Improved combined T2*-weighted MR Imaging of the Brain and Cervical Spinal Cord

Dissertation
Zur Erlangung des Doktorgrades
an der Fakultät für Mathematik, Informatik und Naturwissenschaft
Fachbereich Physik
der Universität Hamburg

vorgelegt von

Ying Chu

Hamburg
2023

Gutachter/innen der Dissertation:	Dr. Jürgen Finsterbusch Prof. Dr. Caren Hagner
Zusammensetzung der Prüfungskommission:	Dr. Jürgen Finsterbusch Prof. Dr. Caren Hagner Prof. Dr. Florian Grüner Prof. Dr. Benedikt Poser Priv.-Doz. Dr. habil. Thomas Lindner
Vorsitzende/r der Prüfungskommission:	Prof. Dr. Florian Grüner
Datum der Disputation:	19.12.2023
Vorsitzender des Fach-Promotionsausschusses PHYSIK:	Prof. Dr. Markus Drescher
Leiter des Fachbereichs PHYSIK:	Prof. Dr. Wolfgang J. Parak
Dekan der Fakultät MIN:	Prof. Dr.-Ing. Norbert Ritter

Eidesstattliche Versicherung / Declaration on oath

Hiermit versichere ich an Eides statt, die vorliegende Dissertationsschrift selbst verfasst und keine anderen als die angegebenen Hilfsmittel und Quellen benutzt zu haben.

Hamburg, den 16.07.2023

Xing Chu

Unterschrift der Doktorandin / des Doktoranden

Abstract

Functional magnetic resonance imaging (fMRI) based on the blood oxygen level-dependent contrast is used to study the function of the central nervous system non-invasively in vivo and has become an important tool in neuroscience and biomedical research. It has been well-established in the human brain for decades and has more recently been increasingly investigated in the human spinal cord. Combined brain and spinal cord fMRI, which can be used to investigate the interaction between these two regions of the central nervous system, is still challenging due to the different geometries, timings, and shim settings that typically would be used for the individual regions. The shimming procedure was cumbersome, time-consuming, and user-dependent; the result was not optimal and sometimes failed. Additionally, the volume coverage was limited. Therefore, the combined brain and spinal cord fMRI was not feasible for more clinical applications.

In this thesis, these issues are addressed. Not only the performance of combined brain and spinal cord T2* weighted MR Imaging has been improved, as is demonstrated in phantom and in vivo experiments, but also its applicability in research and clinical studies has been facilitated considerably. It is shown that a dedicated region-wise shim algorithm increases field homogeneity, which reduces the image artifacts of echo planar imaging, like geometric distortions and signal losses. The procedure to determine the optimum z-shim values has been automatized, which is less time-consuming and not user-dependent, without affecting the image quality. The implementation of the simultaneous multi-slice acquisition method for the brain volume improves the volume coverage and/or temporal resolution for the brain and spinal cord combined T2* weighted image. The image reconstruction has been extended to support on-the-fly image calculation with full functionality without the need for retrospective reconstruction as in previous applications. First steps towards a navigator-based motion detection of the spine have been performed by a navigator echo implemented in the echo planar image sequence, which shows that with the anatomic character of the vertebrae and intervertebral disc, the displacement of the spine along the slice direction can be detected. With these improvements, the performance and applicability of brain and spinal cord combined acquisitions have been improved considerably, not only facilitating its usage in basic research but also paving its way into clinical applications.

Zusammenfassung

Die auf der Blutoxygenierung basierende funktionelle Magnetresonanztomographie wird genutzt um die Funktion des zentralen Nervensystems zu untersuchen. Es ist bereits gut etabliert in Studien des menschenlichen Gehirns, und ist auch zunehmend im menschlichen Rückenmark untersucht worden. Die kombinierte funktionelle Magnetresonanztomographie für Gehirn und Rückenmark, die für die Untersuchung der Interaktion zwischen diesen beiden Regionen des zentralen Nervensystems eingesetzt wird, ist auf Grund von unterschiedlichen Geometrien, Zeitpunkten und Shim-Einstellungen, die normalerweise für die einzelnen Regionen benutzt werden, herausfordernd. Die Einstellung der Shim-Parameter war umständlich, zeitaufwändig und benutzerabhängig, und lieferte keine zufriedenstellende Ergebnisse und scheiterte sogar manchmal. Außerdem konnte nur eine begrenzte Volumenabdeckung erreicht werden. Daher war die kombinierte Gehirn und Rückenmark funtionelle Magnetresonanztomographie nicht in mehr klinischen Anwendungsgebieten einsetzbar.
Diese Arbeit adressiert die oben genannten Probleme. Es wurde nicht nur die Leistung der kombinierten Gehirn- und Rückenmark-T2* gewichteten MR Bildgebung verbessert und im Phantom und in vivo nachgewiesen sondern auch die Benutzerfreundlichkeit in der Forschung und in klinischen Studien wurde erhöht. Durch einen dezidierten regionalen Shim Algorithmus wurde die Feldhomogenität gesteigert, wodurch Artifakte der Echoplanarbildgebung, wie zum Beispiel geometrische Verzerrungen und Signalverluste, reduziert werden konnten. Die Berechnung des optimalen Z-Shims konnte, ohne Verluste in der Bildqualität, automatisiert werde. Diese Berechnung ist dadurch zeitsparender als zuvor und auch benutzerunabhängig. Mit der “Simultaneous Multi-Slice” Methode, die auf das Gehirnvolumen angewendet wurde, konnten sowohl die Volumenabdeckung als auch die zeitliche Auflösung für die kombinierte Gehirn- und Rückenmark-T2* gewichtete Bildgebung verbessert werden. Die Bildrekonstruktion wurde geändert, um parallel zur Messung die Bilder zu berechnen und die nachträgliche Rekonstruktion abzulösen. Es wurde begonnen, eine Bewegungsdetektion, die ein Navigatorecho der Echoplanarbildsequenz nutzt, für die Wirbelsäule zu entwickeln. Damit konnte die Veränderung der Position der Wirbelsäule mittels der periodischen Anordnung der Wirbel und Bandscheiben gezeigt werden. Durch diese Verbesserungen wird das Potenzial der kombinierten Gehirn- und Rückenmark-T2* gewichteten MR Bildgebung gesteigert und die Anwendbarkeit erweitert.

Contents

1 Introduction

Magnetic resonance imaging (MRI) is an important non-invasive medical imaging method used in diagnostics and research, especially for the human central nervous system. It uses a strong magnetic field and radio frequency pulses. It has the possibility to influence the image contrast in a controlled way by choosing the parameters and method of measurement. Thus, it can change or emphasize the image contrast or determine physiological and physical parameters non-invasively. For neuroscience, it is of particular importance, as blood oxygen level-dependent (BOLD) based functional magnetic resonance imaging (fMRI) [33], usually measured with T2* weighting, can study the activity of the central nervous system. It has been well investigated for the human brain, especially with echo planar imaging (EPI), and, recently, is increasingly used in the spinal cord [14]. However, it is more difficult to use due to the required resolution and field homogeneity; therefore, special methods need to be used, e.g., z-shim [18].

Combined brain and spinal cord T2* weighted magnetic resonance imaging [19] plays a critical role in the research of combined brain and spinal cord BOLD fMRI because it records both brain and spinal cord. This allows assessing the functional connectivity between the brain and spinal cord, for example, in pain processing [40] and for the sensory and motor function [4]. However, to date, such acquisitions have many limitations.

One major issue of the combined fMRI is that the standard shim routine is unsuitable because only one shim volume can be used. As a workaround in a previous work[19][40], two separate volumes were used, which allows a dynamic region-wise shim. However, to calculate the shim value, three shim volumes were needed. Therefore, the process was time-consuming, cumbersome, and error-prone. Additionally, this is not the dedicated solution for it because the shim settings are obtained for different volumes. Due to this, the shim result and, thus, the image quality were not always adequate.

Another problem of the combined fMRI is the signal loss for spinal cord fMRI in general. Therefore, another workaround, slice-specific z-shim values [18], was also needed. However, the z-shim values needed to be determined manually for each slice, which was time-consuming and user-depended.

Furthermore, the volume coverage and temporal resolution are limited because one cannot use standard simultaneous multi-slice imaging [37] across two different volumes.

Another critical drawback is that the reconstruction pipeline can only handle one set of parameters for geometry and timing. Therefore, for one volume, the parameters are wrong. In a previous work [19][40], a workaround was used, for which, after the measurement, a

manipulation of the reconstruction parameters and a second, retrospective, reconstruction was done for the second volume. However, the manipulation was difficult, error-prone and time-consuming.
Finally, the motion in the brain can be detected and corrected well due to its clear structure. However, for the spinal cord, only motion in the transversal direction is easy to detect. The motion along the slice direction was hard to detect due to the large slice thickness and the few structural differences along the spinal cord. A workaround was to use the spine position and movement as a proxy; however, due to the large slice thickness the accuracy may be limited.
This thesis addresses these limitations. After introducing the basic principles of MRI and combined brain and spinal cord acquisition in chapter 2, a dedicated shim algorithm [12] for the combined fMRI is presented in chapter 3. The fourth chapter covers the signal loss problem in the spinal cord[10]; for this, an automated z-shim method for the spinal cord region is programmed. The fifth chapter introduces simultaneous multi-slice acquisitions of the brain volume [9]. The sixth chapter presents the newly implemented on-the-fly reconstruction[8] for the combined fMRI to avoid retrospective reconstruction. The seventh chapter covers the first steps towards a navigator acquisition [11] for the motion detection of spinal cord fMRI. The results of the different approaches considered are presented in chapters 3 to 7, each starting with an introduction to the problem and then describing the method and analysis used. They then present and summarize the research findings from the current chapter and discuss the results. The final chapter concludes the research and connects the results with the goal of the thesis.

2 Theory

This chapter first introduces the basics of magnetic resonance imaging (MRI) and the concept of functional magnetic resonance imaging (fMRI). The textbook of Liang and Lauterbur [30] and the textbook Functional Neuroradiology [16] were essential resources for this chapter. Then, the standard EPI optimization methods and combined T2* weighted MR imaging of the human brain and spinal cord are introduced.

2.1 Magnetic Resonance Imaging (MRI)

MRI is a non-invasive biomedical imaging technique that reconstructs cross-sectional images of an object. It is based on the nuclear magnetic resonance (NMR) experiment and requires a strong magnetic field and radiofrequency waves. To obtain information about the spatial position of the different signal contributions, gradient fields are used.
The most used signal resource is hydrogen (^{1}H) in water molecules that are contained in the human body.
Depending on the parameters and methods used, different contrasts in MR images can be generated. Moreover, different acquisition techniques and parameters can suppress or enhance MR signals.

2.1.1 MRI System (Hardware)

A superconducting magnet, a magnetic gradient field system, and a radio frequency (RF) coil system are the three main hardware components of the MR scanner.
The superconducting magnet is the main magnet of the MR system, which generates a high magnetic field strength/ magnetic flux density (B_0). In this thesis, a 3 Tesla superconducting electromagnet was used. The superconductor is Niobium-titanium alloys and is cooled with liquid helium to a temperature of about 4K.
With the help of a passive shim, which uses small metal shims (ferromagnetic plates) in the inner wall of the scanner, the homogeneity of the magnet is improved.
The gradient magnetic system consists of three gradient field (x-, y-, z-axis fields) sets orthogonal to each other. The gradient magnetic fields are linear in space, and the three fields can be used independently so that the linear gradient field can be created in any spatial direction. The center of this gradient field defines the isocenter.

The RF coil system is used to transmit and receive radio frequencies. The transmit part generates an oscillating magnetic field (B_1) inside the object. B_1 can then excite the spins in an object to generate signals. B_1 is usually only used for several milliseconds, so we call it an RF pulse as well. The receiving part detects the signal as voltage due to Faraday's law of induction, as the excited spins build an oscillating net magnetic flux. It is important to note that there is normally more than one coil element for the MR system. The most-often-used coil in this thesis is a head-neck coil with 64 separate coil elements.

2.1.2 Magnetization and NMR

Nuclear magnetic resonance (NMR) refers to a phenomenon where nuclei are in a strong magnetic field and are perturbed by an oscillating magnetic field with a frequency near the intrinsic frequency of the nuclei. The nuclei will precess along the direction of the strong magnetic field with their alignment depending on their spin. The oscillating magnetic field disturbs the direction of this precession. In this section, we will explain the magnetization and electromagnetic signal from the nuclei.

One important characteristic of nuclei in NMR is that the nuclei have a spin angular momentum $\vec{j}$.The magnetic field from the spinning nuclei is called the nuclear magnetic dipole moment (magnetic moment). This magnetic moment can be written as

$$\vec{\mu} = \gamma \vec{j} \tag{2-1}$$

where γ is the so-called gyromagnetic ratio, which depends on the nucleus. For example, $\frac{\gamma}{2\pi}$ for ^{1}H is $42.58 MHz/T$ while for ^{23}Na it is $11.26 MHz/T$. The nuclei of ^{1}H are the most used resource for signal creation in MR imaging because hydrogen can be found in the biological tissue with a suitable gyromagnetic ratio, which results in a sufficient signal.

In the framework of quantum mechanics, we know the magnitude of the magnetic moment is

$$\mid \vec{\mu} \mid = \gamma \hbar \sqrt{I(I+1)} \tag{2-2}$$

where $\hbar$ is the reduced Planck constant $1.05 \times 10^{-34} Js$, I is the nuclear spin quantum number. For ^{1}H, $I = \frac{1}{2}$, thus, it is a spin-$\frac{1}{2}$ system. As $\hbar$ is a constant, and both γ and I are the intrinsic characters of nuclei, the magnitude of the magnetic moment $\vec{\mu}$ of a nucleus is also intrinsic and will not change with or without an external magnetic field. However, $\vec{\mu}$ could change because the direction of $\vec{\mu}$ is random in field-free space due to Brownian motion. The magnetic moment $\vec{\mu}$ will be lined up under an external magnetic field. Therefore, under a macroscopic observation, a human body has no net magnetic field in a field-free space, although it contains many spins. We assume that $\vec{B_0}$ is placed in the laboratory z-direction. Therefore, the magnetic moment can be written by

$$\mu_z = \gamma m_I \hbar \tag{2-3}$$

where m_I is the magnetic quantum number, which can take $(2I + 1)$, states, which are $-I, -I + 1, ..., I - 1, I$. We have a spin-$\frac{1}{2}$ system, thus, we have $m_I = -\frac{1}{2}$ and $m_I = \frac{1}{2}$. If we have a strong external magnetic field with a strength of $\vec{B_0}$, the energy of spins is

$$E = -\vec{\mu} \cdot \vec{B_0} = -\gamma m_I \hbar B_0 \tag{2-4}$$

Then we can calculate the difference in energy between spin-up and spin-down states.

$$\Delta E = E_\downarrow - E_\uparrow = \gamma \hbar B_0 \tag{2-5}$$

Due to the Boltzmann relationship, there is a difference in the number of nuclei between spins in spin-up and spin-down states. The ratio between the number of spins in these two states is given by

$$\frac{N_\uparrow}{N_\downarrow} = exp(\frac{\Delta E}{K_B T_s}) \tag{2-6}$$

where $N_\uparrow$ is the population of spins in the spin-up state and $N_\downarrow$ is the population of spins in the spin-down state, K_B is the Bolzmann constant which is $1.38 \times 10^{-23} J/K$ and T_s is the temperature of the spins. The average absolute temperature of the human body is 310 K, so $\Delta E \ll K T_s$. Therefore, we could approximate that the ratio between $N_\uparrow$ and $N_\downarrow$ is about $1 + \frac{\gamma \hbar B_0}{K_B T_s}$. Because of $N_\uparrow \approx N_\downarrow$, both amounts of spins in spin-up and spin-down state could be approximated to $\frac{N}{2}$. So from equation 2-6, we have the difference of spins between two states:

$$N_\uparrow - N_\downarrow \approx N \frac{\gamma \hbar B_0}{2 K_B T_s} \tag{2-7}$$

The equation above shows that the difference in the population of spins in spin-up and spin-down states is small.

We know that the sum of magnetic moments $(\vec{\mu})$ of all spins constitute the macroscopic magnetization vector $\vec{M}$ which is

$$\vec{M} = \sum_{n=1}^{N} \vec{\mu}_n = \sum_{n=1}^{N_\uparrow} \vec{\mu}_{n\uparrow} + \sum_{n=1}^{N_\downarrow} \vec{\mu}_{n\downarrow} \tag{2-8}$$

where $\vec{\mu_n}$ is the magnetic moment of the nth spin, and N is the population of spins in the spin system. So if we substitute equation 2-3 $\vec{\mu} = \gamma m_I \hbar$ into equation 2-8 we get

$$M_z = (\sum_{n=1}^{N_\uparrow} \frac{1}{2} \gamma \hbar + (-\sum_{n=1}^{N_\downarrow} \frac{1}{2} \gamma \hbar)) = \frac{1}{2}(N_\uparrow - N_\downarrow) \gamma \hbar \tag{2-9}$$

Therefore, if we substitute equation 2-7 $N_\uparrow - N_\downarrow \approx N \frac{\gamma \hbar B_0}{2 K T_s}$ into the equation above, we have the magnitude of the bulk magnetization in the magnetic field direction of the main magnet of an MRI system which we consider the z-direction:

$$M_z^0 = \frac{\gamma^2 \hbar^2 B_0 N}{4 K_B T_s} \tag{2-10}$$

M_z^0 is the magnetization value for $\vec{M}$ in the presence of $\vec{B}_0$ only, which is the thermal equilibrium. This formula shows that the bulk magnetization of the spins is proportional to the gyromagnetic ratio of the nucleus (γ), the magnetic strength of the main magnet (B_0), and the population of spins (N). The bulk magnetization is inversely proportional to the spin system's temperature (T_s).
Higher magnetization means a higher signal. γ and N depend on the nucleus we chose to excite. As we know, hydrogen has a relatively high γ with $42.58MHz/T$. The human body contains a lot of ^{1}H, which means a large N. Therefore, the hydrogen MR image is the most popular MR imaging.
An increased magnetic field B_0 also increases the spin system's bulk magnetization. Common clinical or research systems' magnetic field strength is $1.5T$ or $3T$. $7T$ MRI system is getting more common in research areas. However, only one percent of the MR research institute's scanners have a $7T$ or higher main magnet. There are small animal MR systems even with a field strength of $16.4T$. The spin systems to be measured are usually human beings or other living animals, so the temperature of the spin system T_s is fixed.

2.1.3 Signal Source of MRI

Signal Generation

The net magnetization of the spin system is parallel to the main external magnetic field. To obtain a signal, we use an RF magnetic field $\vec{B}_1(t)$, which is perpendicular to B_0. We define the magnetic field direction from the main magnet as the longitudinal direction (z-axis). The oscillating magnetic field, the so-called radio frequency pulse (RF pulse), should be in the transverse (xy) plane.
The frequency ω_{rf} of the oscillating magnetic field $\vec{B}_1(t)$ resonates with the Larmor precession frequency of the spins in the external magnetic field, which is given by the Larmor frequency ω_0,

$$\omega_0 = \gamma B_0 \tag{2-11}$$

Therefore, the resonance condition of the oscillating magnetic field and the spin under a strong magnetic field can be written as

$$\omega_{rf} = \omega_0 = \gamma B_0 \tag{2-12}$$

Signal Detection

The spin system creates a time-dependent magnetization that can be transferred to electrical signals. As we know from the Faraday law of electromagnetic induction and the principle of reciprocity, the time-varying magnetic flux through a conducting coil will induce a voltage in the coil. In MRI, we use a conducting coil as a receiver coil to detect the signal. The

magnetic flux through the coil by $\vec{M}(r,t)$ is defined by

$$\Phi(t) = \int \vec{B}_r(r) \cdot \vec{M}(r,t) dr \tag{2-13}$$

where $\vec{B}_r(r)$ is the magnetic field at location r produced by a unit current through the coil, $\vec{M}(r,t)$ is the magnetization. If we use Faraday's law of induction, we have the voltage to detect in the coil due to the time-changing magnetization is

$$V(t) = -\frac{\Phi(t)}{dt} = -\frac{d}{dt} \int \vec{B}_r(r) \cdot \vec{M}(r,t) dr \tag{2-14}$$

The voltage is the raw signal of the MR imaging.

Relaxation

After the RF pulse perturbed the spins with their resonance frequency, the spin system will return to the thermal equilibrium state where $\mid \vec{M} \mid = M_z^0$. This process is called relaxation. Given that the Bloch equations describe the time-dependent magnetization in the presence of an external magnetic field, these equations can be used to describe the Larmor precession. The general form of the Bloch equation is

$$\frac{d\vec{M}}{dt} = \gamma \vec{M} \times \vec{B} - \frac{M_x \vec{i} + M_y \vec{j}}{T_2} - \frac{(M_z - M_z^0)\vec{k}}{T_1} \tag{2-15}$$

where $\vec{B}$ is the magnetic field consisting of the constant main magnetic field $\vec{B}_0$ and the oscillating magnetic field $\vec{B}_1(t)$.
We can consider the longitudinal magnetization M_z and the transverse magnetization M_{xy} separately. The recovery of M_z is called longitudinal relaxation or T_1 relaxation, and the decay of the transverse magnetization M_{xy} is called transverse relaxation or T_2 relaxation. To better understand the effects of rotating magnetic fields, we should use a rotating frame. If we observe the spin system in a rotating frame, the transverse plane is rotating clockwise at an angular frequency ω. We use x', y', and z' to describe the three orthogonal axes of the rotating frame, and $\vec{i}'$, $\vec{j}'$ and $\vec{k}'$ as their unit vectors. We use the Larmor frequency ω_0 as the angular frequency. Then we have the so-called Larmor-rotating frame. The Bloch equation in the Larmor-rotating frame is then given by

$$\frac{d\vec{M}_{rot}}{dt} = \gamma \vec{M}_{rot} \times \vec{B}_{eff} - \frac{M_{x'} \vec{i}' + M_{y'} \vec{j}'}{T_2} - \frac{(M_z - M_z^0)\vec{k}'}{T_1} \tag{2-16}$$

Here, $\vec{B}_{eff}$ is the effective magnetic field for the bulk magnetization vector $\vec{M}$ in a rotating frame which contains the magnetic field from the main magnet, the oscillating magnetic field, and the magnetization. Therefore, we have

$$\vec{B}_{eff} = \vec{B}_0 + \frac{\vec{\omega_0}}{\gamma} \tag{2-17}$$

The term $\frac{\vec{\omega_0}}{\gamma}$ is the magnetic field component from the simplified behavior of $\vec{M}_{rot}$. We can assume that $\vec{B} = B_0\vec{k}$ and $\vec{\omega} = -\gamma B_0\vec{k}$ because the spin system is in resonance with the main magnetic field. Then we will have the effective magnetic field $\vec{B}_{eff} = 0$. Therefore, the Bloch equation has only the last two terms

$$\frac{d\vec{M}_{rot}}{dt} = -\frac{M_{x'}\vec{i'} + M_{y'}\vec{j'}}{T_2} - \frac{(M_{z'} - M_z^0)\vec{k'}}{T_1} \tag{2-18}$$

or

$$\begin{aligned} \frac{dM_{z'}}{dt} &= -\frac{M_{z'} - M_z^0}{T_1} \\ \frac{dM_{x'y'}}{dt} &= -\frac{M_{x'y'}}{T_2} \end{aligned} \tag{2-19}$$

If we solve the equation, we obtain

$$\begin{aligned} M_{z'}(t) &= M_z^0(1 - e^{-\frac{t}{T_1}}) + M_{z'}(0)e^{-\frac{t}{T_1}} \\ M_{x'y'}(t) &= M_{x'y'}(0)e^{-\frac{t}{T_2}} \end{aligned} \tag{2-20}$$

Where $M_{z'}(0)$ and $M_{x'y'}(0)$ are the magnetization during t = 0. From the equation above, we know that the decay of the transverse magnetization and the recovery of the longitudinal magnetization are exponential functions. It should be noted that this exponential description applies only to spin systems with weak spin-spin interactions, e.g., which also covers ^{1}H in tissue water.

We now analyze the situation that the RF pulse is a 90° pulse, which means the transversal magnetization takes the whole magnetization in thermal equilibrium M_z^0, therefore, $M_{x'y'}(0) = M_z^0$ and $M_{z'}(0) = 0$. We substitute these two equations into equation 2-20 and easily get the time evolution of the magnetization in the longitudinal and the transversal direction

$$\begin{aligned} M_{z'}(t) &= M_z^0(1 - e^{-\frac{t}{T_1}}) \\ M_{x'y'}(t) &= M_z^0 e^{-\frac{t}{T_2}} \end{aligned} \tag{2-21}$$

A graphical description for T_1 and T_2 process is shown in figure **2-1** and figure **2-2**

Another important property that can be derived from the rotating frame excitation principles is the flip angle. If the magnetic field B_1 is in resonance with the larmor frequency ω_0, the magnetization in the rotating frame rotates only around B_1. The strength of B_1 defines the speed of the rotation. Therefore, the angle accumulated by $B_1(t)$ with time-varying amplitude can be calculated as

$$\alpha = \int_0^\infty \gamma B_1(t)dt \tag{2-22}$$

which is called a flip angle. If there is a constant magnetic field B_1 applied over time duration τ, the flip angle is then $\alpha = \gamma B_1\tau$.

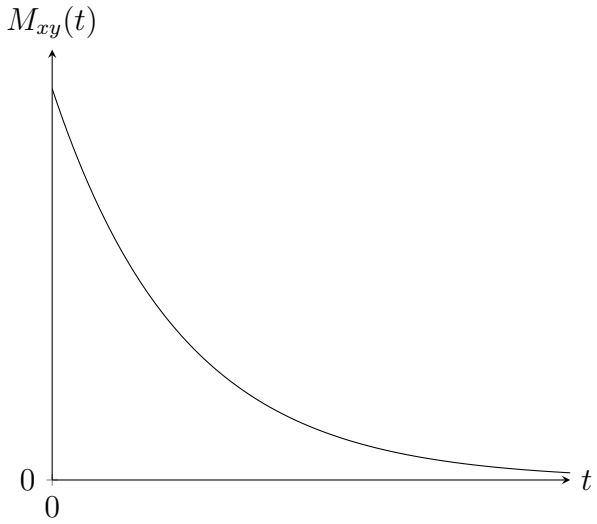

Figure **2-1**: T_2 relaxation curve

$$M_z(t) = M_z^0(1 - e^{-t/T_1}) + M_z(0)e^{-t/T_1}$$

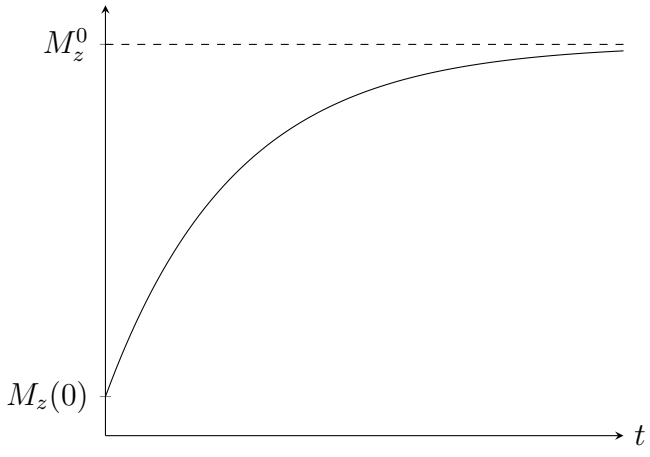

Figure **2-2**: T_1 relaxation curve

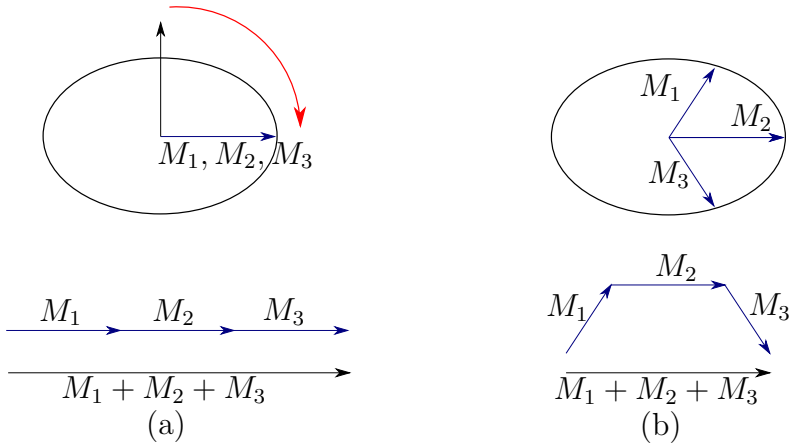

Figure **2-3**: (a) Immediately after the RF pulse, all magnetizations ($\vec{M}_1$, $\vec{M}_2$,and $\vec{M}_3$) have the same phase. Hence, the net magnetization ($\vec{M}_1 + \vec{M}_2 + \vec{M}_3$) has a high magnitude. (b) Different isochromats have different precession frequencies. Therefore, they have different phases after a duration, and the net magnetization ($\vec{M}_1 + \vec{M}_2 + \vec{M}_3$) has a lower magnitude than before. This is called dephasing. (Image from Chu, 2019[6])

2.1.4 MR Signals

This section will observe basic MR signals relevant to this thesis: free induction decay, gradient echo, and spin echo.

Free Induction Decays (FID)

"Free" means that the signal is generated by free precession of the bulk magnetization, and "induction" refers to the fact that the signal is being produced based on Faraday's law of electromagnetic induction. "Decay" is because the signal amplitude decreases over time. This is the signal that we can measure directly after the RF pulse.

In the thermal equilibrium, the longitudinal relaxation points in the direction of the main magnetic field direction which is hard to detect because the magnetic field from the main magnet is much higher than the magnetization of the object.

The FID is theoretically the T_2 decay if the magnetic flux density is a perfect homogenous magnetic field. However, there is never a T_2 decay process after the RF pulse because of the field inhomogeneity. Therefore, the isochromats do not all precess in phase due to the relationship $\omega = \gamma B$; thus, the summation of different isochromats could vanish or partly vanished. A graph illustration is shown in figure **2-3**.

In conclusion, different isochromats have different phase, which results in a loss of the net magnetization, and causes a decay in the detected signal. The time constant descirbing this

deacy is termed T2* and is given by

$$\frac{1}{T_{2*}} = \frac{1}{T_2} + \gamma \Delta B_0 \tag{2-23}$$

From the equation above, we can assume that the T_2* process is not an exponential decay. If the field inhomogeneity is higher (ΔB_0 is larger), T_2^* is smaller, which means the time for the signal detection is less.

Echo Signals

The so-called echo: Another form of MR signal is often used. The main difference between an FID signal and an echo signal is that the echo signal has two sides. One side of the signal is the rephasing of the transverse magnetization, and another is the dephasing of the transverse magnetization. We can use a time-varying gradient magnetic field or more than one RF pulse to create an echo signal. The one created by a gradient magnetic field is called gradient echo. The one created by multiple RF pulses can be spin echo or stimulated echo. The gradient echo is the major signal used for this thesis, so we will discuss the gradient echo in detail and will only have an overview for spin echo.

Gradient Echo

Due to the relationship $\omega = \gamma B$, an additional gradient magnetic field can dephase and rephase isochromats, creating controlled echoes. A gradient field is the magnetic field strength changes linearly along a direction. We know that the MRI scanner has $x-$, $y-$, and $z-$gradient coils. So we have

$$\begin{aligned} B_{G,z} &= G_z z \\ B_{G,y} &= G_y y \\ B_{G,x} &= G_x x \end{aligned} \tag{2-24}$$

The $x-$,$y-$, and $z-$ are linearly and independently. To simplify the three equations, we write the equation as

$$B_G = G_x x + G_y y + G_z z \tag{2-25}$$

The main magnetic field and the gradient field are

$$\vec{B} = (B_0 + G_x x + G_y y + G_z z)\vec{e}z \tag{2-26}$$

If we group the three gradients to a gradient vector $\vec{G}$, we have

$$\vec{G} = G_x \vec{e}_x + G_y \vec{e}_y + G_z \vec{e}_z \tag{2-27}$$

Then, the direction vector can be summarized with $\vec{r}$, therefore, we can write the equation 2-25 as

$$\vec{B}_G = \vec{G} \cdot \vec{r} \tag{2-28}$$

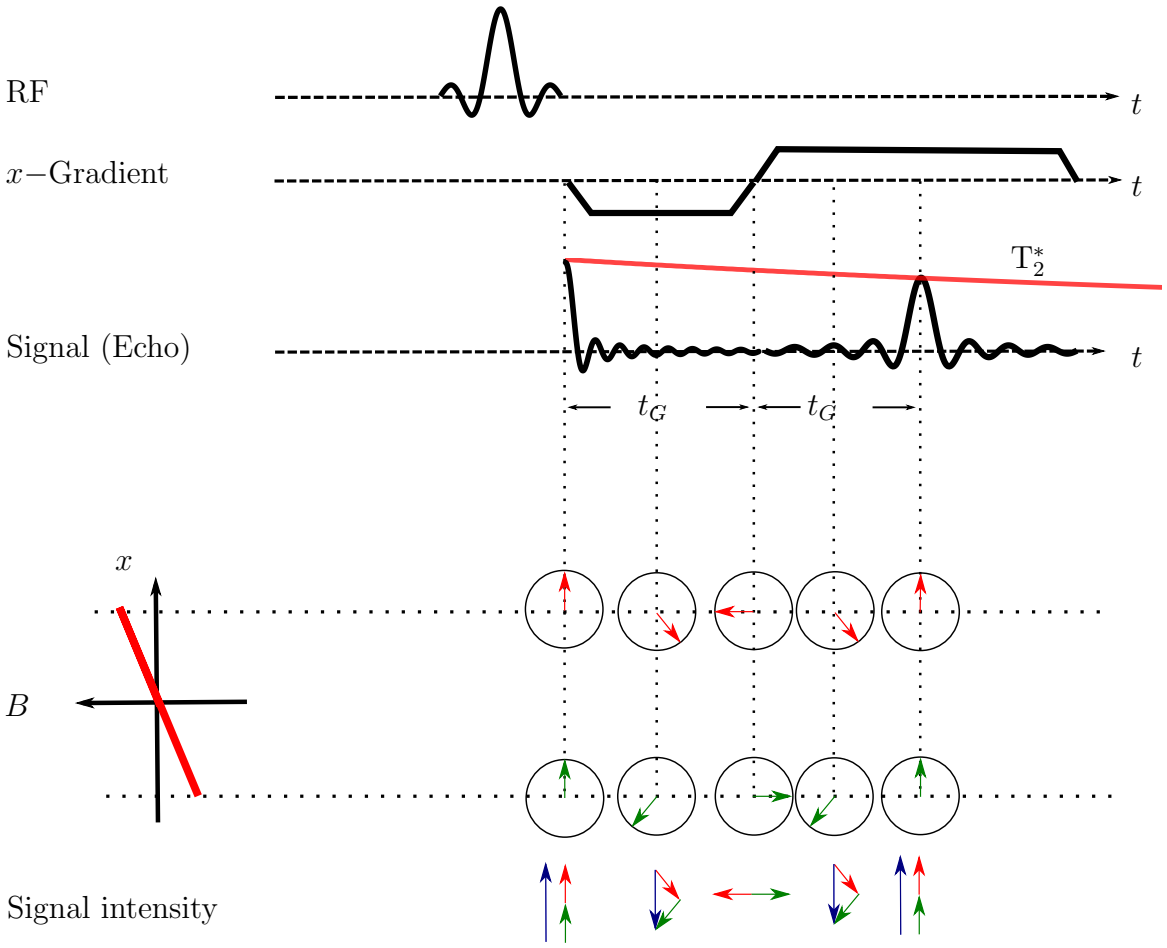

Figure **2-4**: The upper part of this figure is an MR sequence diagram of a gradient echo. The first line noted with "RF" shows the sinc-shaped RF pulse. The second line noted with "$x-$Gradient" shows the status of the $x-$gradient. The third line noted with "Signal (Echo)" shows the FID signal and the echo. The lower part of this figure shows two isochromats (red arrow and green arrow) created by the $x-$gradient and their net magnetization (blue arrow). In this diagram, some vertical dotted lines are shown to mark the time position between the sequence diagram and the isochromat diagram.

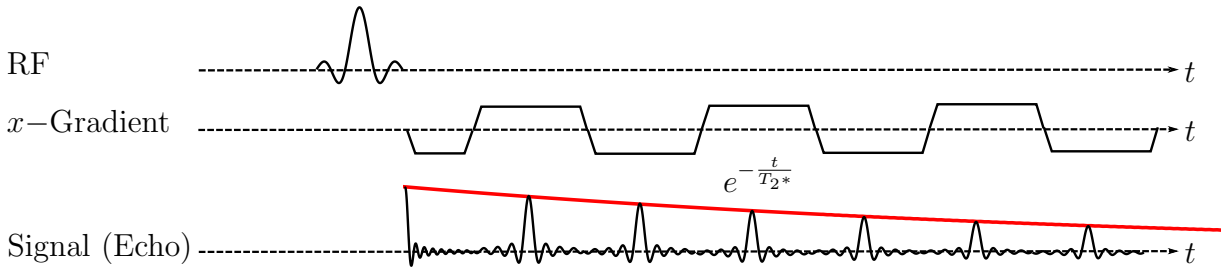

Figure **2-5**: A sequence diagram with multiple gradients echoes after one RF pulse. The red line follows the T_2* decay.

where $\vec{G}$ is a function of time and $\vec{r}$ is the vector of the position. Figure **2-4** is a so-called sequence diagram that presents the dephasing and rephasing of the signal with gradient echo. Immediately after applying an RF pulse, we add a negative gradient (e.g., $x-$ gradient). Therefore, the spins in different positions along the $x-$ gradient axis will experience different frequencies which means different phases after a time t. The phase acquired by different isochromats can be described as

$$\phi(x,t) = \gamma \int_0^t -G_x x dt' \tag{2-29}$$

Figure **2-4** shows a simplified illustration (only two isochromats are shown) of the development of gradient echo. The net magnetization (blue arrow in figure **2-4**) of the second time position is smaller than the one in the first position. After a while (a time period of t_G, without the consideration of the ramp up and ramp down time of the gradient.), the signal will be reduced to zero because the signal of the two isochromats (red and green) cancel each other. If we now add a positive gradient, the isochromats will be rephased after a time period t_G if the gradient areas are the same between the negative and the positive gradient. We can see that the echo in the sequence diagram is still reduced because of the T_2 relaxation and the dephasing from the field inhomogeneity. However, this spin diagram is for understanding the dephasing and rephasing processes due to the gradient. Many isochromats have this process to build the final net magnetization.
Figure **2-5** shows that after one echo, the magnetization of isochormats can be dephased and rephased again multiple times. The signal will follow the T_2* decay and always be smaller than the original magnetization amplitude.

Spin Echo

Spin echo is an RF-refocused echo because we can make an echo signal with two or more RF pulses. Figure **2-6** shows a spin echo created by two RF pulses. After the second RF pulse, the isochromats which have a slower frequency now lead, so they will be back in the initial position at the same time that the faster frequency isochromats spins go back to the initial

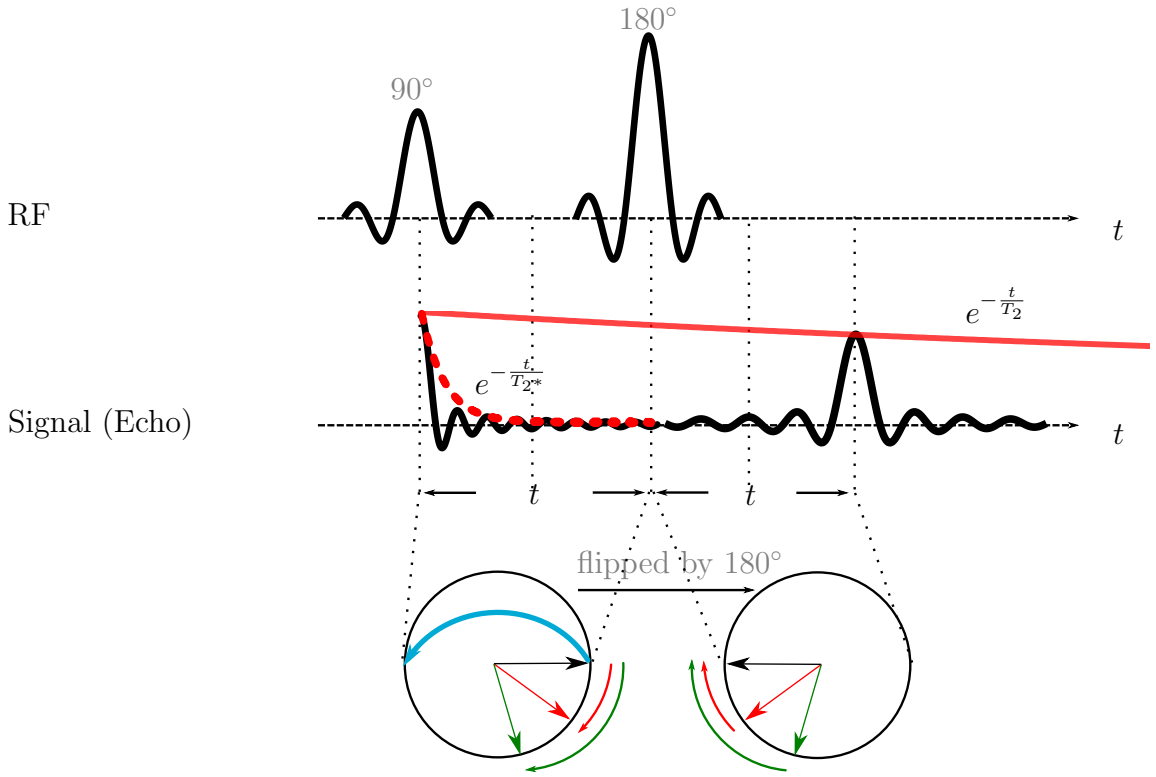

Figure **2-6**: A sequence diagram (top) with a spin echo after two RF pulses, and phase diagrams (bottom) describe phases of spin before and after the flip (180° puls). After the first 90° RF pulse, the spins are in phase in the transverse plane and start to precess. Because the isochromats are in different magnetic fields, they precess with slightly different frequencies. Isochromat (green arrow) is the fastest, isochromat (red arrow) is slower, and isochromat (black arrow) is the slowest. After a complete decay of the signal due to T_2^* decay, another, stronger, RF pulse is used to flip the isochromats by 180°. After this RF pulse, the isochromat (black), which is slow and was behind, is leading now. After $2t$, the isochromats are in phase again, which reaches the maximum of the echo.

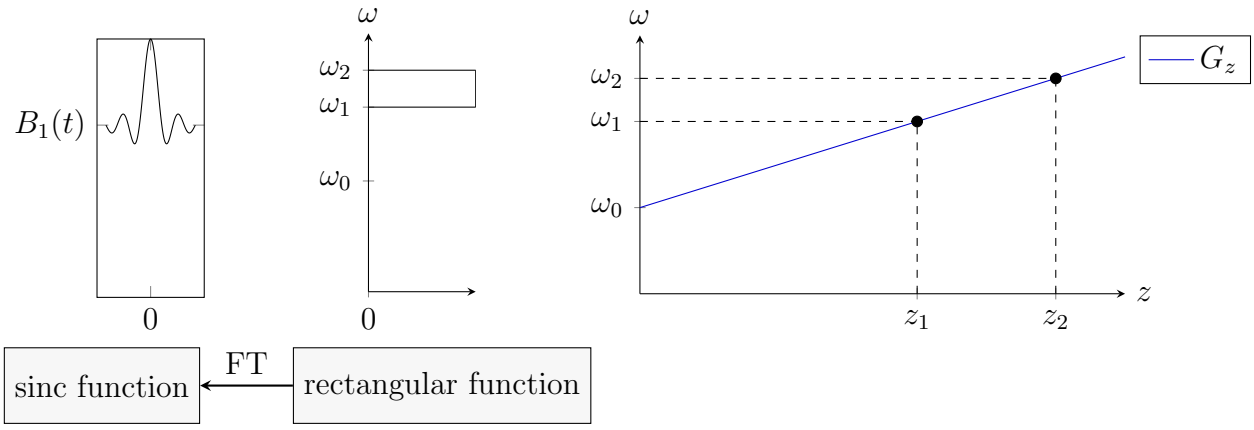

Figure **2-7**: Relationship between slice parameters and the excitation profile.

position. Therefore, the echo signal at refocusing (t = TE) contains no T_2^* decay, and the field inhomogeneity will not influence the signal from spin echo. The example shown in the figure shows one of the often used flip angles 90° and 180° for the creation of the spin echo. In general, we use α_1 and α_2 for the two flip angles. The echo signal amplitude is then given by

$$M = M_z^0 sin\alpha_1 sin^2\frac{\alpha_2}{2} e^{-\frac{2t}{T_2}} \tag{2-30}$$

Now we know from the equation above, if the first RF pulse has a flip angle of 90° and the second RF pulse has a flip angle of 180°, the signal amplitude reaches its maximum value. And the signal amplitude of the echo is always smaller than M_z^0.

2.1.5 Signal Localization

This section shows slice-selective RF excitation and how the spatial information of spins of one slice is encoded with the use of gradients.

Slice-Selective RF Excitation

The signal contains the information from the transverse magnetizations of the whole object. Therefore, the slice-selective RF excitation can be used to select the signals from one slice. The idea for slice-selective RF excitation is that different magnetic fields should be added at different slice positions of an object so that the spins will have different resonance frequencies for different positions. The gradient magnetic field can be used for the application of different magnetic fields at different positions.

For example, for spins in a main magnetic field of B_0 with a precession frequency of ω_0, we can use an RF pulse to excite a slice parallel to the $xy-$plane with a thickness of Δz. The Larmor Frequency can be written as

$$\omega(z) = \omega_0 + \gamma \cdot G_z \cdot z \tag{2-31}$$

Because we have a thickness for the excited slice, we need two different z (z_1 and z_2) as borders that result in two frequencies borders ω_1 and ω_2, we now have

$$\begin{aligned} \omega_1 &= \omega(z_1) = \omega_0 + \gamma G_z z_1 \\ \omega_2 &= \omega(z_2) = \omega_0 + \gamma G_z z_2 \end{aligned} \tag{2-32}$$

This equation above and figure **2-7** shows that the value of ω_1 and ω_2 are linearly dependent on the slop of the gradient G_z and the slice parameters (thickness and position). To design a sinc function for excitation, we must first design the border z_1 and z_2. The intersection points with G_z define the ω_1 and ω_2, so we have a rectangular excitation profile. And we know the Fourier Transform of a rectangular function is a sinc function. Therefore, the excitation RF pulse $B_1(t)$ is a sinc function. It should be noted that the same sinc function parameters can result in different slice parameters by changing the slope of the gradient G_z.With the help of slice-selective excitation, only the spins at the selected slice are excited. Therefore, the echo signal only contains the information from the selected slice.

Spatial Encoding

This section summarizes how spatial information can be encoded into echo signals. There are two usually used ways to encode spatial signal information, called frequency encoding and phase encoding, respectively.
After the excitation, we have a homogenous magnetic field B_0 again. If we introduce another linear gradient field $\vec{G}$, the Larmor frequency is position dependent:

$$\omega(\vec{r}) = \omega_0 + \gamma \vec{G} \cdot \vec{r} \tag{2-33}$$

This is the so-called frequency encoding (readout) because every position along the gradient $\vec{G}$ has a unique frequency $\omega(\vec{r})$ according to the equation above. Therefore, the received signal from the excited spins can be written as

$$S(t) = \int \rho(\vec{r}) e^{-i(\omega_0 + \gamma \vec{G} \cdot \vec{r})t} dr \tag{2-34}$$

After the removal of the carrier signal $e^{-i\omega_0 t}$ (demodulation), we will have a simplified frequency encoded signal formulation, which is

$$S(t) = \int \rho(\vec{r}) e^{-i\gamma \vec{G} \cdot \vec{r} t} dr \tag{2-35}$$

where $\rho(\vec{r})$ is the spin distribution of the target spins and $\vec{r}$ is the position vector of the frequency gradient.

However, this is still not all the information we need for cross-section imaging because it is only encoded in the direction of the gradient.
To make a reconstruction of a two-dimensional image possible, we also need another encoding method in another direction: the so-called phase encoding.
To realize the phase encoding, we introduce a gradient in the selected phase encoding direction for a short duration T_{PE}. Therefore, the phase of the target spins changes for a phase ($\Phi(\vec{r})$), and the Φ is dependent on the position $\vec{r}$

$$\Phi(\vec{r}) = -\gamma \cdot \vec{G} \cdot \vec{r} \cdot T_{PE} \tag{2-36}$$

Therefore, every spin position with the same frequency information due to frequency encoding can be encoded with different initial phase information from their position in the phase encoding direction. Now, with the frequency encoding and the phase encoding, information from the entire excited cross-section is encoded. For example, we can use frequency encoding to the orthogonal direction of phase encoding.
Two important sequence diagrams are shown in figure **2-8**, which is a fast low angle shot (FLASH) sequence, and figure **2-9**a, which is an echo planar imaging (EPI) sequence. Both sequences use gradient echoes. The second sequence, EPI, is the main sequence for functional MRI (fMRI).

k Space

In this section, the k-space notation is introduced. We assume that the frequency encoding direction is on the x-axis of the laboratory system. From equation 2-35, we have

$$S(t) = \int \rho(x) e^{-i\gamma G_x \cdot x t} dx \tag{2-37}$$

If we substitute the trajectory relationship

$$k_x = \gamma G_x t \tag{2-38}$$

into the equation above, we will obtain the following Fourier transform relationship:

$$S(k_x) = \int \rho(x) e^{-i2\pi k_x x} dx \tag{2-39}$$

Equation 2-38 means that the frequency encoding gradient over time gives a straight line in the k space shown in figure **2-10**. Equation 2-39 follows that the Fourier transform of the signal S recovers the spatial information of the magnetization.
This k sampling is from a basic FLASH sequence as shown in figure **2-8**. After every RF excitation, the phase encoding gradient trapezoids with different amplitudes (dashed blue and red in figure **2-10**) are turned on, together with the negative frequency encoding gradient,

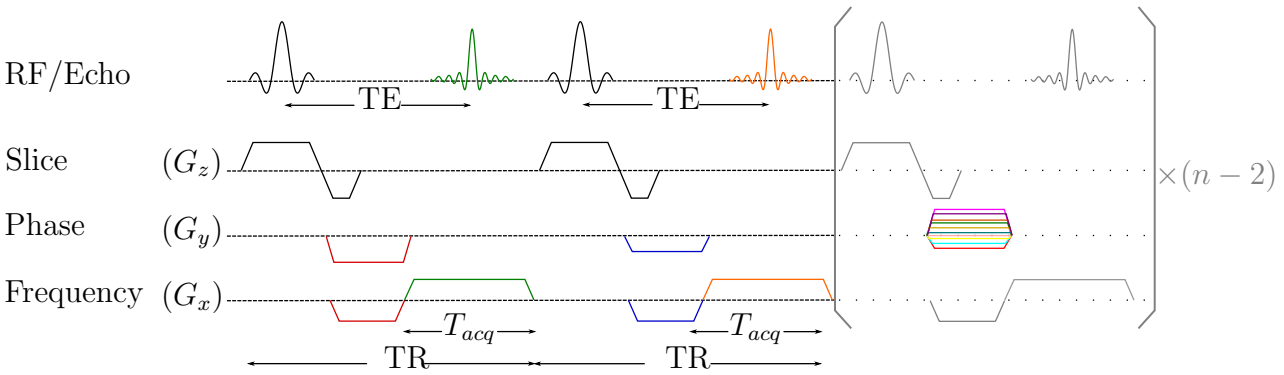

Figure **2-8**: Fast low-angle shot (FLASH) sequence. On the first row are the RF pulses and the echoes. On the second row are the gradients for the slice-selective excitation. On the third and fourth rows are the gradients for phase and frequency encoding. First, we must turn on a gradient for the slice-selective RF excitation. Then, a rephasing gradient is needed to refocus the spins to avoid signal loss due to the phase shift across the slice thickness. This rephasing gradient has half of the amplitude times the duration of the gradient for the slice-selective pulse. During the rephasing gradient in the slice-selective direction is used, the phase encoding gradient (red) for the phase encoding is introduced, shown on the axis "Phase (G_y)". A negative dephasing gradient (red) is also activated in the frequency encoding direction before the spins can be rephased with a positive gradient (green) on the x axis to build an echo. We can see that after the first and second RF pulses, the phase encoding gradients have different amplitudes (red and blue) after the RF pulse. They encode different initial phases for spins in the object with the phase encoding gradients. Therefore, as we can see in the grey part of the sequence, different phase encoding gradients are introduced for the same slice-selective RF excitation. If we assume n is the number of phase encoding steps. The grey part is repeated for $(n-2)$ times. During each repetition time (TR), different amplitudes of phase encoding gradients (shown as different colored trapezoids) are used.

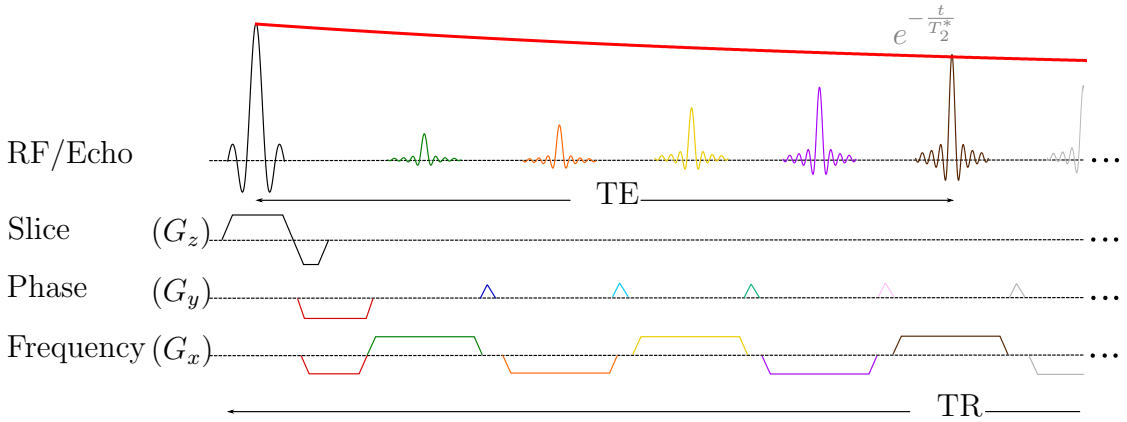

(a) An example sequence diagram of an Echo Planar Imaging (EPI) sequence which depicts the RF pulse and gradients during the data acquisition (readout) of an EPI sequence. First, a slice selective RF excitation (black sinc pulse) is applied. After this RF pulse, a negative phase encoding gradient (red) and a negative frequency encoding gradient (red) pre-dephased the spins and decide the first horizontal line (green in figure b) in the k-space for data acquisition. After the first data acquisition, a phase encoding blip (blue) is turned on, which makes the data acquisition line in the k space travel to the next horizontal line (orange) parallel to the first, green, one. And then another phase encoding blip (light blue) is turned on, which makes the data acquisition line in the k space travel to the next horizontal line (yellow), and the echo is acquired then. The phase encoding and frequency encoding repeat themselves, and the data of the k space could be acquired.

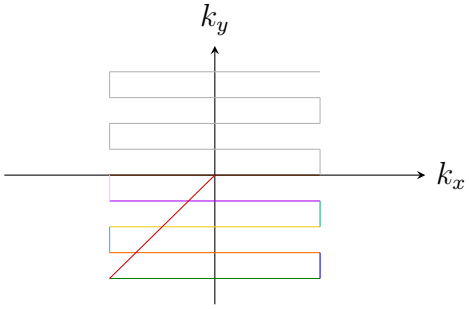

(b) k space data sampling in EPI. The trajectory starts in the center of the k space and follows the red diagonal line to one edge of the k space. Then, the trajectory follows a zig-zag pattern.

Figure **2-9**: An Echo Planar Imaging (a) sequence and (b) its k space data sampling diagram. The graphs of both diagrams with the same color indicate the same steps in the data sampling. The steps of gradient encoding in the (a) sequence diagram have the same number as the horizontal lines in the (b) k space data sampling diagram.

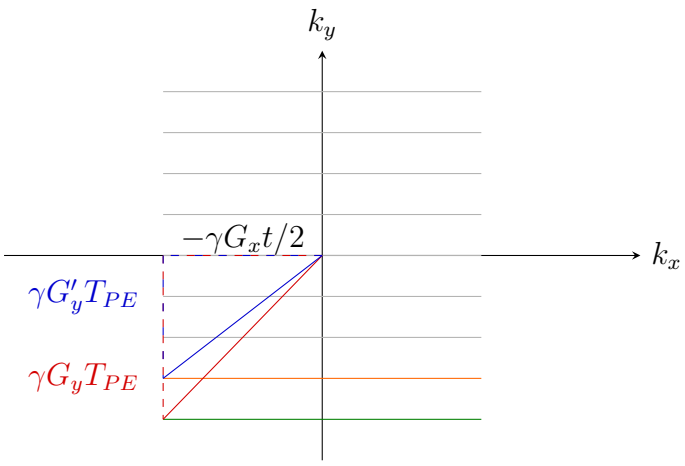

Figure **2-10**: A k-space trajectory example of FLASH. In the step with the red marked trajectory, a negative G_x (red) and G_y (red) shift the trajectory to the first data sampling start for the frequency encoded signal (green). Data are acquired when the next G_x (green) is active. After acquiring the first echo, a different G_y (blue) and the same negative G_x (blue) create another starting point for the data sampling so that the next frequency encoding trajectory (orange) is parallel to the first one. t is the time duration of the gradient for frequency encoding.

resulting in different start points for the frequency encoding trajectory. The trajectory relationship can be written as

$$k_y = \gamma G_y T_{PE} \tag{2-40}$$

where T_{PE} is the time duration of the activated phase encoding gradient.
The k space trajectory for a typical EPI sequence is drawn in figure **2-9**b. The examples shown in this section are only cartesian sampling examples. There are different k space trajectory patterns for data sampling because every sampling point contains the entire spatial information of the image. Some popular sampling trajectories are cartesian, radial, spiral, and random sampling methods. The signals near the center of the k space determine the brightness of the image because they are at a low-frequency area. The signals near the edge of the k space determine the image's detail.

2.2 Principle of Functional MRI

fMRI can visualize the activity of the central nervous system. Most fMRI applications are based on the Blood Oxygen Level Dependent (BOLD) contrast which uses the local field inhomogeneities induced by activities of the central nervous system and requires T2* weighted acquisitions. Echo Planar Imaging (EPI) is a commonly used MRI technique for

fMRI due to its short acquisition time, as detecting the activity is a dynamic process. The following section summarizes the basics of fMRI related to this thesis and is mainly based on the textbook Echo-Planar Imaging Theory, Technique, and Application.[35]

2.2.1 Blood Oxygen Level Dependent (BOLD) Contrast

Gradient echo blood oxygen level-dependent (GE-BOLD) contrast is based on a susceptibility difference that linearly scales with the field strengths [32]. The neuronal activity changes the concentrations of deoxy- and oxyhemoglobin in the blood. Deoxyhemoglobin has four unpaired electrons at its iron atom which makes the deoxyhemoglobin paramagnetic and results in a microscopic local magnetic field inhomogeneity in the subject. In contrast, oxyhemoglobin has a connection with oxygen, and is diamagnetic, which does not result in a detectable local magnetic inhomogeneity.
If a region in the gray matter of the central nervous system (brain and spinal cord) is activated, e.g., through sensory or painful stimulus, the blood vessels in the activated region will dilate. Then, the blood vessel contains more blood, resulting in a lower deoxyhemoglobin concentration. As a result, the tissue around the capillaries has fewer field inhomogeneities than before. A smaller field inhomogeneity increases the signal in T2* weighted measurements, so the intensity of the signal in a specific area increases while this area is activated.
The BOLD effect is an important imaging contrast for fMRI research in the brain [3], and is increasingly being used in the spinal cord [14] as well. The BOLD effect changes the signal in seconds; therefore, a fast acquisition method (e.g., echo planar imaging) is needed. However, the structure of the spinal cord is finer, and the signal-to-noise (SNR) geometric distortion of fMRI images is worse in the spinal cord. Therefore, fewer pieces of research are based on the BOLD effect in the spinal cord area. Combined brain and spinal cord fMRI studies are even rarer.

2.2.2 Echo Planar Imaging (EPI)

Echo planar imaging (EPI) is a fast MR imaging technique that was conceived by Mansfield in 1977 [31]. EPI acquires a whole data set of one complete image after a single RF excitation. Therefore, EPI is T_2^* weighted and a high-speed imaging technique. These two important characteristics make EPI the most important sequence for functional MRI techniques. The basic sequence of EPI and its k space trajectory are already shown and explained in figure **2-9**.
In this section we will focus on major shortcomings and limitations of EPI

Signal Loss

EPI samples the whole slice after one RF excitation. This characteristic is beneficial for the rate of data sampling. However, the signal amplitude of the center echo will be smaller with

time, as shown in the decay curve (red) in figure **2-9**a. As we know, the image intensity depends on the center echoes, and the signal amplitude is smaller if the echo time (TE) is longer. Therefore, the intensity of the image is worse. If we have a larger number of echoes or the gradient strength is weaker because of the hardware limitations, the echo time is longer. Therefore, reducing the echo time is a good possibility to reduce signal loss.
Another problem leading to signal loss is the field inhomogeneities. These field inhomogeneities result in through-slice dephasing, which is explained in detail in section 4.1. A better shimming (refer to section 2.3.3) can improve the field homogeneities and reduce this signal loss.

Geometric Distortion

After a selective slice excitation, the spatial information for the EPI sequence is encoded by frequency encoding and phase encoding. However, if the magnetic field in the frequency encoding or phase encoding direction has field inhomogeneities, it is an additional frequency encoding or phase encoding with unknown parameters accumulating incorrect spatial information. Therefore, the higher the number of echoes, the more pronounced the geometric distortion for the phase encoding direction because the effect of field inhomogeneity accumulates during every phase encoding gradient. To improve this, we can either use a better overall shimming (refer to section 2.3.3) or reduce the number of echoes for the same image resolution so that there is less accumulation of incorrect encoding.

2.3 Standard EPI Optimization Methods

The methods introduced in the following subsections address and optimize some problems of EPI. Some of these methods can also be used for the optimization of other MRI sequences.

2.3.1 Parallel Imaging (PAT)

Echo planar imaging often uses the parallel imaging technique (PAT) to speed up the acquisition. As mentioned in section 2.1.3, the signals are received by multiple coil elements. PAT is based on the acquisition of multiple coil elements with different spatial sensitivities; the relative signal amplitudes reflect basic spatial information that can be used to skip gradient encoding steps and thus reducing the number of echoes required, which shortens the echo train and increases the speed for phase encoding steps.

Aliasing

As we know from section 2.1.5 of k space, every sampling point in k space contains the information of the whole image. If we do not have enough sampling points, the frequency could be incorrectly estimated, as shown in figure **2-11**. In this example, a higher frequency

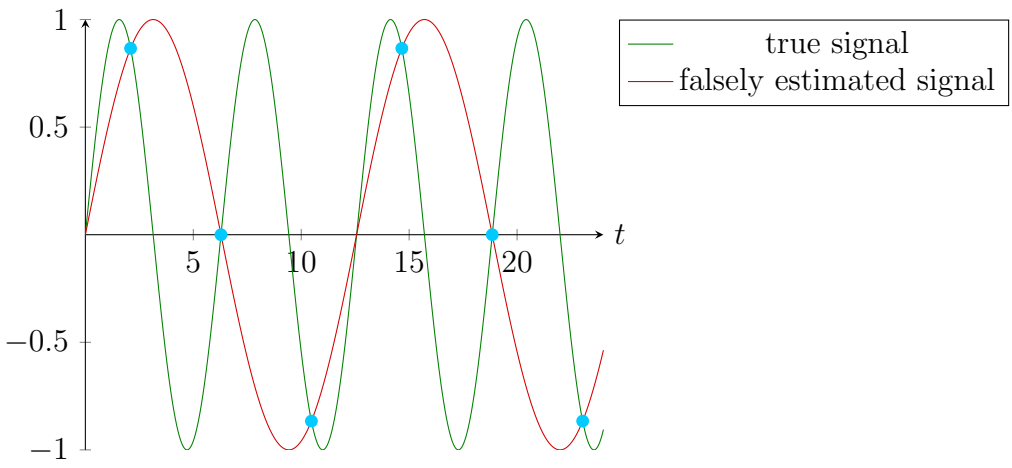

Figure **2-11**: Inadequate sampling example results in aliasing. The light blue points show the sampling points

is the correct frequency, but a lower frequency is estimated because of the missing sampling points.

Therefore, in the condition of the exact spatial resolution in phase encoding direction, the sampling distance Δk is inverse proportional to the desired field of view (FOV) $\Delta k_{\mathrm{PE}} \propto \frac{1}{\mathrm{FOV}_{\mathrm{PE}}}$. As a result, if we increase the sampling distance Δk, we will have a smaller FOV in the phase encoding direction. However, because the whole information of the object is still acquired, there will be an overlap in the image if the object size is bigger than the FOV, as shown in figure **2-12**. Due to the aliasing problem, it is impossible only to reduce the sampling rate to speed up the acquisition.

Coil Sensitivity

PAT uses the sensitivity of the coils to encode the spatial information roughly because the signals from different spatial positions give different amplitudes of the signal for the different coil elements, as shown in figure **2-13**. This figure shows the signal at different positions: in the middle and at the border. Different coils will receive different intensities of the signal depending on where the coil is. In the example with a signal source point in the middle of the object, the middle coil (4th) will have the strongest signal from this target point. In the example with a target point at the object's border, the 2nd coil from the left will receive the highest signal from this target. There can also be the case that two coils receive the same amplitude of signals for one target point. Then we know that the signal source point is in the middle of two coils. This example is only a simplified illustration.

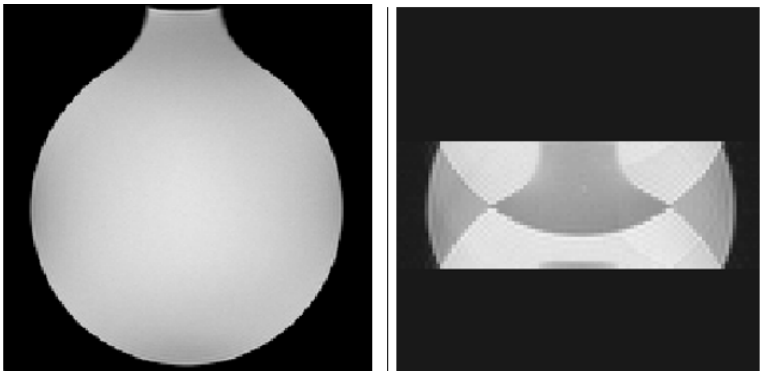

Figure **2-12**: Example of aliasing in a water phantom. While the image (left) has no aliasing effect due to a sufficiently large FOV, the image (right) shows an aliasing effect to overlap the image because the FOV is smaller than the in-plane size of the object. (From Chu, 2019[6])

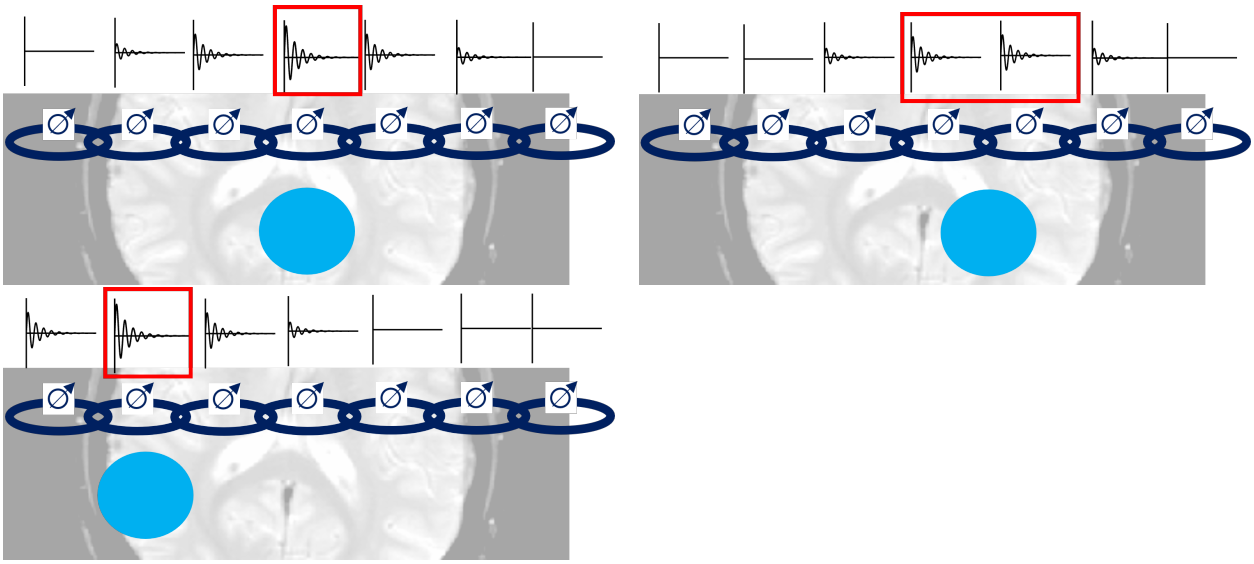

Figure **2-13**: Explanation for sensitivity differences between different coils. The FID signal shows the amplitude of each coil. The icon with a voltage indicator shows the position of the coil. The big blue point shows the signal source for the illustrated voltage indicator.

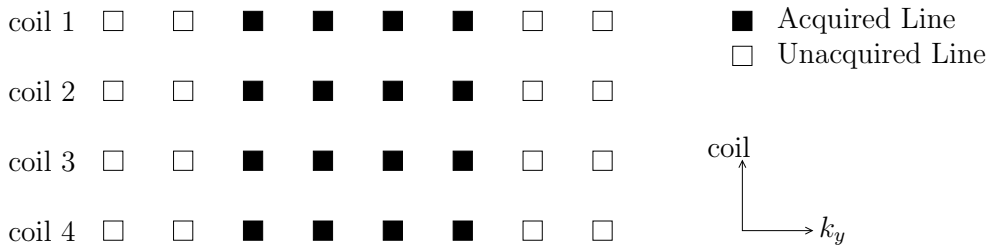

Figure **2-14**: The first step of GRAPPA is a calibration scan with fully sampled center lines in k space as auto-calibration signal (ACS) lines. Every square indicates one frequency encoded line in the k space.

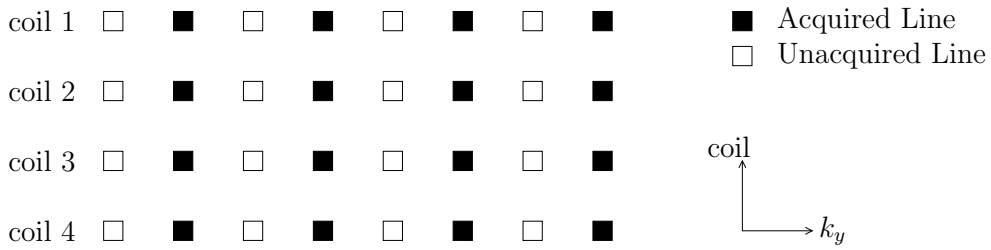

Figure **2-15**: The second step of GRAPPA is under-sampled raw data in k space

GRAPPA

GeneRalized Autocalibrating Partially Parallel Acquisition (GRAPPA) is a parallel imaging technique using undersampled k space. The GRAPPA method first fills missing data in k space, then the image is reconstructed with the fully filled k space.
First, a calibration scan with a full sampling of central k space is done as shown in figure **2-14**. The weighting factor between each line from every coil is calculated using the scanned acquired lines in the calibration scan. An undersampled k space image can be acquired as shown in **2-15**. Every missing line can then be estimated using the weighting factor, calculated from the calibration scan, as shown in figure **2-16**. It needs to be mentioned, that data from multiple lines from all coils are used to estimate the missing lines in each coil. After moving the kernel over the whole k space, all missing lines in the k space can be estimated as shown in figure **2-17**. The illustration only showed one variant of the kernel size and target position. However, the size of the kernel, the number of weighting factors used, and the target missing line position within the kernel are all variables.

2.3.2 Simultaneous Multi-Slice (SMS) Imaging

Simultaneous multi-slice (SMS) imaging [37][2], is a tool to accelerate fMRI imaging. This method uses multi-band RF excitation to simultaneously excite multiple slices with separated frequency bands. Similar to PAT, different receive-coils with different spatial sensitivities are

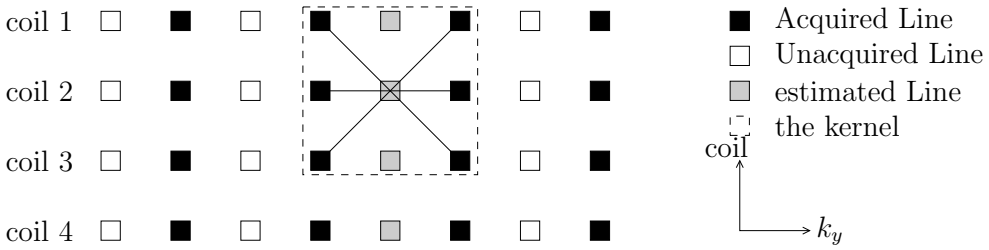

Figure **2-16**: GRAPPA's third step is fitting the measured lines to the ACS lines and then to estimate the missing lines.

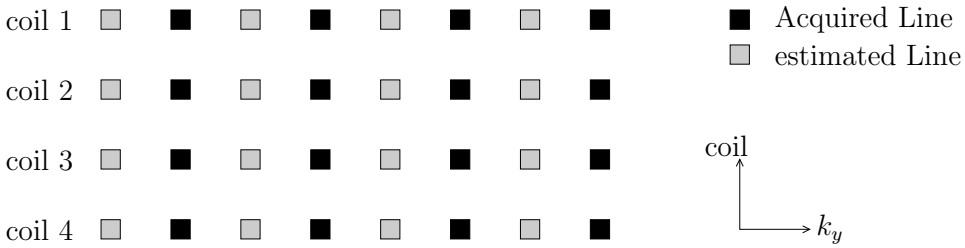

Figure **2-17**: The fourth step of GRAPPA is to use the fully filled k space to reconstruct the image normally.

needed (c.f. **2-18**a) to reconstruct the different slices separately. As shown in figure **2-18**b, from the upper coil's observation, the upper slice have higher intensity. From the observation of the lower coil, the lower voxels have higher intensity. Therefore, after we acquire the data for n slices together, we could split the image of the n slices in the reconstruction steps.

Blipped-CAIPI

The widely used simultaneous multi-slice (SMS) technique is the blipped-controlled aliasing in parallel imaging (blipped-CAIPI) [37] technique, which is also used as the SMS technique for this thesis. Blipped-CAIPI realizes apparent spatial shifts in the phase-encoded direction for simultaneously excited EPI slices to improve the performance of the reconstruction. To achieve simultaneous excitation, we need to apply multiple single-band RF pulses with different frequency offsets. Extra gradients in the slice direction needed to be added. The gradient magnet modulates the phase of multiple slices to shift the slices that were simultaneously excited by the multiband RF to help separate them. Figure **2-19** shows an example of shifts of FOV/3 in the phase encoding direction between three simultaneously excited slices. One slice is at the isocenter; another two slices are located at different off-isocenters. One additional feature of the blipped CAIPI is that only a small prewind-blipped gradient (shown as red in figure **2-19**) is used as the first blip, which makes sure the phases for the edge of all simultaneously excited slices switch around 0.
After the data acquisition, the image is reconstructed using a slice-GRAPPA algorithm[37],

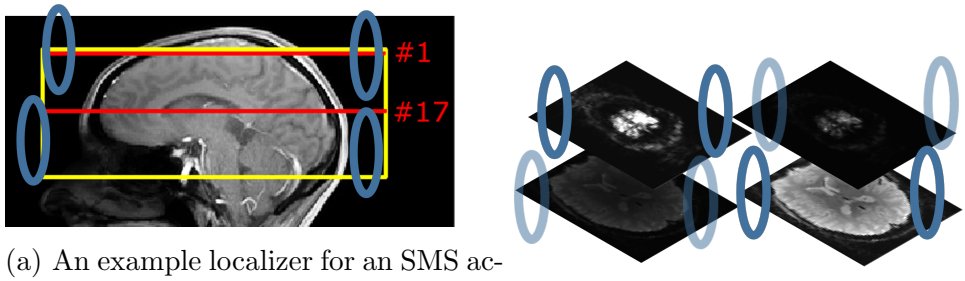

(a) An example localizer for an SMS acquisition with a nearly whole brain coverage (yellow block). Two separate slice examples are shown.

(b) Shown from different coil element positions, the sensitivity for different slices is different.

Figure **2-18**: Illustration of coil sensitivity for SMS technique. The ellipse shape (dark blue) indicates the position of the coils. The faded blue ellipse indicates ignored coils for image reconstruction shown here.

with a kernel from reference single-band data. For this thesis, existing SMS acquisition sequences and reconstruction algorithms had to be modified and adapted.

2.3.3 Shimming

Shimming makes the magnetic flux density (B) more homogenous, which is especially important for the T2* weighted imaging technique because it uses the field homogeneity differences as contrasts. In general, field homogeneities are important for spatial encoding. A worse homogeneity results in signal loss and geometric distortion (refer to sections 2.2.2 and 2.2.2).

Passive Shimming

To reduce field inhomogeneity, passive shimming is used. For passive shimming, small pieces of ferromagnetic materials are arranged and fixed inside the scanner bore.

Active Shimming

Passive shimming is not sufficient to reduce field inhomogeneity induced by the different susceptibilities of the object inside of the scanner. Therefore, active shimming usually is needed and used for in vivo scans. Active shimming uses currents through coils to compensate the unwanted field inhomogeneities.
To correct the B_0 field inhomogeneities, the standard scanner method needs to acquire a field map. The field map shows the static magnetic field distribution (B_0). If the field map is acquired while the subject is in the bore, the specific unwanted magnetic field can be identified. Then, it can be fitted with the opposite harmonic created from the shim coil. The standard scanner normally uses gradient field offsets to consider linear shim. The spherical

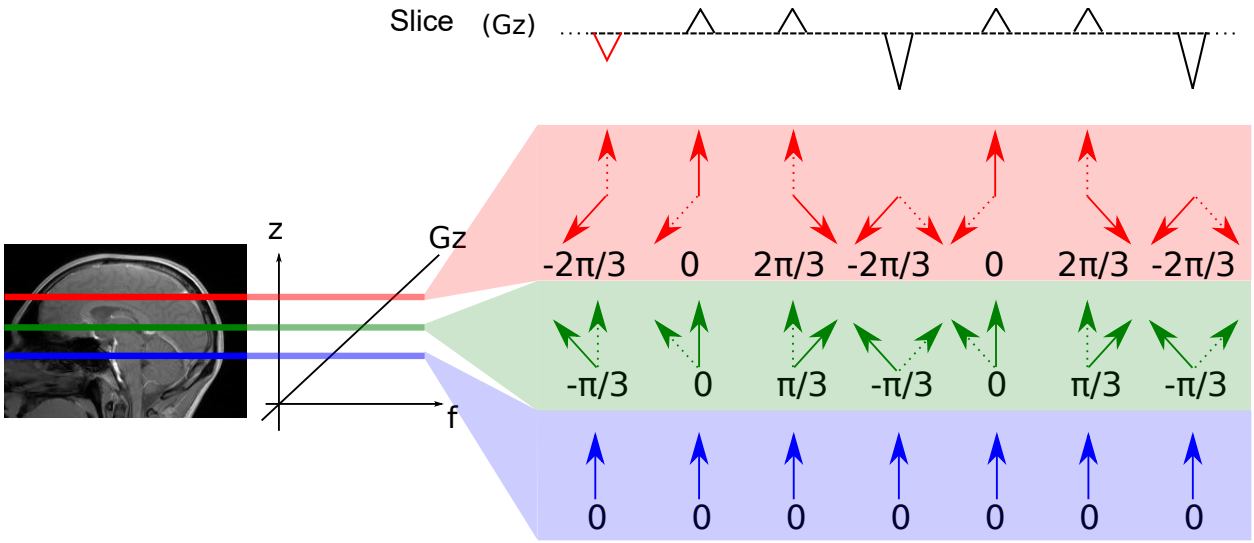

Figure **2-19**: Creation of FOV/3 shifts between three simultaneously excited slices (red, green, and blue) in the localizer image on the left. Due to different slice positions, the three slices have different phase development through the influence of the blipped gradient on the slice selective axis. The first negative red blip gradient is a prewind-blip gradient. The arrows with solid/dashed lines show the phase position after/before the blipped gradient.

harmonic (second-order shim) is usually corrected with extra coils. Typically, they are z^2, zx, xy, yz and $x^2 - y^2$ components.

Figure **2-20** shows the identification and correction of a field inhomogeneity in a target region, which is normally the FOV of measurement. After the standard active shimming process, the target region is more homogeneous but still does not have perfect homogeneity because the harmonic of the shimming is limited.

2.3.4 z-shim

As shown in figure **2-20**, the magnetic field may still not be perfectly homogenous after a general shimming, especially for a significant area of the spinal cord, because of the susceptibility difference between vertebrae and the intervertebral disc. There is a strong field inhomogeneity in the through-slice direction, which can result in slice dephasing. This means that the isochromats in the upper part of one slice can be in the opposite direction compared to the lower part of the same slice. As a result, less signals can be detected. To address this problem, z-shim can be used. Slice-specific z-shim gradient pulses [18] can help the signal loss problem in the spinal cord. It [18] introduces a method that uses a gradient pulse to compensate for the through-slice dephasing effect to reduce signal loss in spinal cord acquisitions.

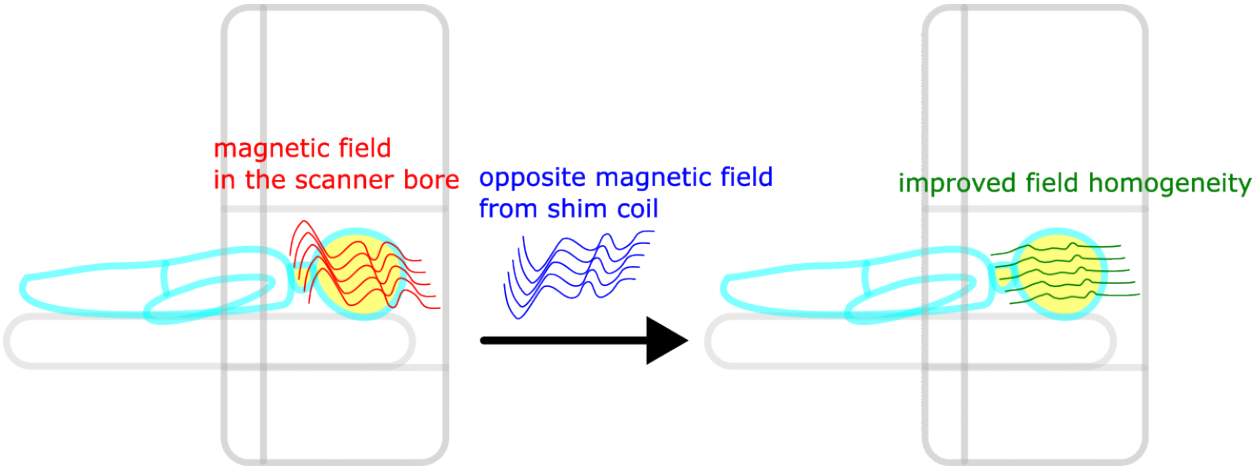

Figure **2-20**: The magnetic field (red) after the head of a volunteer is placed in the center (isocenter) of the magnet bore is shown in the left image. Then, the opposite magnetic field can be calculated. However, because of the limitation of harmonic terms, the magnetic field from the coils (blue) is not perfectly opposed to the measured magnetic field. As a result, the shimmed volume usually does not have a perfect magnetic field homogeneity but only an improved field homogeneity (green).

2.4 Combined T2* Weighted MRI of the Human Brain and Cervical Spinal Cord

This section will discuss the motivation and limitations of the combined fMRI imaging of the human brain and spinal cord. The limitations will only be discussed shortly here. The following chapters will show a detailed description and possible solutions for the limitations.

2.4.1 Motivation

Combined T_2^* weighted imaging of the human brain and spinal cord fMRI acquisitions aims to study interactions between the brain and spinal cord, for example, during painful or tactile stimulation[40] and motor output[4]. Only a few studies exist since the acquisition is rather challenging.

There are some limitations to brain and spinal cord combined fMRI. The sequence diagram of the Echo-Planar Image is shown in figure **2-21**.

In the frame of this thesis, solutions are presented to these limitations in the other chapters. The aim of this thesis is to improve the image quality and the usability of the combined fMRI of the brain and spinal cord.

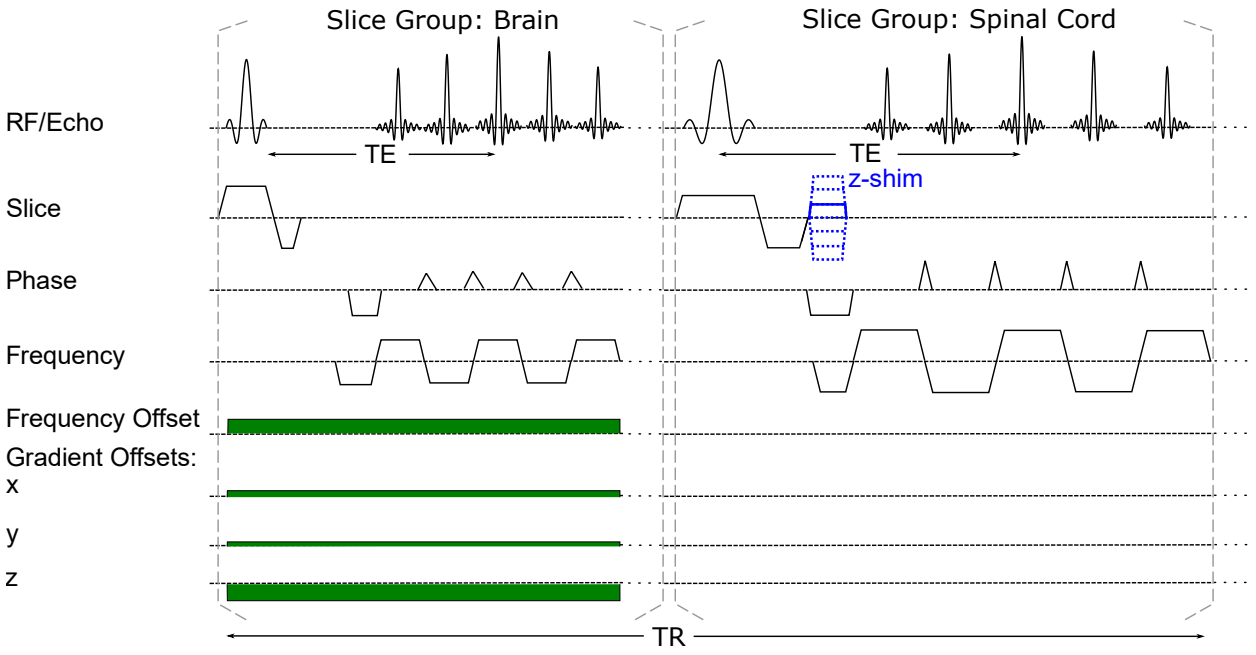

Figure **2-21**: The sequence diagram of a brain and spinal cord combined EPI with region-wise dynamical updated first order shim. When brain slices are acquired, gradient and frequency offsets (green) are considered. For the two groups, different resolutions, FOVs, and timing parameters are used. The repetition of the slice excitation is shortened as (...) on the axis.

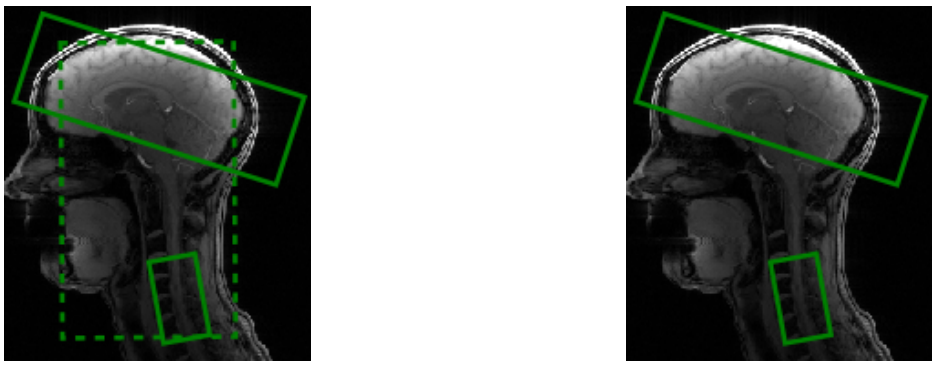

(a) "Conventional" region-wise shim. An extra "full" adjustment volume (dashed, green) is used for the 2nd shim.

(b) Dedicated "Cospi" shim

Figure **2-22**: Localizer with adjustment volumes for the "conventional" and dedicated "cospi" shim. The green cuboid adjustment volume defines the volume that should be shimmed.

2.4.2 Conventional Shimming Process

For the image quality, a big shimming volume to cover the two regions is not ideal because the volume in-between will also be covered, which means that unnecessary volume will be covered, which results in not precise results.
A workaround, "conventional" region-wise shim based on vendor's algorithm, was introduced before[19]. However, the vendor's procedure can only have a single cuboidal adjustment volume. Therefore, for the "conventional" region-wise shim approach, shim volume needs to be defined multiple times with adjustment volume, which is error-prone. And the second-order shim comes from a big shim region (**2-22** dashed green), independent from the first-order shim comes from an individual adjustment volume (solid green) as shown in figure **2-22**. The frequency offset and the linear shim are shown in figure **2-21**. Therefore, the "conventional" region-wise shim does not provide the optimal 2nd order shim for the fitted 1st order shims of two target volumes.
Therefore, within the framework of this work (chapter 3), a dedicated algorithm for region-wise shimming named "Cospi" shim is implemented and tested. The adjustment volumes for "Cospi" shim are shown in **2-22**b.

2.4.3 z-Shim in Spinal Cord

Because shimming until the second order cannot compensate the high-order harmonic due to the influence of the surrounding tissue, e.g., the alternation of vertebrae and intervertebral disc, the field inhomogeneity along the slice direction cannot be easily compensated by a shimming process for the whole volume. Moreover, the slice thickness is also quite big;

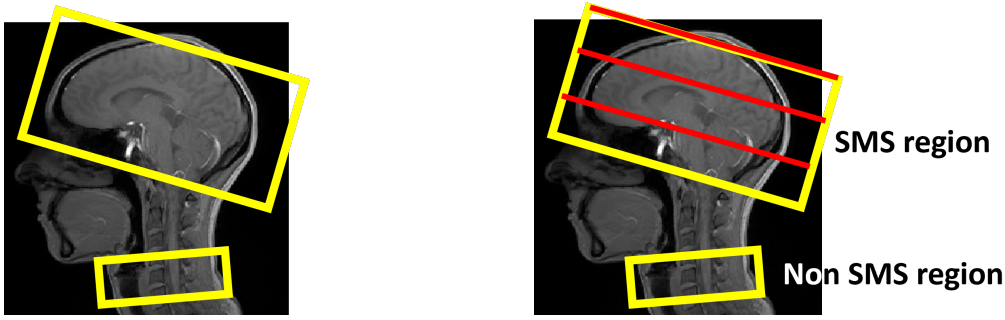

(a) Longer repetition time (TR), worse time resolution.

(b) Shorter repetition time, better time resolution.

Figure **2-23**: Localizer images. Yellow blocks indicate the volumes covered area. Red lines indicate the simultaneous slices.

therefore, there is a through-slice dephasing effect, resulting in a signal loss in spinal cord images. The signal losses due to the through-slice dephasing in spinal cord fMRI can be reduced by slice-specific z-shim[18]. Conventionally, the optimum values for the slice-specific z-shim are determined from a reference acquisition covering a series of z-shim values (dotted blue gradients, see figure **2-21**) by a user who needs to find the image with the least signal loss (e.g., solid blue gradients). However, this approach requires some experience, is time-consuming, and is user dependent.
Therefore, in this work, a user-independent automatized calculation of the optimum z-shim (refer to chapter4) gradient pulses has been developed and implemented on the MR system, and the results have been evaluated.

2.4.4 Volume Coverage and Temporal Resolution

Due to the requirement of high coverage in the brain and spinal cord region, the time resolution is rather high (about 4s). However, due to the different orientations of these two volumes and different slice thicknesses, therefore, the simultaneous multi-slice [37] technique can not be used directly. It is also not feasible to have the simultaneous multi-slice technique in spinal cord volume with fewer slices because of the insufficient coil elements.
Therefore, in chapter 5, the simultaneous multi-slice acquisition for brain volume only is implemented and tested to improve the temporal resolution and/or volume coverage of the combined fMRI. The SMS for brain volume only uses the SMS technique [37] to accelerate the brain region only but not the spinal cord region, as shown in figure **2-23**.

2.4.5 Retrospective Reconstruction

The in-plane resolutions and echo spacings differ for the different volumes, which results in different gradient trapezoids, as shown in figure **2-21**. However, the standard MR system's

reconstruction cannot handle different values for these parameters. As a result, some reconstruction steps, like regridding of data points acquired during the gradient ramps and correcting the Maxwell terms, will only work correctly for one of the two regions on-the-fly. In previous studies, a workaround method was a retrospective reconstruction of the other volume with the incorrect parameters reconstructed during the experiment. However, this method is error-prone and time-consuming because it requires the manipulation of parameters in the files used to configure the reconstruction. Furthermore, during the additional reconstruction, no acquisition can be performed, which means it blocks the MR for up to 25 min for typical fMRI studies [40], making the combined fMRI for the human brain and spinal cord less practical.
To overcome this limitation, the reconstruction was extended to an on-the-fly reconstruction with the correct parameter sets for both volumes measured, this reconstruction is implemented and tested (see chapter 6).

2.4.6 Navigating Spine Movement

The cervical spinal cord moves along the spine direction during swallowing and intense respiration, which can worsen the data, and makes the reference acquisition-based z-shim approach non-optimal. The in-plane resolution of the spinal cord is about 1mm×1mm, but the slice thickness usually is more than 3.5mm. Due to the transverse orientation and the high in-plane resolution, movement is easy to detect and correct in the fMRI data. However, the motion along the spinal cord's axis is difficult to recognize because the cross-section at different positions is very similar.
As a workaround, spine movements are usually used as a proxy for spinal cord movement. However, with thick slice thickness, the movement can not be estimated precisely. A navigator scan of a columnar volume along the spine axis will be introduced in chapter 7. This columnar volume can estimate the spine movements in the spinal cord's direction with much better spatial resolution.

2.5 Standard Parameters for Experiments

The measurements performed within this thesis used a 3T whole-body MR system (Magnetom PrismaFit, Siemens Healthineers, Erlangen, Germany) and a standard 64-channel head-neck coil.
For in vivo experiments, volunteers were investigated for the in vivo experiments after their informed consent was obtained. The phantom measurements were conducted by arranging doped water phantoms provided by the vendor
Unless stated otherwise in individual chapters, EPI acquisitions were performed with the following parameters which are typically used in previous combined fMRI studies.

For the brain volume, the slices have a FOV of 256×256mm^2. The voxel size of brain slices is 2.0×2.0×2.0mm^3. The receiver bandwidth is 2056Hz per pixel, which yields echo spacings of 0.59ms.
For the spinal cord volume, the slices have a FOV of 128×128mm^2, and the voxel size is 1.0×1.0×5.0mm^3. The receiver bandwidth is 1220Hz per pixel, which yields echo spacings of 0.93ms. There are no gaps between the slices. Two regional saturation pulses (see figure **3-3**) were used for every spinal cord slice to prevent residual aliasing, especially for the chin region.
For both brain and spinal cord volume: The phase encoding direction is from anterior to posterior. For the in-plane acceleration of the EPI image, the parallel acquisition technique is used with a factor of 2 (GRAPPA, 48 reference lines acquired in a single extra shot). The technique is explained in section 2.3.1. For the acceleration of the image acquisition, a 7/8 partial Fourier encoding is also used in the phase-encoding direction. Before each slice excitation, fat saturation was performed to avoid the signal from fat. Otherwise, the fat signal will also be detected and lead to an artifact because the Larmor frequency of fat protons is slightly different from that of water protons. These parameters yield an acquisition time for each slice of 63.8ms for the brain and 87.5ms for the spinal cord. An isocenter in the near spinal cord volume is needed, which improves the overall shim performance.

3 A Dedicated Algorithm for Region-Wise Shimming

Shimming is necessary for fMRI scans as discussed in the prior section 2.3.3. For combined T_2^* weighted imaging of the brain and cervical spinal cord fMRI, two measurement volumes, the brain and cervical spinal cord volumes, are defined as shown in figure **3-1**. The field of view in the cross section direction of the spinal cord is larger than the spinal cord itself because we need to contain the entire neck cross-section due to the aliasing effect explained in section 2.3.1. However, we only need a better field homogeneity in the spinal cord area because the field homogeneity only influences this area's spatial encoding. The field inhomogeneity of the nearby area must be low enough, that the image will not have such a strong distortion, that the image is larger than the FOV which could have aliasing. However, as the magnetic field is continuous, the magnetic field outside of the shim volume usually is not that inhomogeneous. Thus, for the spinal cord volume, we can only have a small shim volume to focus the spinal cord area.

3.1 Motivation of a Region-Wise Shimming

The standard vendor's setup only allows one shim volume. However, we have two separate volumes. Several options for the shim volume can be considered. If a big shim volume across the brain and spinal cord is used, we call it "full" shim volume. We can see from figure **3-2** that for the "full" shim volume, there is a significant geometric distortion on the anterior

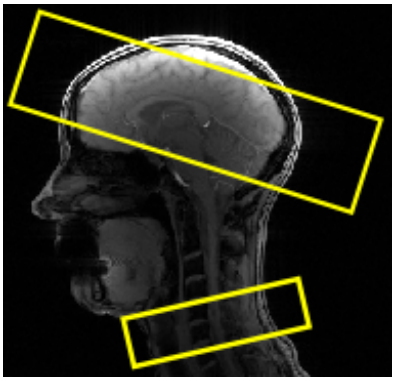

Figure **3-1**: Example of measurement volumes for combined fMRI

side of the brain image. The signal from the spinal cord area is low. This is because the distance between the two target volumes is large, therefore, the optimal shim setting can be different across the spinal cord and brain area, especially for the small spinal cord region. As known from section 2.3.3, the field homogeneity can not be corrected perfectly in every location due to the limited shimming harmonic. As a result, we cannot have a good image quality for both brain and spinal cord regions.

If we only shim the brain or spinal cord area, only the brain or spinal cord will have good image quality, but the other volume will be distorted or ghosted or will have an extreme signal loss. As shown in figure **3-2**, the spinal cord and the cerebrospinal fluid (CSF) have barely any signals for the "brain" shim volume images. And for the "cord" shim volume images, the brain image is strongly distorted. The results in phantom measurements also show similar results.

Therefore, in a previous study, region-wise shim approach with a dynamic update [19] for the linear shim has been used as a workflow that uses the vendor's shim approach. It uses the second order shim from the "full" shim volume, shown as the dashed green block in figure **3-2**, but uses a "dynamic" region-specific constant and linear shim setting on the spinal cord and brain areas. The results with the "dynamic" shim volume show that the EPI image quality is improved regarding signal loss, distortion, and ghosting.

3.2 Motivation of a Dedicated Algorithm for Region-wise Shimming

However, multiple operations of the shimming process for three different volumes: "brain", "cord", and "full" shim volumes are needed for this shim approach. And there is a requirement of manual changes of the shim setting and frequency adjustment, making it time-consuming, cumbersome, and error-prone. Furthermore, another issue of this method is that the linear and second-order shim terms of different shim volumes are mixed. The second-order shim terms come from the "full" volume, and the first-order shim terms come from the particular shim volume. Therefore, the shim results are not optimized perfectly, resulting in geometric distortions and signal losses. [19]

These issues are addressed with a dedicated region-wise shim algorithm for the combined fMRI. We use the term "CoSpi" shim, short for "Combined cortico-Spinal" shim. The "CoSpi" shim optimizes the region-specific linear and a joint optimization of static second-order shims in one step. It is easier to use and provides better field homogeneity in the target region, reducing signal loss and geometric distortion.

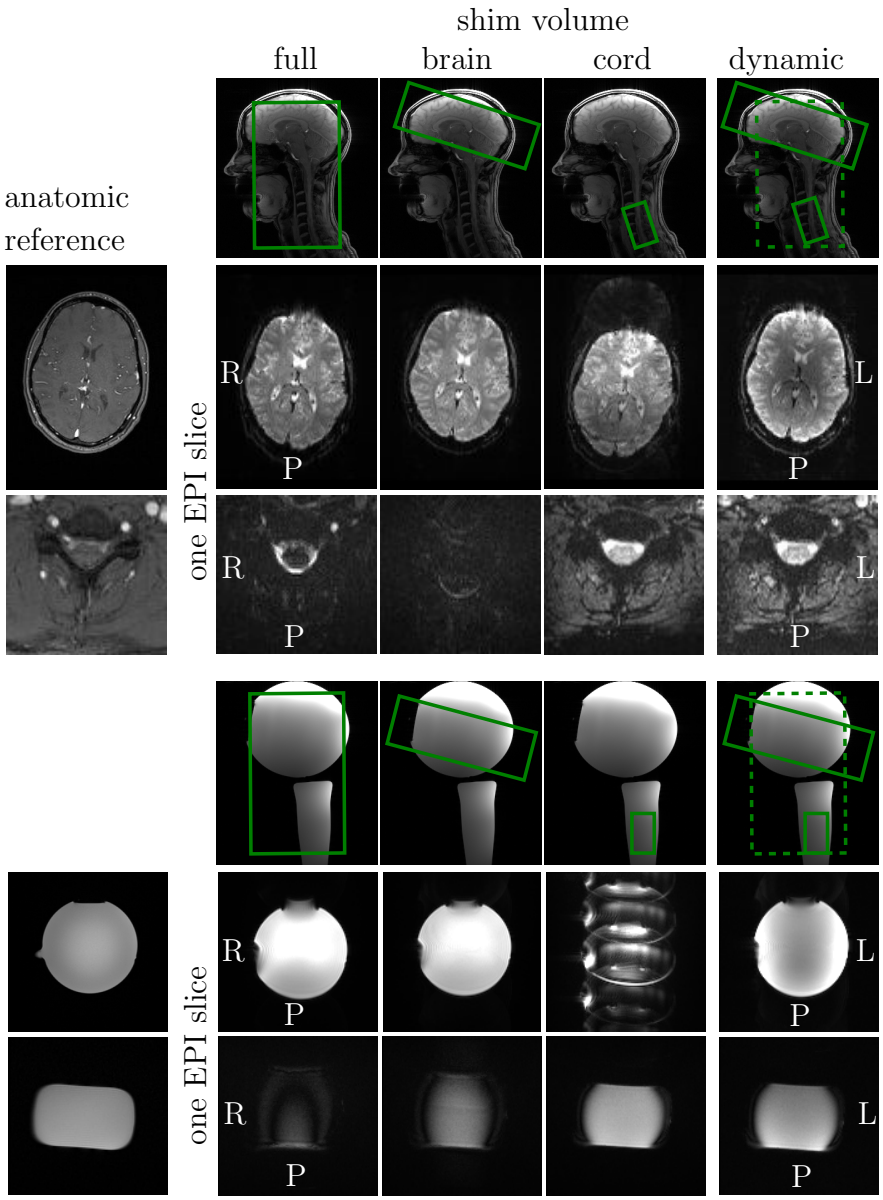

Figure **3-2**: EPI images and their anatomic references (FLASH) in brain and spinal cord with different adjustment volumes: in vivo (upper) and in phantoms (lower). The position and form of the phantoms mimic the in vivo setup. The shim volumes' positions and sizes (green block) are shown in the localizer images (first rows of in vivo and phantom image blocks). (from Chu et al., 2023[12])

3.3 Method

3.3.1 Setup

The basic setup with two separate measurement volumes is based on the previous pain processing studies which used thermal stimulation on the forearm [40] [39]. The setups with localizer images are sketched in figure **3-3**. For the setup (Fig. **3-3**a), there were two slice groups (yellow) defined. One slice group was located in the brain, which was centered in the corpus callosum and tilted by about 20° to cover the brain region that reacts to pain processing. Another slice group was perpendicular to the vertebral disc between C5 and C6. The center of this slice group is also the center of the spinal cord in the cross-section plane. The in-plane field of view and the voxel size was different for the two slice groups, which optimized the image quality of the brain and spinal cord target region. The "full" (dashed green), "brain" (top, green), and "spinal cord" (bottom, green) adjustment volumes covering the respective areas were defined. For the "CoSpi" shim algorithm, a field map (blue, $480 \times 328 \times 240 mm^3$) was also measured, which covers both target regions and contains the whole head. The phantom measurement (**3-3**b) is set up for a more controlled experiment that is not influenced by motion and physiological noise.
The T2* weighted images of the two slice groups were acquired with EPI. The basic sequence of the EPI measurement is shown in figure **2-21**. The name of the dynamic shim update comes from the on-off of the frequency and gradient offset. The motivation for using a separate volume is discussed in 2.4.1, and the motivation for using the dynamic shim update to acquire a better image quality is shown in section 3.1.

3.3.2 Dynamic Shim on Sequence

The sequence diagram (Figure: **2-21**) shows that the constant (frequency f) and linear (x, y and z gradient fields) shim terms can be changed during the acquisition. However, the second-order (xy, xz, yz, z^2 and $x^2 - y^2$) shim terms cannot be changed quickly during the experiment because of the eddy current and power supply constraints. Therefore, a dynamic update is limited to 0th and 1st order.
For the brain and spinal cord acquisition, the shim interface of the MR system allows the input of the five second-order shim terms and three linear-order shim and frequency settings. We use the 9 shim terms above from the spinal cord adjustment volume as the nine "static shim parameters". During the acquisitions of the slices in the brain volume, the sequence adds "dynamic shim offsets"(green in figure **2-21**) with zeroth- and first-order shim settings for the brain slices. The shim terms are from the vendor's shim procedure for the conventional shim approach [19]. For the "CoSpi" shim procedure, the dedicated shim algorithm calculates the shim setting with the acquired field map. For both approaches, 13 shim terms (nine "static": $f_s p$, $x_s p$, $y_s p$, $z_s p$, xy, xz, yz, z^2, $x^2 - y^2$ and four "dynamic": $f_b r$, $x_b r$, $y_b r$, $z_b r$) are determined. The steps of these two methods are introduced in the next two sections.

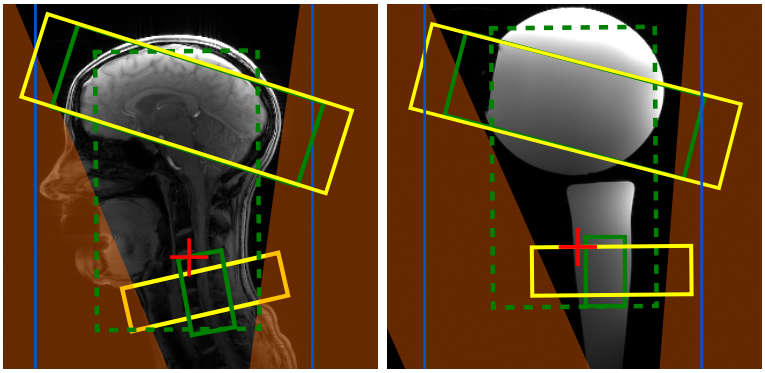

(a) Setup for in vivo experiments

(b) Setup in the phantom experiments. The arrangement of the phantom mimics the experiments in vivo

Figure **3-3**: Basic geometric setup for the data acquisition. The fields of view (yellow block) of the brain area with a volume of $256 \times 256 \times 71 mm^3$ and cervical spinal cord with a volume of $128 \times 128 \times 40 mm^3$ are shown. The "brain" adjustment volume (top, green) almost covers the field of view area of the brain. The "full" adjustment volume (dashed green) covers brain and spinal cord areas. The " spinal cord" adjustment volume (bottom, green) covers the spinal cord and is slightly taller than the spinal cord FOV. Two saturation bands (orange) cover the chin and neck to avoid aliasing in the spinal cord target region. The isocenter (red cross) position is near the spinal cord field of view.

3.3.3 "Conventional" Shim Approach

The "conventional" shim approach [19] is based on the vendor's shim procedure which optimizes first- and second-order shim terms. However, it is limited to a single, cuboidal adjustment volume.

The system's shimming procedure started with a "tune-up" shim, which is predefined before the shim procedure. Then, the magnetic field distribution (field map) was acquired. After obtaining the field map, the shim parameters can be calculated and set. It is then typically still not homogenous enough, thus, a second round of field map acquisition, calculation, and setting has been done.

The steps to acquire the "conventional" shim setting for the combined measurement were the following:

First, for the five second-order shim terms, we use an "full" adjustment volume (dashed green in Fig. **3-3**).

Second, we use the "brain" adjustment volume (cf. Fig. **3-3**) to get the optimal first-order shim setting.

Then, we use the "spinal cord" adjustment volume (cf. Fig. **3-3**) to get the optimal first-order shim setting.

Next, combine the second-order shim terms from the "full" volume and the first-order shim terms from the "brain" volume as the "conventional" shim setting for the brain volume. And then use the frequency adjustment of the MR system to define the frequency of the brain volume.

Last, combine the second-order shim terms from the "full" volume and the first-order shim terms from the "spinal cord" volume as the "conventional" shim setting for the spinal cord volume. And then use the frequency adjustment of the MR system to define the frequency of the spinal cord volume.

The "conventional" shim settings for the spinal cord volume were used as the static shim setting. The dynamic shim update setting is the difference between the shim settings for spinal cord and brain volume. The dynamic shim update should be applied during the acquisition of the brain slice group as shown on the sequence diagram **2-21**.

The "conventional" shim approach was used in several cortico-spinal fMRI studies[40][39]. It provided a high image quality in both target regions (as shown in column "dynamic" in Fig. **3-2**). As a result, it was chosen as the primary reference in this study.

The optimal shim settings for each volume are obtained while obtaining the "conventional" shim setting. These settings are considered the "gold standard".

The "conventional" region-wise optimization has two limitations. Firstly, it fails to produce optimal shim settings because the linear terms used for the target regions are combined with second-order shim terms optimized for a different volume ("full" volume) with different linear shims, resulting in residual geometric distortions and signal losses. This is because the vendor's shim algorithm can only optimize both orders for the chosen single

cuboid adjustment volume. Secondly, the procedure is complex and time-consuming, which increases the chances of errors, mainly because linear- and second-order shim settings must be stored and changed multiple times. Therefore, this method requires skilled and trained users and sufficient time for fMRI studies to execute the entire process before the functional experiments.

3.3.4 "CoSpi" Shim Approach

Figure **3-4** outlines the fundamental workflow of the "CoSpi" shim algorithm. The algorithm was implemented in IDL (version 8.8.0, L3Harris Geospatial, Broomfield, CO, USA).
As shown in the red block of figure **3-4**, inputs are needed for the algorithm. They are:

- The magnitude and phase differences of a field map measurement that covers the target regions, together with the related acquisition parameters and shim settings, including the "tune-up" shim.
- The desired adjustment volumes for the brain and spinal cord regions and their position and orientation (shown as green blocks).
- The adjusted frequencies for the two adjustment volumes (shown as "adjusted frequencies (f_1 and f_2)"). The shim settings need to be the same as the "tune-up" shim which has been used for the field map acquisition as well.
- An intensity threshold is needed, which is shown from the following: the histogram in figure **3-5** shows that a lower intensity threshold of 100 for the field map is typically about 35% lower than the minimum intensity in spinal cord tissues.

After collecting the necessary inputs, the voxels from the magnitude field map outside of the adjustment volumes, and the voxels inside of the adjustment volumes with an intensity smaller than an intensity threshold, are discarded. We obtain the "volume + intensity mask". Then, its binary mask ("phase mask") is created and used on the phase difference map. Next, an unwrapping process on the phase difference image can be performed on the remaining voxels. The algorithm is independent between the two adjustment volumes. The phase unwrapping process begins at the geometric center of the corresponding adjustment volume. However, if the voxel associated with this center has been discarded in previous steps, one of the closest remaining voxels is selected instead. Once the phase difference images have been unwrapped, they are scaled to reflect frequencies rather than phase differences ("relative frequency"). This process is called "scaling". After that, a "frequency match" needs to be done. The mean frequency of each adjustment volume is set to the experimentally determined frequency (f_1 and f_2 from the input). A "matched frequency" map can be obtained. It ensures that the mean frequency of the field map is related to the measured one by the vendor's system in each of the two volumes to relate to the frequency of the two separated volumes because of the discontinuities of the phase in the two adjustment volumes.

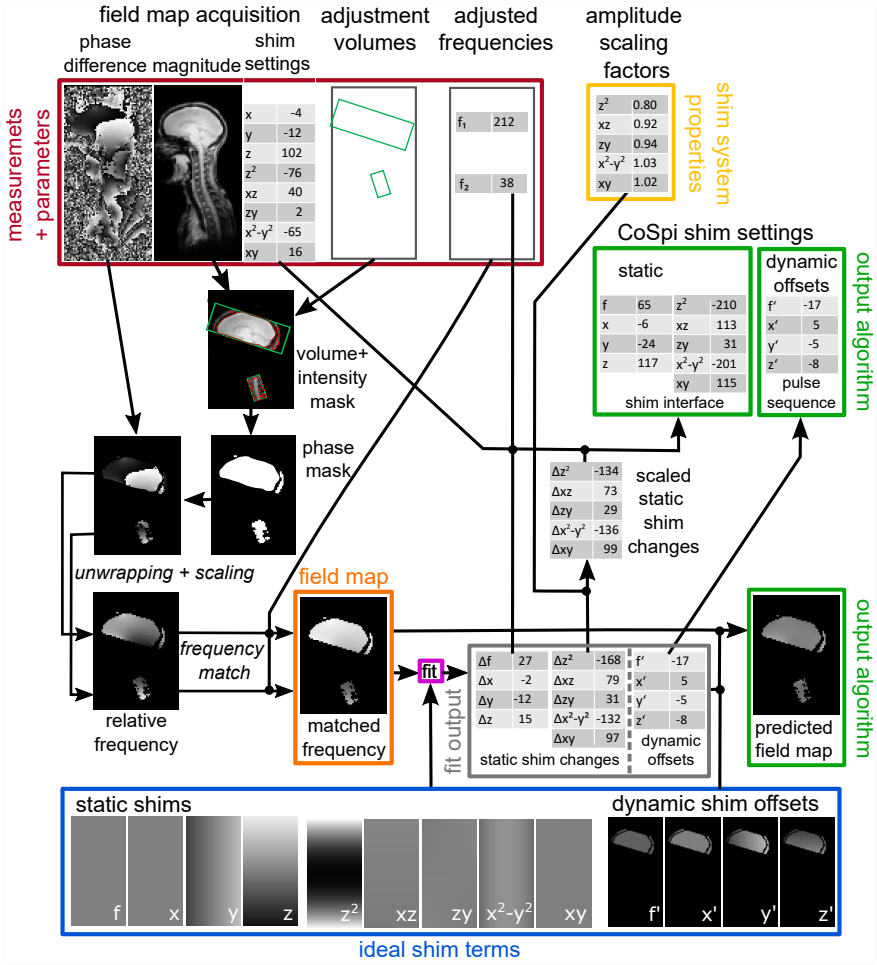

Figure **3-4**: The workflow of the CoSpi shim algorithm, which shows (i) the necessary input data for the particular examination (red), including a phantom reference acquisition (yellow) and pre-defined shim terms based on theoretical field distributions (blue), (ii) the outputs of the fit procedure (solid grey frame), and (iii) the CoSpi shim configurations and predicted field map as the final output (green). Each step displays the status of an in vivo example dataset. To obtain static CoSpi shim values, the "static shim changes" values need to be added to the "matched frequency" field map's shim settings, with the second-order values being scaled from the phantom reference first. Note that the shim setting values shown are solely for demonstration purposes and do not reflect actual values obtained in the present study. The 13 terms are scaled to show the distribution without a wrap. (Figure from Chu et al., 2023[12])

Then, the estimation of the shim settings can be done. The shim algorithm aims to minimize the field inhomogeneities in the two adjustment volumes. Therefore, the field distribution (blue block) with the isocenter as the identical origin for all shim settings is shown. The nine "static shims" terms (f, x, y, z, z^2, xz, zy, $x^2 - y^2$, xy) are defined for the whole volume of the field map. The four "dynamic shim offsets" terms (f', x', y', z') only exist during the acquisition of the slice group of the brain. Therefore, the field distribution outside of the brain adjustment volume is set to zero.
To fit the "matched frequency" map, the 13 shim terms were used. A Levenberg-Marquardt algorithm is utilized. No constraints were assumed, including maximum shim amplitude. Next, the sign of the fit parameters is inverted for the compensation of the field inhomogeneities to obtain the solid grey frame values, which represent the changes required for the static shim terms ("static shim changes") and the "dynamic offsets" of the brain-only shim terms. These values are then used to calculate the expected theoretic field distribution or a so-called "predicted field map" using the pre-defined shim terms. The values for the brain-only terms (f', x', y', z') directly reflect the "dynamic offsets" of the "CoSpi shim settings" (green frame) and are saved to a file that the pulse sequence can read.
The "amplitude scaling factor" scales the parameters of the changes for the second-order shim terms, resulting in the "scaled static shim changes". The "scaled static shim changes" and the first order "static shim changes"(Δf, Δx, Δy, Δz) can be added to the static shim values of the field map. Then, we have new "static" shim values for the "CoSpi shim setting" (green frame). The "dynamic offsets" do not need any further modification. The final "output" of the "algorithm" is shown (green frame).

3.3.5 Measurement Steps and Parameters

First, a localizer acquisition has been acquired, as shown in figure **3-3**. A localizer acquisition is a rapid low-resolution image that helps to localize the region of interest (ROI), shim volumes, and saturation area within the object.
After the localizer acquisition, a coronal orientation field map acquisition was performed using a 2D dual-echo FLASH sequence provided by the vendor with the "tune-up" shim settings. The acquisition parameters were as follows: field-of-view (FOV) 480× 480mm^2 (read × phase), 60 slices without gap, voxel size 4.0 × 4.0 × 4.0mm^3, echo times (TE) of 4.26/6.72ms (with an echo time difference fixed at 2.46ms), receiver bandwidth of 340Hz per pixel, repetition time (TR) of 583ms, flip angle of 40°, and a total acquisition time of 1 minute and 38 seconds. The acquired images, consisting of two magnitude images due to two echo times and one phase difference image, were transferred to the CoSpi shim algorithm.
The subsequent step is positioning the two slice groups, which had a gap range of 110-128 mm (with an average of 120 mm) between them for the five different volunteers, and positioning their cuboidal adjustment volumes for the cortico-spinal EPI acquisition. This is illustrated in figure **3-3**. A single EPI shot was acquired with the same shim settings

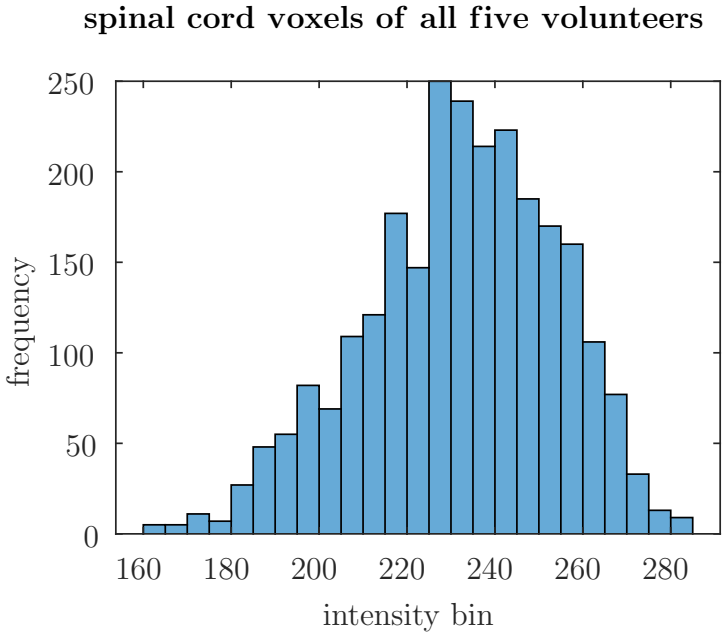

Figure **3-5**: The intensity of the pure spinal cord voxels (masked from the EPI acquisition with the spinal cord toolbox[22]) on the field map.

used for the field map acquisition for each adjustment volume. These measurements also included automatic frequency adjustment by the vendor's system before acquisition. The relevant image parameters, especially the adjustment volume parameters, were stored in the EPI image and then transferred to the CoSpi algorithm, providing the necessary parameters with a single step for each volume.

For the EPI acquisitions described above and all other EPI acquisitions in this chapter, the standard parameters from section 2.5 are used. The brain slice's echo time (TE) was 30ms, and the spinal cord slice's echo time (TE) was 31ms. Twenty-four slices were acquired in the brain with a gap between two slices of 1mm, yielding a 71mm stack thickness for the volume coverage. The spinal cord group acquisition involved eight slices in the spinal cord without any gap in between. Therefore, the volume coverage is 40mm in the slice excitation direction. The gradient must be ramped up and down for the dynamic shim update. Therefore, it adds an additional 2ms to the sequence. As a result, the minimum TR of these two slice groups is 2231ms.

We obtained anatomical reference data using 2D FLASH acquisitions, which covered the same slices as the EPI acquisitions, with a fixed field of view like the EPI acquisition and slice thickness and an in-plane resolution of $1.0\times1.0\text{mm}^2$ yielding a TE of 3.2ms, a TR of 7.5ms and a flip angle of 15°. Additionally, we performed a 2D MEDIC acquisition [38] to obtain spinal cord volume reference data with a voxel size of $0.5\times0.5\times5.0\text{mm}^3$ which yields a TE of 21ms, a TR of 307ms. The flip angle was 20°.

3.3.6 Analysis

This section will introduce the analysis steps for the results section. The distortion and tSNR were only analyzed in the brain and spinal cord volume because they are the regions that the fMRI is interested in.

Distortion

The name "voxel displacement map" indicates that the map calculates the voxel displacement from the EPI image by the related field map.
First, voxel displacement maps were calculated with the Field Map toolbox of SPM12 [20][25][21] based on the field map acquired with the corresponding shim settings and the EPI acquisition parameters of the respective volume. Next, masks of the target regions were determined.
For the brain slices, the magnitude images of the field map measurement acquired with the CoSpi shim settings were used to identify brain tissue/CSF voxels using SPM12 [20][1]. The bottom half of the field map had to be discarded to ensure that the algorithm identified the brain properly due to its unusual position (about 100 mm above the isocenter). Voxels of the mask outside the volume covered by the EPI acquisition were discarded. For the spinal cord slices, the EPI images (20 averages) were used to identify voxels with spinal cord tissue using the Spinal Cord Toolbox [29][23][22].
For the spinal cord area segmentation, EPI images were preferred due to the rather large in-plane resolution ($4\times4\text{mm}^2$) of the field map. In the uppermost spinal cord slice (slice 8), Spinal Cord Toolbox cannot identify the spinal cord for one of the five volunteers. Thereby, the data of this slice is based on only four volunteers. The obtained masks were used to evaluate the geometric distortions in the two target regions.

Temporal SNR

First, the maps of the temporal signal-to-noise ratios (SNR map), as shown in figure **3-10**a and figure **3-10**b, were calculated from the mean map divided by the standard deviation maps across 20 EPI acquisitions. The mean map is an averaged image over 20 successive acquisitions on the same slice, which will be calculated voxel by voxel. With the mean map and all 20 acquisitions, the standard deviation of each voxel over the 20 acquisitions can be calculated by $\text{Deviation}_{\text{x,y}} = \frac{\sum_1^n \left(I_{\text{intensity}(x,y)} - I_{\text{mean map}(x,y)}\right)^2}{n}$, where $n = 20$ due to the 20 acquisitions and x,y represent the position of the current voxel. After deviations of all voxels of one image are calculated, the deviation map over 20 acquisitions is obtained. By using $SNR_{(x,y)} = \frac{I_{\text{mean map},(x,y)}}{Deviation_{x,y}}$, the temporal SNR of each voxel in the MR image is calculated. The image with SNR values of all voxels is called an SNR map.
Slice-wise (tSNR_{Slc}) and region-wise (tSNR_{Vol}) temporal SNR averages were calculated. Both tSNR_{Slc} and tSNR_{Vol} only averaged the brain or spinal cord volume voxels from the brain

and spinal cord mask. The brain (white-, gray-matter, and CSF) mask was obtained from the averaged EPI acquisitions by SPM12 [20][1][21]. And the spinal cord mask was obtained by the Spinal Cord Toolbox [29][23][22]. In the uppermost spinal cord slice (slice 8), the Spinal Cord Toolbox can not identify the spinal cord for one of the volunteers. Hence, the data of this slice is based on only four volunteers.

3.4 Results and Discussion

The results are shown in quantity and quality with Field maps, EPI images, SNR maps, and voxel displacement maps.

3.4.1 Agreement Check of the Field Map

Phantom Figure **3-6** (a) shows the performance of the CoSpi method for the phantom setup regarding their field maps. It compares the tune-up and CoSpi field map, both predicted and measured. It also shows the difference map between the predicted and measured CoSpi field map, which gives us the impression that the measured CoSpi field map can be predicted because the predicted and measured field maps are similar. Compared with the tune-up shim, the measured field map has a much better field homogeneity. For the measured field map, the standard deviation of the separate volume is 28% less than the tune-up field map for the "brain" volume of the phantom; and 50% less for the "spinal cord".
Another important feature is that the predicted and measured field map has a similar field homogeneity, as the frequency changes are similar throughout the field map. The standard deviation value between the predicted and measured field map from the CoSpi method differed by less than 8%. On average, the measured field map has an increased standard deviation value of 4%, so, it has an increased field inhomogeneity. The difference maps shown in figure **3-6** have low mean values (0.1 Hz) and standard deviations (9.2 Hz) for the brain volume, indicating a very good agreement between the predicted and measured field data.
As for the spinal cord volume, the mean values and standard deviations of the difference field maps are 14.0 Hz and 1.3 Hz, respectively, indicating good agreement between the predicted and measured data in the phantom.
The agreement check in phantom shows that the predicted and the measured field maps are similar, and the CoSpi algorithm enhances the field homogeneity, therefore, in vivo experiments were also investigated.

In Vivo Now we focus on the in vivo results of figure **3-6**. For the in vivo experiment, the gain is even more significant. The standard deviation of the whole volume is reduced by 55%/60% (volunteer B/volunteer E) for the brain and by 63%/58% (volunteer B/volunteer E) for the spinal cord volume if we compare the field map of the measured CoSpi field map and the tune-up field map.

The difference maps shown in figure **3-6** for the in vivo measurement have low mean values (19.0/11.0Hz; volunteer B/volunteer E) and standard deviations (5.8/4.8Hz; volunteer B/volunteer E) for the brain volume, indicating a very good agreement between the predicted and measured field data.
The brain volume is expected to be more sensitive to imperfections of the shim terms due to its large distance to the isocenter, such as gradient non-linearities. Therefore, the parameter amplitude scaling factors used for second-order shim terms are reasonable and adequate for the hardware used in this study.
As for the spinal cord volume, the mean values and standard deviations of the difference field maps are –50.2/14.4Hz (volunteer B/volunteer E) and 26.0/7.3Hz; volunteer B/volunteer E, respectively, indicating a not-perfect consistency in the in vivo acquisitions between the predicted and measured data. However, both the predicted and measured field map has shown improved field homogeneity in comparison to the tune-up field map.

3.4.2 Comparison of the Field Map of Single Volume, CoSpi, and Conventional shim approach

This section compares the shim results between "single volume", "conventional", and "Cospi" adjustment volume. The field map from "single volume" uses the shim setting optimized for one of the two volumes only. The field map from the "conventional" adjustment volume is introduced in section 3.3.4 and the field map from the "CoSpi" adjustment volume in section 3.3.3. The "single volume" adjustment volume shim setting can only be used in single-volume EPI measurements, which is incompatible with the combined brain and spinal cord measurement. Therefore, we can use the field map from the "single volume" adjustment volume as the golden standard, the reference image.

Phantom Figure **3-7** shows that the field maps from the single volume have near-perfect field homogeneity, as the frequency changes are low throughout the field map. However, with the conventional approach, the sagittal and transversal field map images show a significant field inhomogeneity. Using the CoSpi approach, the field homogeneity improved compared to the conventional approach. These results show that in phantom measurements, the single-volume approach provides the best field homogeneity. However, the field homogeneity with the CoSpi approach is also satisfactory, which can be used for combined brain and spinal cord measurement.

In Vivo For the in vivo experiment, the difference between the conventional and CoSpi approach is even more significant. The field map with the conventional approach has much worse field homogeneity than the one from the single volume and CoSpi approach. For in vivo experiments, the field homogeneity of the CoSpi approach is comparable to the single-volume approach.

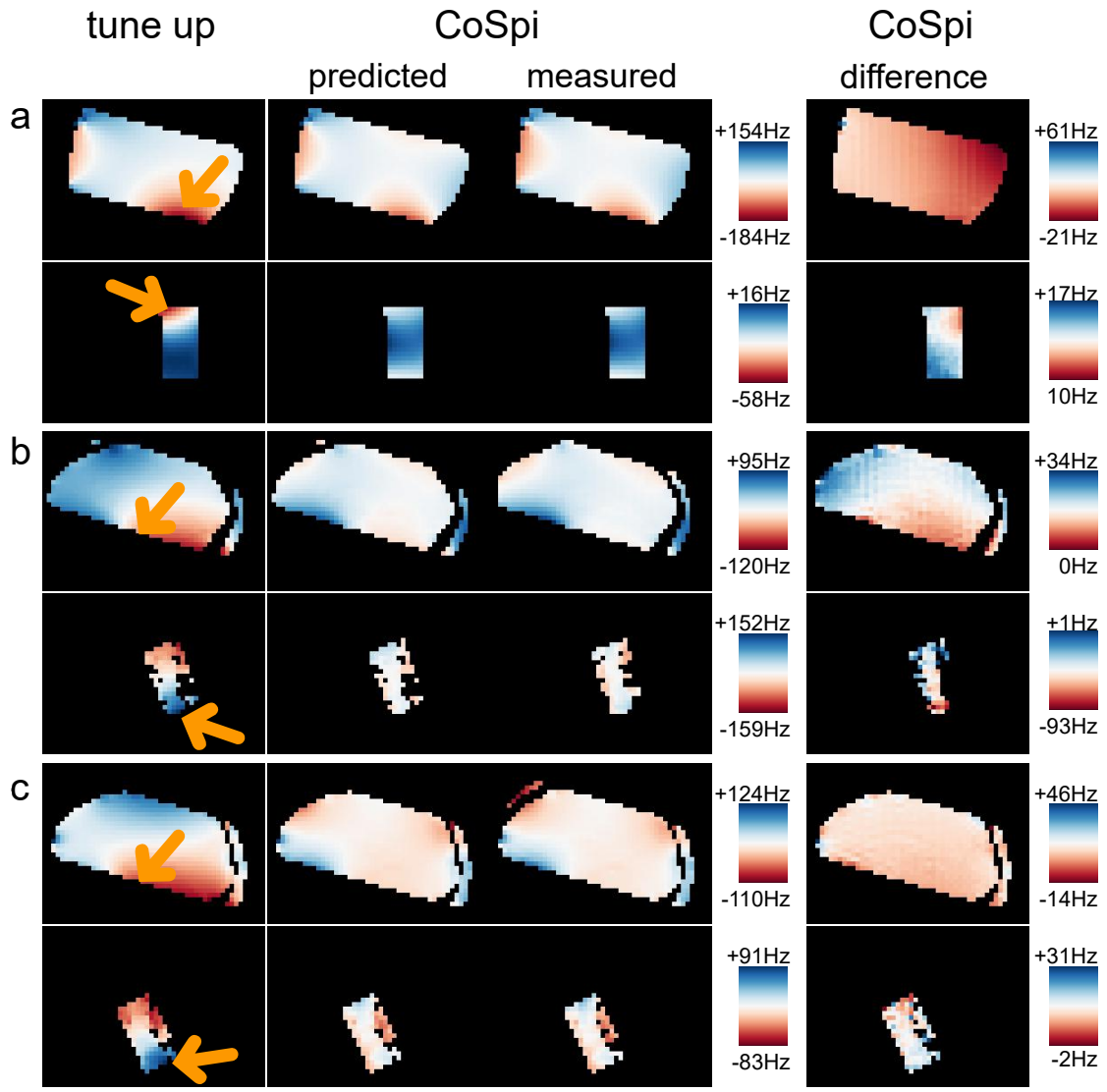

Figure **3-6**: Sagittal views of the B_0 field map of the masked brain and spinal cord adjustment volume. From left to right, the columns are the field map from the "tune-up" shim, the predicted field map from the CoSpi shim value, the measured field map from the CoSpi shim, and the difference between the predicted and measured field maps. The arrows show the location with enhanced field inhomogeneities. The field maps are from (a) phantom experiment, (b, c) in vivo from volunteers B and E. The number shown in Hz are the maximal and minimal frequencies of the field maps from the same row. (Figure from Chu et al., 2023[12])

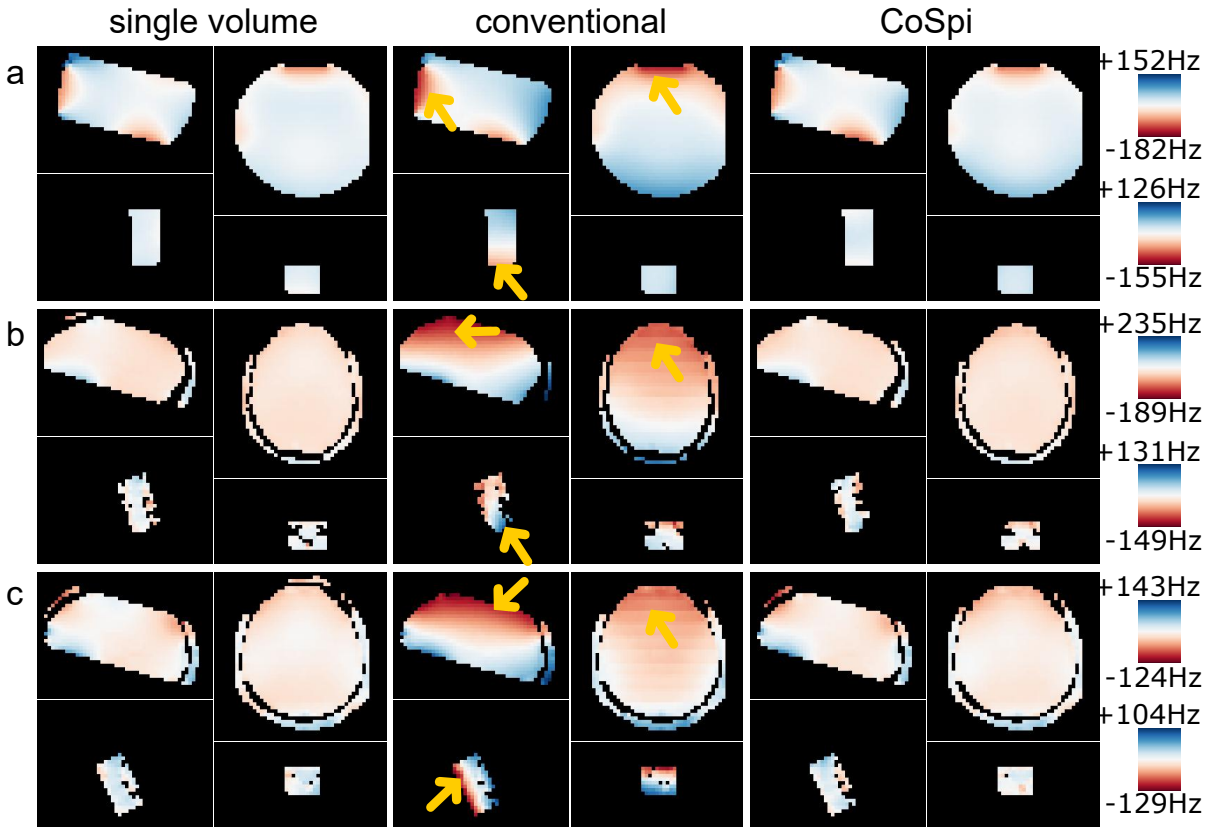

Figure **3-7**: Sagittal and transversal views of the B_0 field map of the masked brain and spinal cord adjustment volumes from "single volume", "conventional" and "CoSpi" region-wise adjustment volumes. They are for (a) a phantom setup, (b,c) volunteers B, and E. The arrows show the location with enhanced field inhomogeneities. The values shown in Hz are the maximal and minimal frequencies of the field maps from the same row. (Figure from Chu et al., 2023[12])

Table **3-1** shows that the conventional approach has a larger standard deviation (56Hz for the brain, 78.6Hz for the spinal cord) across the adjustment volumes than the CoSpi approach (19Hz for the brain, 20.4Hz for the spinal cord) in all volunteers. A higher standard deviation means that the variation of the values in the volume is higher. This table also shows that the linewidth (LW) of the field maps is better for the CoSpi approach. For the brain volume, the CoSpi shim approach is even better than the single volume shim (-6% in standard deviation and -22% in linewidth). The reason could be that an even higher harmonic of the shim is needed; both the single-volume and CoSpi shim method is limited to up to the second order shim; however, for the CoSpi shim, a precise brain and spinal cord mask is created, and the tune-up field map has a better resolution than the one that the single-volume shim approach used. For the spinal cord volume, the CoSpi shim approach has comparable performance to the single-volume approach (+1% in standard deviation and +5% in linewidth).
Therefore, from the quality and quantity value of the field maps, we can summarize that the overall field homogeneity is significantly improved for the CoSpi approach compared to the conventional region-wise shim approach.

3.4.3 Quality Comparison of EPI Acquisition of CoSpi and Conventional Shim Approach

The zoomed image of figure **3-8** shows that some slices are more distorted with the conventional shim setting. For the brain slice, the yellow contour overlapped on the brain part with the conventional shim setting. This means the EPI image is stretched. Similar distortions are also shown in the other slices, in which no contours are marked. The upper slices also show signal dropout (in the middle of the cross-sections) with a conventional shim setting. The spinal cord is also stretched for the spinal cord slice, and there is more signal dropout (enhanced in slice 1, 3, 6, and 8) on the image with a conventional shim setting.

3.4.4 Distortion

The results are shown in figure **3-9**. In figure **3-9**a, we can see that the voxel displacement map with the conventional shim setting has more variation than the one with CoSpi, which means that the distortion on the EPI acquisition with the CoSpi shim approach is less. We can also see it with the data of all five volunteers quantified in plot **3-9**c. This plot shows that the standard deviation of the voxel displacement for the slices in the middle of the brain with the CoSpi method has smaller values, which means the distortion is small. For the outer slices, the values of CoSpi shim is also slightly better. Therefore, the CoSpi approach has better performance regarding the reduction of distortion.
The results are even more pronounced for the spinal cord region, as shown in figure **3-9**b. The voxel displacement map from the conventional shim has a significant variation. Hence, more distortion is contained. From the plot in figure **3-9**d, we can also see that the CoSpi

Table **3-1**: Standard deviation in the masked area of the measured field map (upper row) and measured linewidth (LW, lower row) of the brain and spinal cord adjustment volumes for the different shim settings for the individual volunteers and their average value ("Mean"). The absolute values have the unit Hz. The relative changes compared to the single volume method ("gold standard") are written in parentheses.

		Volunteer					
	Shim Settings	A	B	C	D	E	Mean
Brain	Single Volume Brain	19.9 57.1	17.9 46.3	22.3 57.1	26.5 61.8	18.3 37.2	21.0 51.9
	Conventional	55.2 (+178%) 189.4 (+232%)	69.9 (+291%) 257.2 (+456%)	61.2 (+174%) 202.9 (+255%)	46.4 (+76%) 199.0 (+222%)	47.4 (+159%) 180.8 (+386%)	56.0 (+167%) 205.9 (+297%)
	CoSpi	19.0 (–4%) 31.6 (–45%)	16.8 (–5%) 39.4 (–15%)	20.1 (–10%) 54.2 (–5%)	24.1 (–9%) 43.0 (–30%)	18.1 (–1%) 33.0 (–11%)	19.6 (–6%) 40.3 (–22%)
spinal cord	Single Volume Spinal Cord	24.3 88.0	20.5 78.4	21.5 97.5	16.5 74.5	18.5 87.9	20.3 85.3
	Conventional	122.6 (+404%) 116.5 (32%)	75.5 (+269%) 130.4 (66%)	68.4 (+218%) 360.2 (269%)	66.7 (+305%) 205.4 (176%)	60.0 (+224%) 319.6 (264%)	78.6 (+288%) 226.4 (165%)
	CoSpi	15.0 (–38%) 82.9 (–6%)	28.7 (+40%) 117.7 (+50%)	18.8 (–13%) 90.1 (–8%)	20.6 (+25%) 78.3 (+5%)	18.8 (+1%) 79.2 (–10%)	20.4 (+1%) 89.6 (+5%)

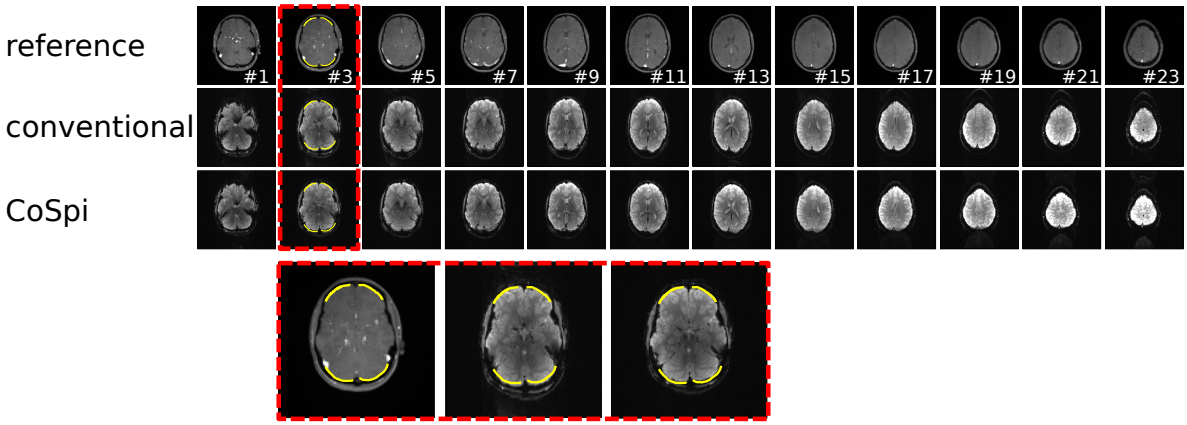

(a) Brain volume, every second slice is shown.

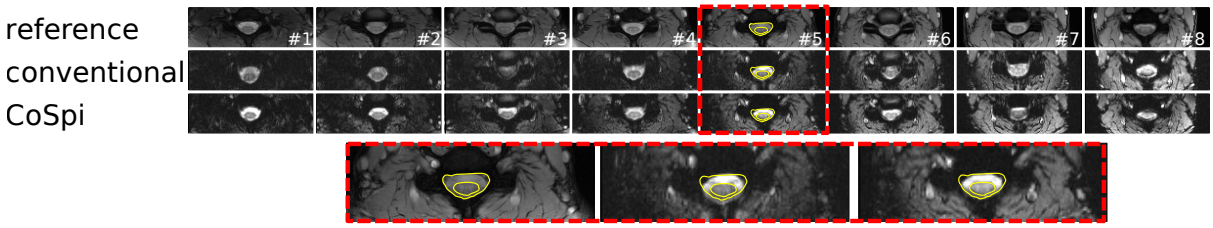

(b) All spinal cord slices.

Figure **3-8**: Comparing anatomical reference image with EPI acquisitions with conventional and CoSpi shim settings. For one slice of each volume, the anatomic contour, derived from the reference measurement is marked in yellow on the EPIs. And this slice is also zoomed (within the red block). The images are from volunteer B.

shim approach performs better than the conventional shim approach in all slices. The blue contour from the anatomic reference image on the sagittal EPI images also shows that the distortion is enhanced from the conventional shim method.
Table **3-2** shows the standard deviation of the voxel displacements for each individual volunteer. The values indicate that voxel displacements are reduced with the CoSpi shim settings in each volunteer for brain and spinal cord volume, with an average reduction of 34% in the brain and 71% in the spinal cord volume. It is important to mention that these absolute values in the table **3-2** show the overall performance of the shim approaches and provide a comparison of these two shim approaches and do not represent the degree of in-plane geometric distortions directly.

Table **3-2**: Comparison of Standard deviation of the voxel displacements (in mm) in brain and spinal cord volume for all five volunteers from conventional and CoSpi shim settings.

		Volunteer					
		A	B	C	D	E	Mean
brain	conventional	0.58	1.79	0.72	0.85	0.84	0.96
	CoSpi	0.52	0.54	0.59	0.71	0.78	0.63
spinal cord	conventional	0.27	0.38	0.97	0.58	0.76	0.59
	CoSpi	0.14	0.26	0.14	0.21	0.10	0.17

3.4.5 Temporal SNR

A better shim along the slice direction can reduce the through-slice dephasing problem and result in a better signal. Therefore, we also compare the temporal signal-to-noise ratio of the CoSpi and Conventional shim approach.
Figure **3-10**a shows that on some slices, the signal-to-noise ratio is extremely small in the middle (#1 and #18) and at the front (#1) of the brain (shown with green arrows) with the conventional shim setting. Also, for the higher location (sagittal image) of the brain, the image with a conventional shim setting has a significant signal dropout, while the CoSpi has, in general, a higher level of SNRs, as shown in the sagittal images. For the spinal cord volume (c.f. **3-10**b), the CoSpi shim setting provides a better temporal SNR in the sagittal image and slice 3. However, for slice 7, the conventional shim setting provides a better SNR. We can also see from the sagittal SNR maps that there is one slice (pointed at with a green arrow) that has a higher value with the conventional shim approach than the CoSpi shim approach. But in total, we can see the sagittal SNR map of EPI acquisitions with the conventional shim setting has more signal dropouts (pointed out by the green arrows).

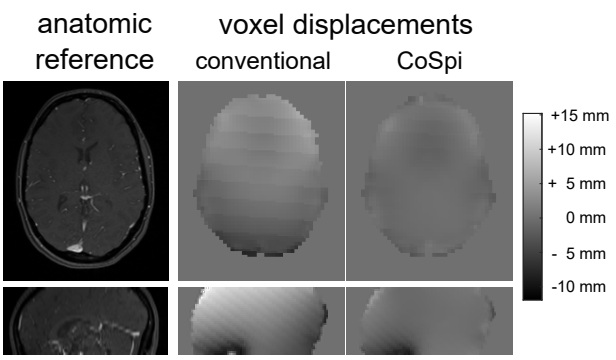

(a) Anatomic reference with the sagittal and transversal view for the brain volume and its voxel displacement maps within the masked brain volume. The color bar shows that the range of the voxel displacement is between -10mm and +15mm.

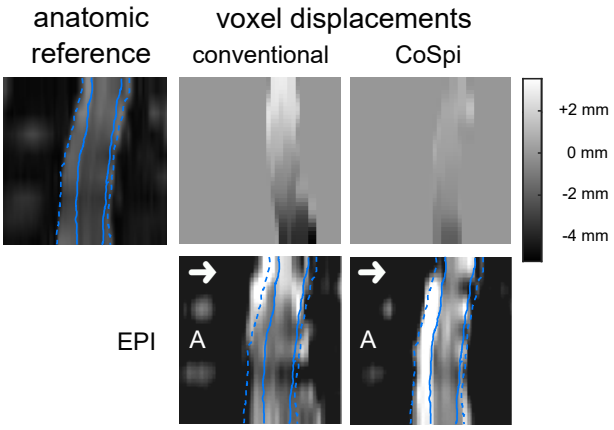

(b) Anatomic reference with the sagittal view for spinal cord volume, its EPI, and its voxel displacement map. The letter A on the EPI image means the anterior direction. The arrows indicate the phase encoding direction. The blue contour shows the position of the spinal cord in the anatomic image. The dashed blue contour shows the position of the CSF.

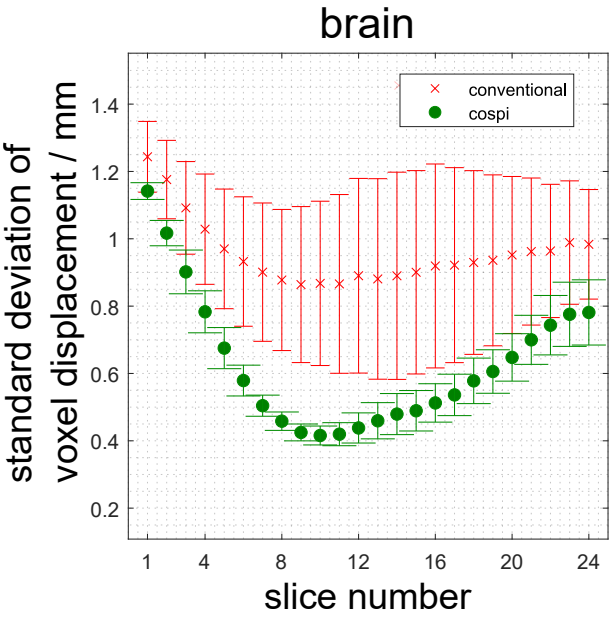

(c) The standard deviation of voxel displacement in every single slice in the brain volume averaged from five volunteers.

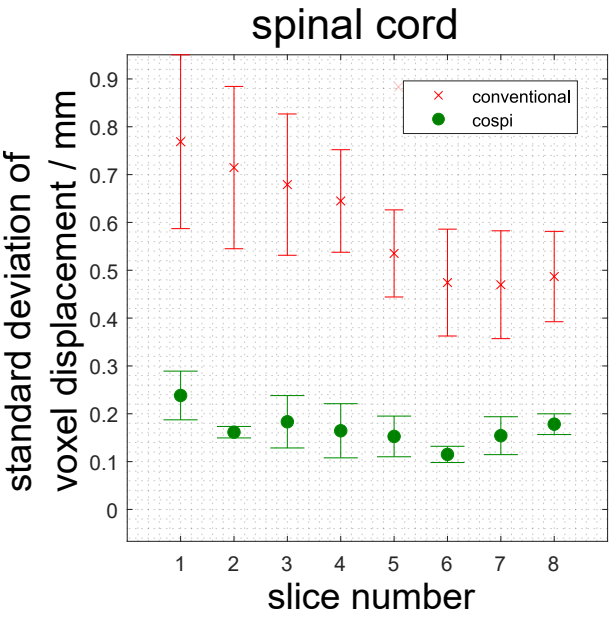

(d) The standard deviation of voxel displacement in every single slice in the spinal cord volume averaged from five volunteers.

Figure **3-9**: Comparison of voxel displacements map for the brain and spinal cord volume from in vivo experiment. The error bars are the standard deviation over the data of the five volunteers. (Figure from Chu et al., 2023[12])

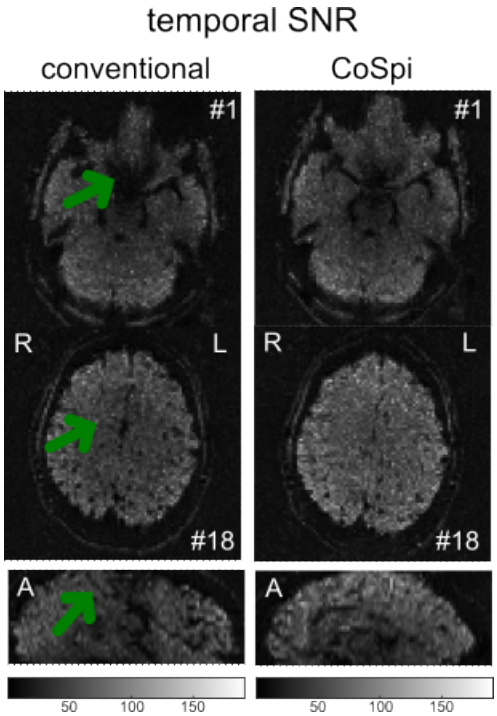

(a) Temporal SNR maps of the brain volume of EPI acquisitions with CoSpi and conventional shim approach. The green arrows show the low tSNR areas.

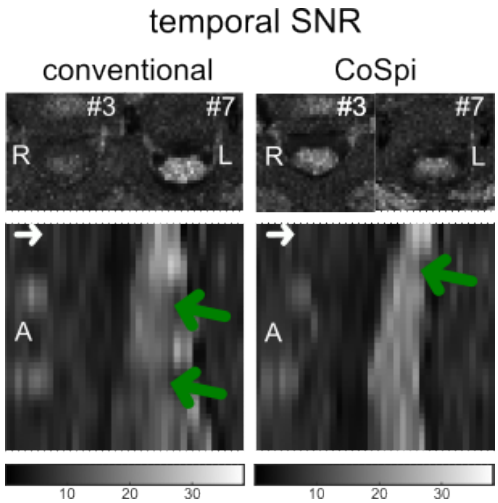

(b) Temporal SNR maps of the spinal cord volume of EPI acquisitions with CoSpi and conventional shim approach. The green arrows show the low tSNR areas.

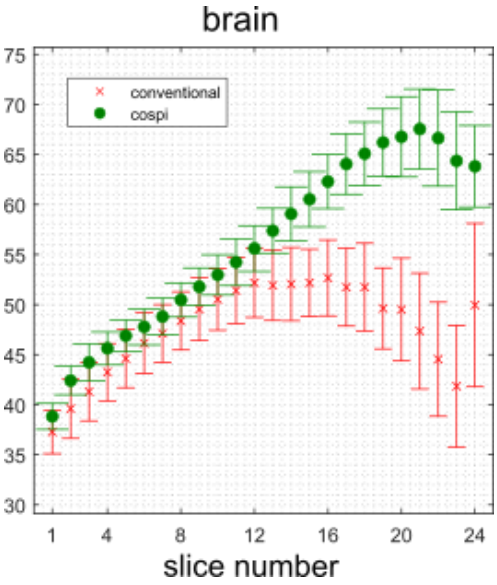

(c) Slice-wise tSNR plot in brain slices for images acquired from CoSpi and conventional shim approach.

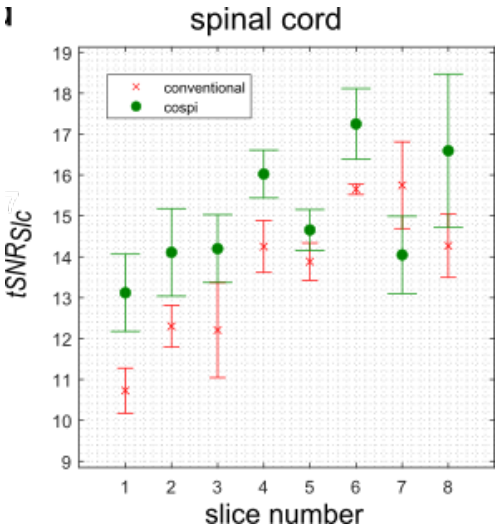

(d) Slice-wise tSNR plot in spinal cord slices for images acquired from CoSpi and conventional shim approach.

Figure **3-10**: Comparison of the Temporal SNR map for the brain and spinal cord volume. (Figure from Chu et al., 2023[12])

The plot in figure **3-10**c shows that the SNRs in lower slices of the brain region for the CoSpi shim setting only perform minorly better than the conventional shim setting, while the upper slices indicate an advantage for the CoSpi shim settings with a gain of SNR for up to 50%. And figure **3-10**d shows that not all slices with the CoSpi shim method have better values in terms of SNR. However, seven of eight slices still have a tSNR increase with the CoSpi shim setting. The gain is between 5% and 20%.
Values of $tSNR_{Vol}$ for all five volunteers, ten volumes separately, are presented in table **3-3**. The EPI acquisitions obtained with the CoSpi shim approach have a higher tSNR for all the volumes than the conventional shim approach, except for the brain volume of volunteer E. In particular, all spinal cord volumes show increased temporal SNR values for the CoSpi shim settings with an improvement of up to 20%. For all volunteers, all volumes, the average improvement is 8%.

Table **3-3**: tSNRs of the respective volumes

		Volunteer					
		A	B	C	D	E	Mean
brain	conventional	42.4	52.5	49.5	37.1	57.4	47.8
	CoSpi	51.0	59.3	64.4	52.8	52.4	56.0
spinal cord	conventional	12.7	14.6	13.3	14.2	13.0	13.6
	CoSpi	13.2	17.4	13.5	14.7	15.7	14.9

3.5 Summary and Conclusion

In this chapter, the performance of the CoSpi shim approach was compared with the conventional and single-volume shim approaches.
The results show that the CoSpi shim approach performs much better regarding field homogeneity than the conventional approach. The field homogeneity in vivo is even better than the single-volume shim approach. The results also show that typical problems like geometric distortions and signal losses are improved with the CoSpi shim approach. Therefore, the CoSpi shim approach improves the image quality of the combined brain and spinal cord fMRI, making this method more usable for patient scans. Additionally, with this dedicated algorithm, the measurement is faster and more user-friendly.
Nevertheless, there is still some interest in further improving the field homogeneities in the brain and spinal cord volume.
On top of the dedicated CoSpi algorithm, either z-shim [18] or automated z-shim (refer to chapter 4) can be used in the spinal cord volume, therefore, no z-shim was considered for the comparison of conventional region wise shim approach and CoSpi algorithms.

This dedicated CoSpi algorithm can be easily extended to more than two target volumes. An additional target volume can be helpful if, e.g., more brain stem coverage is desired.
A slice-specific shim setting [26] was not considered here. One reason was that the acceleration for the brain volume with sms (refer to section: 2.3.2), as we did in chapter 5, requires the shim settings to be compatible with all slices being excited simultaneously. It will not be easy to find a slice-specific shim compromise between these simultaneously excited slices. But slice-specific frequency settings can easily be determined with the CoSpi algorithm if present. It has not been used in this chapter because the application of slice-specific frequency settings is time-consuming for the conventional region-wise approach. For each slice, a manual determination of the adjustment volume is required, and an experimental frequency adjustment from the vendor is needed. Therefore, we cannot ensure a fair comparison between them.
Dedicated shim hardware (e.g., refer to [24]) also seems feasible to be used, which could provide a dynamic update of second- and up to fifth-order shim for further improvement. However, this will require a hardware installation.

4 Automated z-Shim Calculation

The interest in spinal cord fMRI is increasing. However, there are fewer fMRI studies because a cumbersome and user-dependent z-shim [18] method is needed. This increases the difficulties of spinal cord fMRI. This chapter introduces an automated calculation of optimum z-shim gradient pulses to overcome this problem.

4.1 Through Slice Dephasing

EPI is normally used sequence for spinal cord fMRI imaging which suffers from a through-slice dephasing effect within the spinal cord slice. The reason is that the vertebrae and intervertebral discs have different magnetic susceptibilities which result in a periodical varied magnetic field inhomogeneities [13]. Therefore, the inhomogeneities cannot be compensated with the standard shimming due to the limitation of the first and second-order magnetic strength terms. The slice resolution for EPI spinal cord scan usually is relatively low. e.g., 5mm. Different compensation moments of shimming in the z-direction could be needed for different slices. Figure **4-1** shows an illustration for this problem. This figure shows different magnetic fields in the longitudinal direction due to field inhomogeneity beside vertebrae and intervertebral disc through one slice, resulting in an unsynced spin rotation called a dephasing effect.

4.2 Slice-Specific z-shim Gradient Pulses

To solve the signal loss problem in the spinal cord, slice-specific z-shim gradient pulses for T2*-weighted spinal cord imaging were performed in previous studies[18]. The z-shim method has a pre-dephasing gradient moment prior to data acquisition. This pre-dephasing gradient is chosen, as shown in figure **4-2** with the red trapezoid, so that the signal at the center echo reaches its maximum signal intensity, reducing the signal loss. From the observation of spins follows, that the field inhomogeneities have a dephasing effect; therefore, the echoes have reduced intensity. A pre-dephasing gradient causes an extra dephasing in the opposite direction of the dephasing effect due to the field inhomogeneities. As a result, the dephasing effect from the field inhomogeneities is partly compensated by the pre-dephasing gradient moment.

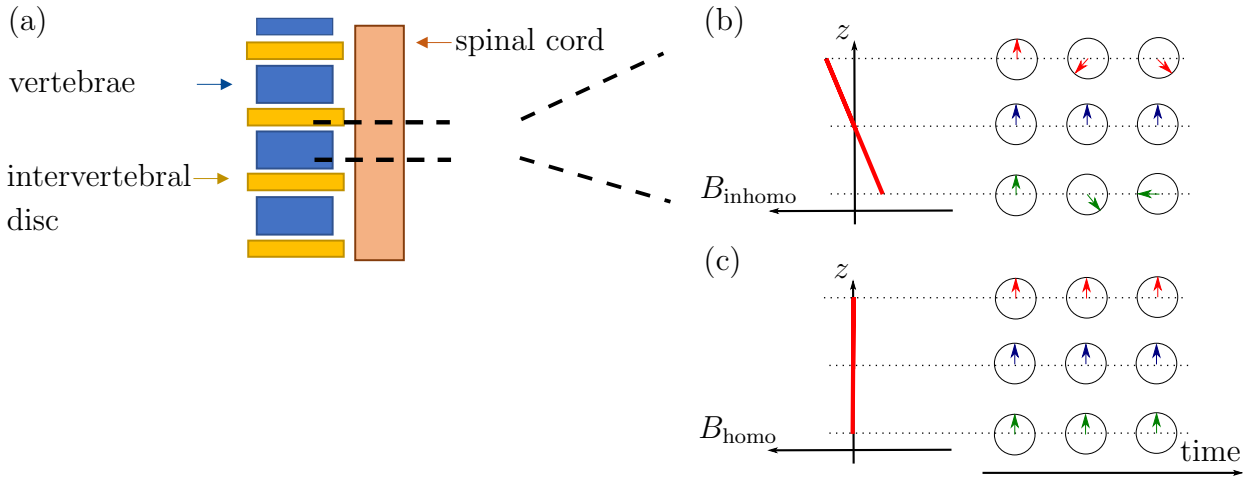

Figure **4-1**: (a) An illustration of a part of the spinal cord, vertebrae, and intervertebral disc with a symbolic linear field inhomogeneity within one slice. In this example, the upper row of spins of one slice has a positive extra magnetic field, and the lowest row has a negative extra magnetic field. (b) The change of phase of spins, induced by the linear field inhomogeneity, is different in the different positions within one slice, which results in a smaller sum of phases within one voxel. (c) In an ideal case of field homogeneity within one slice, the magnetic field in the longitudinal direction is perfectly homogenous, which does not induce phase differences within one slice.

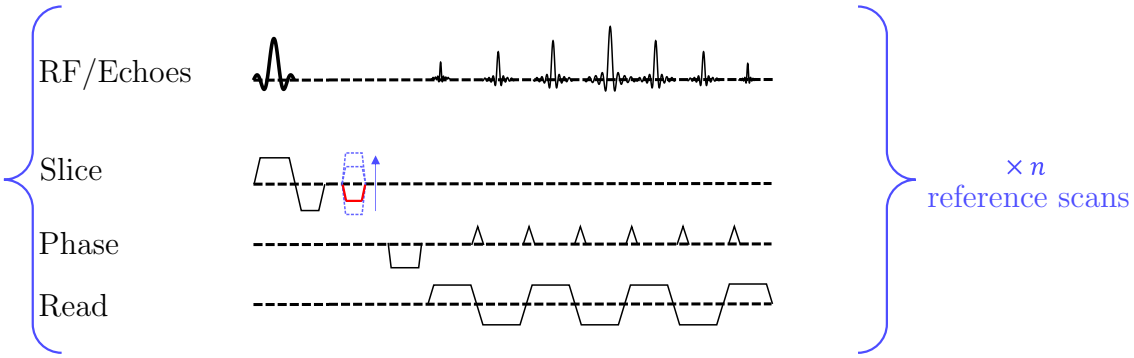

Figure **4-2**: EPI z-shim reference sequence with different z-shim reference gradient moments (blue trapezoid). Without all different reference gradient moments and $\times n$ scans, the sequence graph represents an EPI sequence with a single, slice-specific z-shim gradient pulses (red trapezoid). n are the reference measurement steps.

In practice, the pre-dephasing gradient are not perfect. The reason is the nonlinearity of the field inhomogeneities through a slice.

If we assume that the gradient field due to the field inhomogeneity is $-I_{\text{inhomo}}[\mu T/m]$, a gradient $G_{\text{pre-dephasing}}$ should be introduced. We can write the pre-dephasing gradient amplitude, which is:

$$G_{\text{pre-dephasing}} = \frac{I_{\text{inhomo}} \cdot TE}{t_{\text{pre-dephasing}}} \tag{4-1}$$

where $t_{\text{pre-dephasing}}$ is the duration of the pre-dephasing gradient. However, we cannot know the I_{inhomo}. Therefore, during the reference measurements, different I_{inhomo}, accordingly $G_{\text{pre-dephasing}}$ are tried. A series of equidistant $G_{\text{pre-dephasing}}$ around 0 are measured, which are the reference measurements.

The field inhomogeneity I_{inhomo} for z-shim is not calculated from a field map because the EPI acquisition faced a strong problem with distortion due to field inhomogeneity which could lead to a mislocalization between EPIs and Field map.

To show the necessity of the z-shim for the spinal cord, we can see figure **4-3**, which shows that in the cervical spinal cord, without z-shim, an obvious signal loss is seen in some slices but not in all slices, which shows a slice-wise z-shim can be useful. With the z-shim, slices with signal loss improved, and the slices without signal loss kept their good image quality.

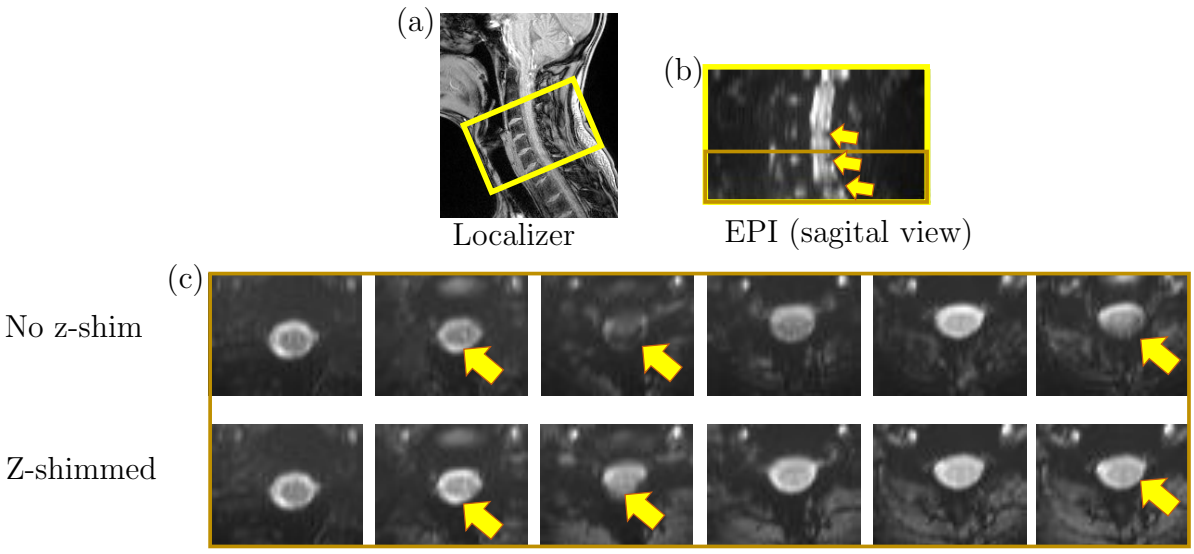

Figure **4-3**: (a) Localizer image to define FOV. The area within the yellow block shows the EPI measurement stack. (b) Spinal cord EPI acquisition in sagittal view. (c) Some slices of transversal EPI images were compared without and with z-shim. The arrows show the signal loss at the EPI images of the measurement with z-shim, which shows that the EPI images have better signal in the z-shimmed images.

4.3 Method

This section introduces two methods to determine the optimal z-shim gradient moments. One method is user-based z-shim which has been used in several previous studies[40][14], which is manual and user-dependent. Another method is automated z-shim written in the self-written program in IDL (Interactive Data Language from version 8.8.0, L3Harris Geospatial, Broomfield, CO, USA). The measurement parameters and analysis methods to compare user-based and automated z-shim are also shown in this session.

4.3.1 Workflow of User-Based z-shim

A graphic workflow is shown in figure **4-4** within the blue dotted block. EPI reference scans were performed with 21 different z-shim gradient moments $G_{\text{pre-dephasing}}$ between $-0.2mT/m$ and $+0.2mT/m$ for each slice. The used z-shim gradient moments were equidistant. A user must check all images of the z-shim reference acquisition to identify the best signal intensity in the spinal cord area for each slice. The z-shim value represents the value desired for the fMRI acquisition and then needs to be entered as indices into the user interface of the pulse sequence.

4.3.2 Algorithm of Automated z-shim

A graphic workflow is shown in figure **4-4** within the yellow dotted block.
First, the maximum intensity projection (MIP) from all z-shim reference images was calculated to obtain images for each slice with a higher signal amplitude in all spinal cord voxels.
A rough spinal cord and cerebrospinal fluid (CSF) intensity area was identified by dynamic threshold from an intensity histogram of the central region of the MIP image, as the spinal cord is positioned in the center of the image within one slice. The spinal cord and CSF region have higher signals than surrounding tissues, so no higher threshold was needed.
The bin differences are shown as a red curve in figure **4-4**. If the sum of six consecutive differences of bins was below a certain threshold (1200; empirical value), this position is defined as the lower threshold. We set the lower threshold because, on the histogram of maximum intensity projection, the bins of surrounding tissues have bigger differences because there are more voxels in each individual low-intensity bin.
After the lower intensity threshold is set, the voxels below this threshold are discarded. This step discards most of the voxels that are not of interest, leaving a large and connected area close to the center of the slice that contains the spinal cord and surrounding CSF. The following steps could discard other non-region-of-interest voxels.
Next, a region-grow algorithm was used to discard voxels isolated from the spinal cord and CSF regions. The seed voxel of the region-grow algorithm was determined from the center of a circle with a diameter of $10mm$ for which the sum intensity was a maximum from all

investigated circles because that means most spinal cord and CSF voxels are located within the circle. And the center of the circle should be located in the center of the spinal cord region. If the seed voxel is in the CSF region, the intensity of the whole $10mm$ diameter circle shouldn't be the maximum of all circles considered because the CSF is rather thin.
Next, the intensities were scaled around the mean value of certain slices to maximize the contrast within slices. To separate CSF from spinal cord voxels, edge detection was applied with another region grow step to obtain the final spinal cord mask.
To obtain the optimum z-shim value, the signal amplitude of each voxel as a function of the z-shim value of the reference acquisition was fitted with a sinc function because a sinc function, Fourier transform of a rectangular slice profile, is the theoretical signal curve of linear field inhomogeneity. As you can see from the orange curve in the plot in figure **4-4**, only the upper half is fitted because the reference measurement with a low signal contains a high percentage of noise, which can lead to a wrong fit.
The position of the fit's maximum was taken as the optimum z-shim value for this single voxel. (The position of the maximum is shown as the point of intersection of dotted lines in the plot in figure **4-4**.) The average of all z-shim values within the masked spinal cord slice is the z-shim value for this specific slice. The value is rounded to the units used by the pulse sequence. Voxels with non-valid results were discarded. Compared to picking the z-shim value with the highest signal intensities, this fit approach can be expected to be more robust to the physiological signal fluctuations. The observed curves normally do not match a perfect sinc and often do not show nulls. Hence, only the upper half of the sinc curve was fitted. The values for all slices will be written as indices to a file that is read by the pulse sequence.

4.3.3 Parameters

For the phantom experiment in Figure **4-5**, a phantom consisting of two $0.5l$ milk cartons (Hamfelder Hof Milch, Hamfelder Hof Bauernmeierei GmbH & Co. KG, Mühlenrad, Germany) with a gap of $1.6cm$ in-between was investigated. The localizer of the phantom experiment is shown in figure **4-5**a.
Healthy volunteers were also investigated for the in vivo experiment. The localizer of the in vivo experiment is shown in Figure **4-3**(a). For both phantom and in vivo Experiments, EPI acquisitions covering 16 slices of the spinal cord only were performed. In the section 2.5 described acceleration method is used. However, unlike the standard spinal cord parameter, a square FOV of 132mm, an in-plane resolution of $1.2\times$ 1.2 mm^2 is used. The images were acquired with a TE of 24ms and a TR of 2000ms and the isocenter in the middle of the slice stack. The z-shim reference acquisition covered 21 equidistant steps compensating field gradient between $\pm$ 0.2mT/m for each slice. Both user-based and automated z-shim were used and evaluated. Averaged images and SNR maps were calculated with twenty acquisitions.

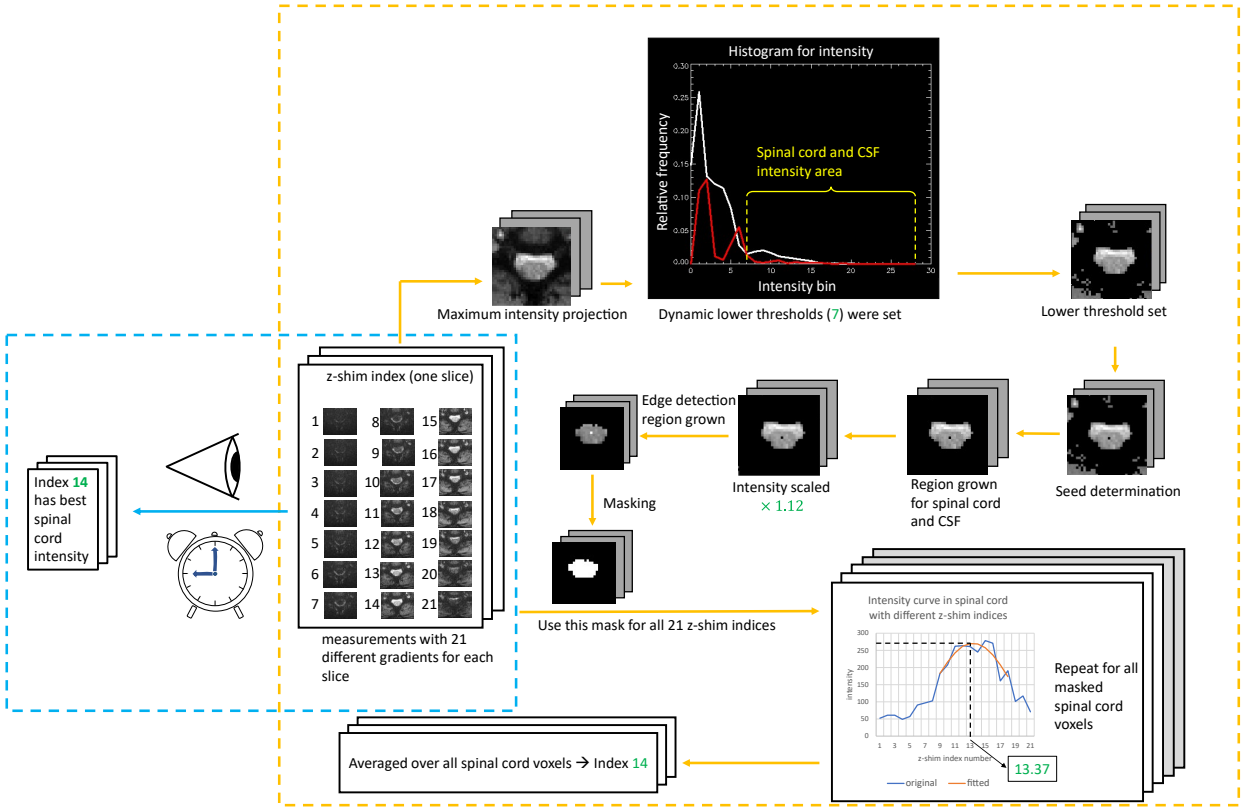

Figure **4-4**: Workflow of user-based (in the blue block with blue arrow) and automated z-shim (in the yellow block with yellow arrows). The detailed description is written in sections 4.3.1 and 4.3.2

4.4 Results

4.4.1 Phantom

This result (see **4-5**c) shows that the slice near the gap needs a more extensive z-shim correction than the slices far away from the gap, which makes sense because the created field inhomogeneity is due to the susceptibility difference between milk ($\geq$87% water) and air. Figure **4-5**b shows without z-shim, the slices near the gap have a great signal loss. Both user-based and automated z-shim approaches yield similar results regarding z-shim values (see **4-5**c) and signal intensity and image quality for the corresponding optimum values, which shows a basic performance of the automated z-shim method. Other than the method described in section 4.3.2, no segmentation of the spinal cord is needed.

4.4.2 In vivo

In figure **4-6**, the arrows are pointing at the signal dropout area on the averaged images and SNR maps. From the no z-shim result column, some slices do not have enough intensity on the spinal cord, and its SNR map also shows low SNR in the spinal cord area, which means the signal could be the major problem on low SNR. As we can see, both user-based and automated z-shim methods have improved on the spinal cord slice with a non-11 index according to the signal intensity from averaged image and SNR value according to the SNR map.

4.4.3 Similarity with User-based and Automated Z-shim

As described in section 4.3.2, the automated z-shim needs to segment the spinal cord area and fit half sinc to find the optimum value for the z-shim gradient pulse. Especially in the segmentation part, we used an empirical threshold to discard low signal voxels. Before, this method was widely used for future fMRI studies from the institute, some data were acquired and evaluated with user-based and automated methods to test the algorithm's stability.

Parameters

To check the stability of the automated method, nine healthy volunteers were investigated after their informed consent was obtained. In this Experiment, only localizer and reference measurements were acquired. Different from the experiment before, as described in section 4.3.3, only 12 EPI slices were acquired because for the current combined brain and spinal cord fMRI study design, only 12 spinal cord slices were desired. Other parameters are identical as described in the section 4.3.3.

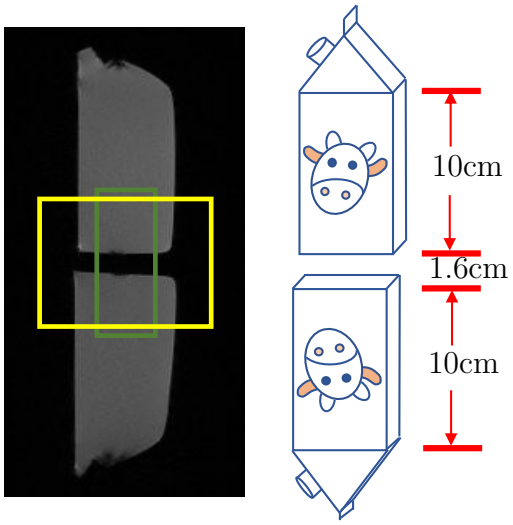

(a) Phantom localizer. Two milk cartons with a gap of 1.6cm were scanned. The yellow block shows the localizer. The green block shows the standard shim area from the vendor.

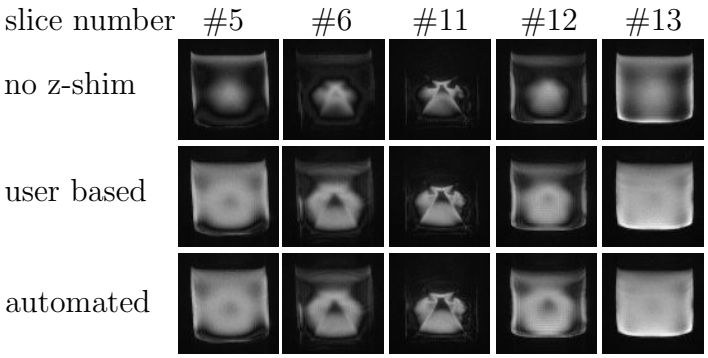

(b) Phantom results for slices 5, 6, 11, 12, and 13. Some slices (slices 7, 8, 9, 10) in the middle of the acquisition stacks, which has rare signal because of the designed gap, are not shown.

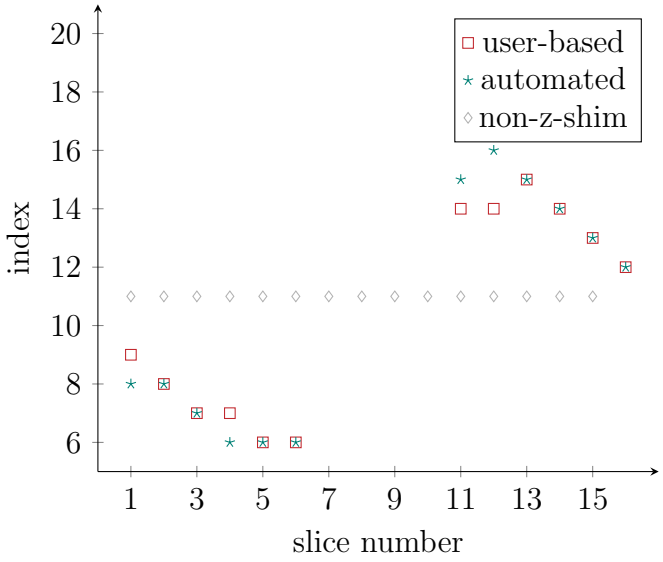

(c) Phantom results. The chosen indices are from the user-based and automated method for all slices.

Figure **4-5**: Results of the milk carton phantom.

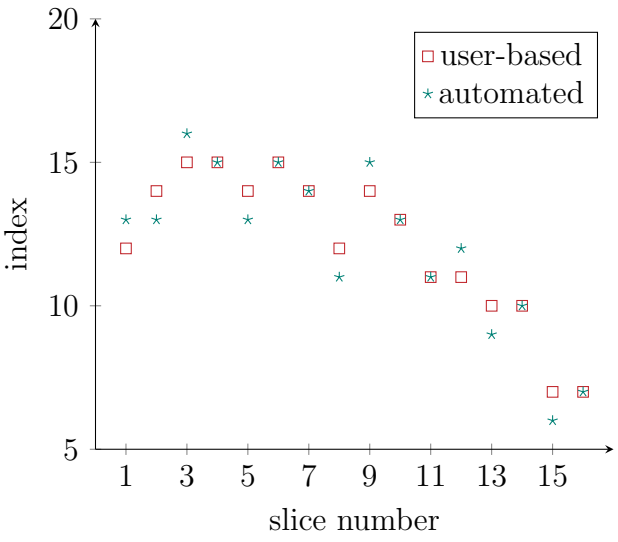

(a) Chosen indices of volunteer 1

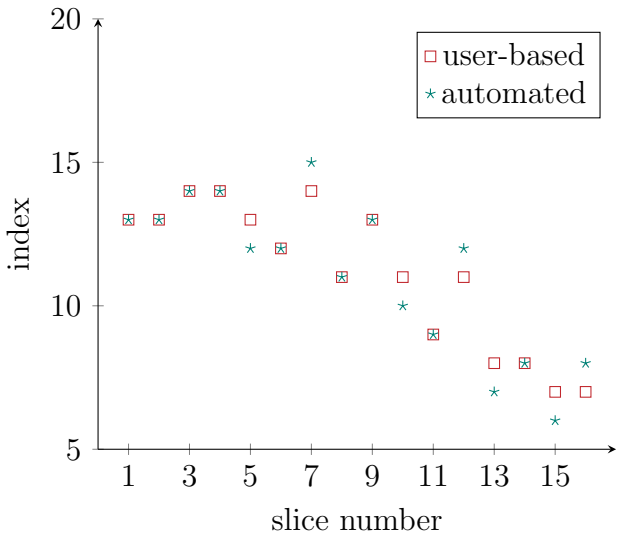

(b) Chosen indices of volunteer 2

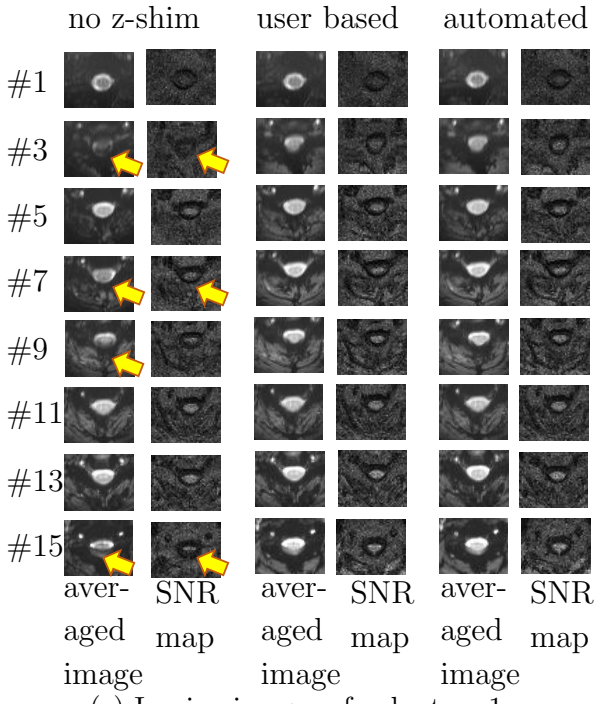

(c) In vivo images of volunteer 1

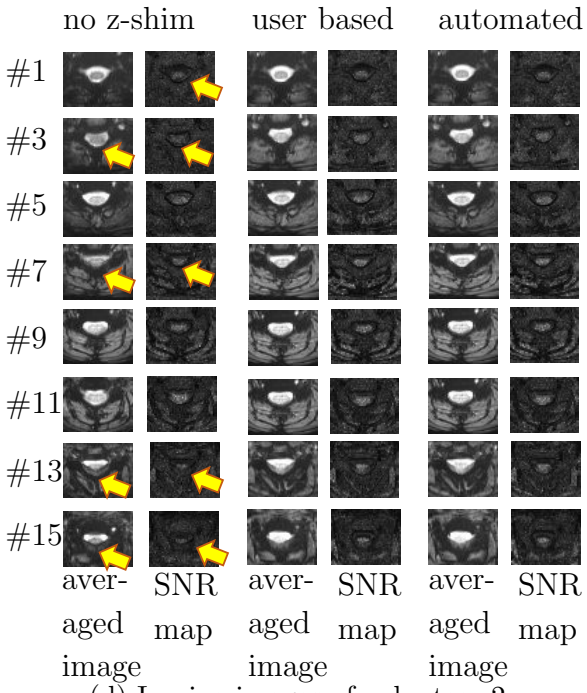

(d) In vivo images of volunteer 2

Figure **4-6**: Results from two in vivo experiments. (a, b) Chosen indices for different slices from user-based and automated methods. (c, d) Averaged image and temporal SNR maps of 20 successive EPI measurements for 8 of 16 slices from two volunteers. The signal dropouts were seen in several slices, pointed with yellow arrows, for measurements without z-shim. Measurement with the z-shim approach, both user-based and automated methods, could compensate for the signal dropout problem.

Results

Figure **4-7** shows that the z-shim value yields similar results for nine volunteers between the user-based and automated z-shim approaches. The average difference between the user-based and automated z-shim approaches is 0.69, which shows the stability of the automated shim method.

4.5 Summary and Conclusion

A z-shim improves the signal intensity problem in a T2* weighted image for the spinal cord through the correction of the center echo. However, the conventional user-based method is time-consuming and user-dependent. This chapter introduced an automated z-shim, which provides a similar result to the conventional user-based method but is less time-consuming and not user-dependent.

One drawback of this method is that the volume coverage is still small. Currently, a maximum of 16 slices with a slice thickness of 5mm are tested. The reason is that the current combined brain and spinal cord fMRI study design from our institute only requires a volume coverage of 60mm in the slice-selective direction. For a bigger volume, especially at the thoracic spinal cord, the image quality gets worse, and the segmentation of the spinal cord area will be more difficult.

Nevertheless, there is also another study regarding the automated z-shim approaches [28], which provides and analyzes two automated z-shim approaches. Similar to the approach provided by this chapter, one approach also uses a series of EPI reference scans to find the z-shim value with the maximum spinal cord signal. The other approach calculates each EPI slice's required compensation gradient moment from field map data. They found out that from the image quality level, the approach based on the field map performed slightly worse than the manual approach, while the approach based on the EPI reference scan performed as well as the manual approach. In comparison to the automated z-shim from this chapter, this method uses a well-tested segmentation from the spinal cord toolbox [22]. However, the data must be transferred to an additional online calculation computer to achieve this approach, which was difficult for the data infrastructure of the MR system of the institute. Another difference is that this study uses the index of the maximum of the signal as z-shim indices, and no sinc fit was considered. However, due to an acute movement during the acquisition of the reference scans, a single scan is less reliable.

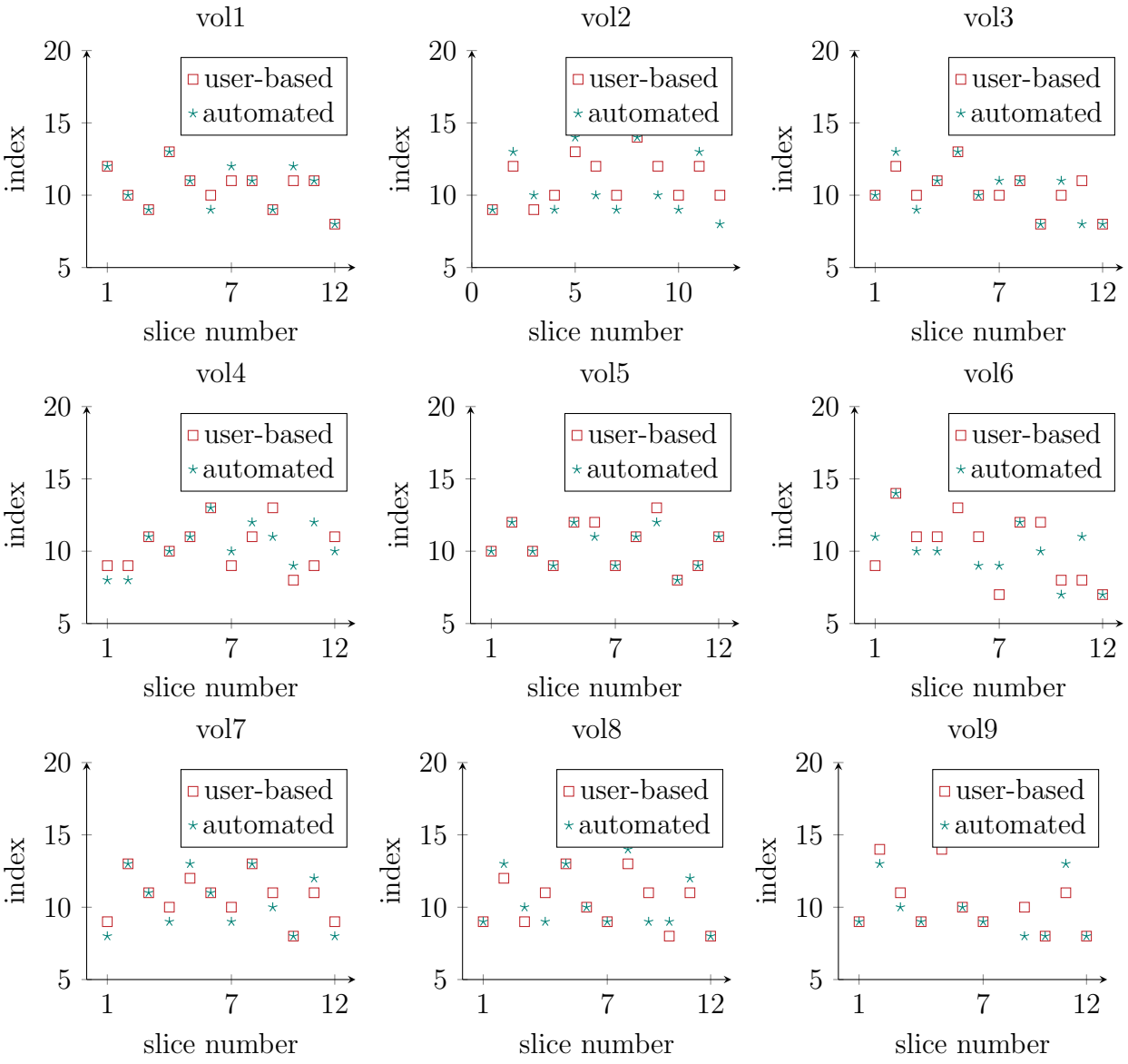

Figure **4-7**: z-shim indices from user-based and automated z-shim method

5 Partial Simultaneous Multi-Slice Acquisitions

In the previous chapters, the image quality for combined fMRI of the brain and cervical spinal cord through region-wise dynamic shimming and slice-specific z-shim in the spinal cord was optimized. However, to avoid excessive repetition times/TRs, the volume coverage is limited[40]. Better volume coverage/shorter TR could be achieved with simultaneous multi-slice (SMS), which is well established in the brain; however, the vendor's SMS implementation is not compatible with two slice groups as used for combined brain and spinal cord fMRI, furthermore, SMS is not feasible in the spinal cord due to the limited coil arrangement around the neck area.

This is why a "partial" SMS acceleration has been implemented that applies SMS to the brain but not to the spinal cord, which requires not only pulse sequence modifications but also adaptations in the reconstruction pipeline.

5.1 Background

The simultaneous multi-slice (SMS) technique [37] (refer to 2.3.2) is usually used to acquire large-volume fMRI because it accelerates the data acquisition directly. SMS should not be used in the cervical spinal cord. The reason is that SMS excites and acquires multiple slices simultaneously and separates their signals based on their relative signal amplitudes in different coils. The solution of the equation system is poorly conditioned because the coil sensitivities are too similar due to the small distance between the coils. Therefore, as shown in figure **5-1**, the image quality of the phantom with SMS has more ghosting artifacts than without SMS.

An overall SMS in brain and spinal cord volume could not be used because of the different orientations and resolutions of the two volumes.

However, a partial simultaneous multi-slice acquisition improves the temporal resolution for the brain and spinal cord fMRI without losing image quality. A partial simultaneous multi-slice acquisition means that only one volume, in this case, the brain volume, uses the SMS, but the spinal cord volume does not use the SMS technique.

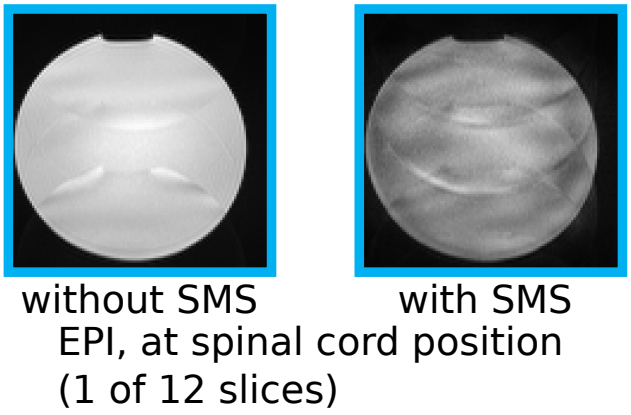

Figure **5-1**: Single volume spinal cord EPI without SMS and with SMS of factor 3 for a typical spinal cord position, for combined fMRI.

5.2 Method

To realize an image reconstruction pipeline using the SMS function in the brain volume but without the use of the SMS function in the spinal cord, the reconstruction pipeline needs to be modified. Therefore the image reconstruction results need to be examined.

5.2.1 Reconstruction Modification

The reconstruction pipeline from the vendor is built as a chain of functors with different functions. Each functor performs a particular task in the image reconstruction, e.g., regridding, filtering, GRAPPA kernel calculation and application, Fourier transformation, magnitude extraction, channel combination, and image correction like correction of Maxwell terms and filling header information. It also connects the functors and transfers the raw and image data with the information of k space line, slice number, and orientation of the image data.
The standard functors themselves cannot be modified; however, own functors can be written, and a dedicated configuration program can be used to remove or replace std functors from the chain, add own or standard functors to the chain, and redefine to which functor output of a functor is passed to. The use of pipe services can define if and how data can be processed in parallel. At the end of a pipe service: all parallel processes are terminated so that the next pipe service can only be performed with fully processed data.
To achieve the goal of having only SMS in the brain volume, the brain data had to be processed using the original reconstruction pipeline. Additionally, the spinal cord data required pseudo SMS reference measurements, and the spinal cord data had to bypass the SMS functions.
To realize this function, first, the data need to be cloned. Then the cloned data will be defined as the reconstruction data for brain volume and the reconstruction for spinal cord volume with a newly added flag. The flag is dependent on the slice group number. Cloned

data are needed because modification of the data wasn't allowed. And the unnecessary data can be easily deleted with another self-written functor.

To bypass the SMS functionalities, branch functors have been written and added to the reconstruction pipeline. These branch functors can recognize the flag that is added after the cloning of the data. And the data can be led in the correct functors: SMS or non-SMS functors. In the non-SMS functors, the data will only go through the functors without being processed. Bypassed functors that we assigned simply by the name to SMS functionality are SliceGrappaFitLoop, SliceGrappaFit, SliceGrappaApply, and SliceGrappaApplyLoop. Another functor that needs to be bypassed empirically is the EPIPhaseCorrPE functor.

5.2.2 Setup and Parameter

It is important to check the image quality with the modified reconstruction pipeline compared to the reconstruction without a modification. Therefore, the single volume with SMS acquisition was compared to the combined volume with SMS acquisition.

For this study, 72 slices were acquired, 60 slices of the brain with an acceleration factor of 3, and 12 spinal cord slices. The brain volume has a square FOV of 220mm with an in-plane resolution of $2.0\times2.0\text{mm}^2$ and a slice thickness of 2mm without any gaps in between. The spinal cord volume has a square FOV of 136mm with an in-plane resolution of $1.2\times1.2\text{mm}^2$ and a slice thickness of 3.5mm without any gaps in between. For both volumes, GRAPPA with an acceleration factor of 2 and a 7/8 partial Fourier was used, which yields a minimal TE of 24ms for the brain and 27ms for the spinal cord volume. With these parameters, we have a minimum TR of 4177ms without SMS acceleration but a minimum TR of 1975ms with an SMS factor of 3 for the brain region. For the phantom experiment, the particular minimum TRs with a fixed flip angle of 75° were used. For the in vivo experiment, a fixed TR of 4177ms with a flip angle of 86° was used for all acquisitions to avoid the influences of the T1 values with different TRs on the tSNR. This flip angle is the Ernst angle $\alpha_E = arccos(e^{-TR/T1})$ for gray matter T1 (1470ms) at 3T system in literature[15]. Aside from combined measurements, acquisitions covering the brain volume only were performed with and without SMS and solely using the standard reconstruction of the vendor to evaluate whether the modification targeting the non-SMS slices had an impact on the reconstruction of the SMS slices.

5.3 Results and Discussion

To evaluate this partial SMS method, the tSNR maps for both phantom and in vivo examinations were calculated. For the tSNR maps in vivo, only gray matter is evaluated because the fMRI activation is on gray matter.

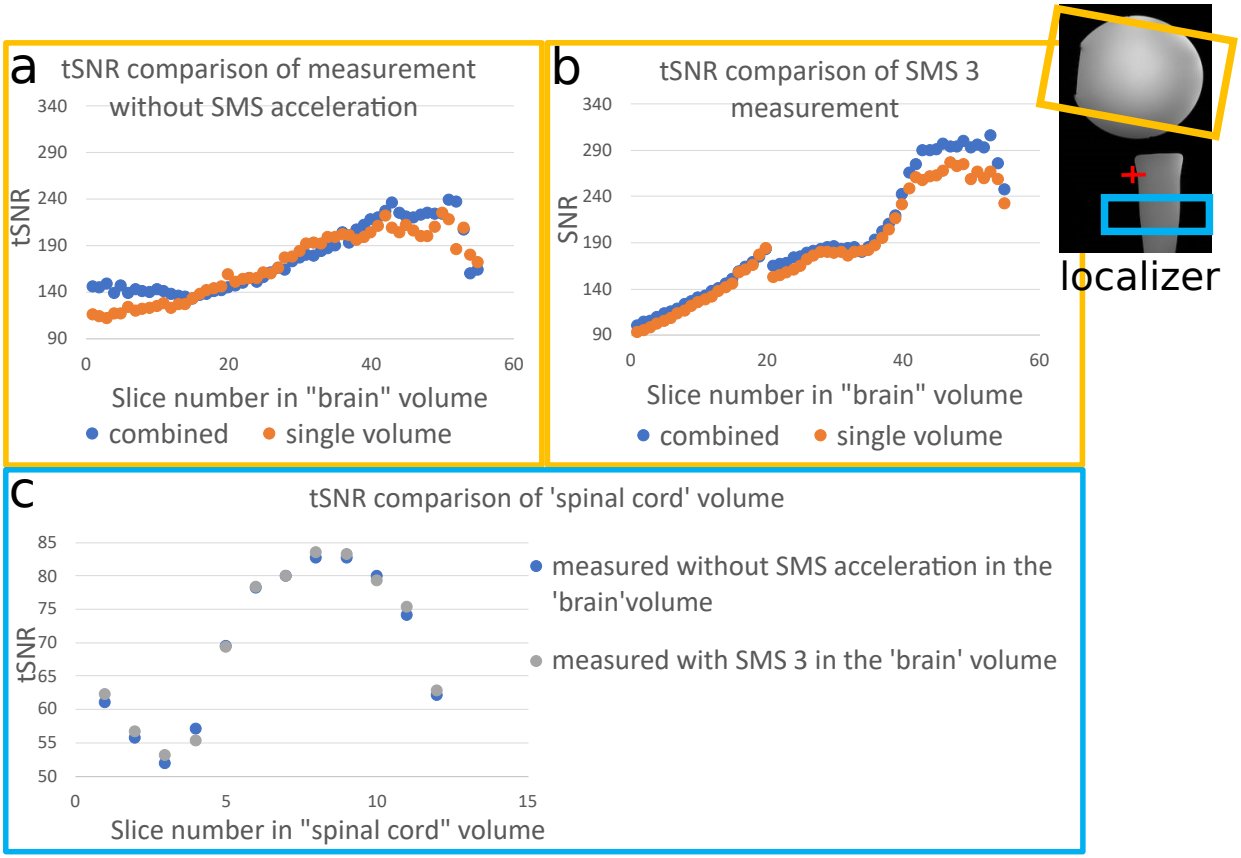

Figure **5-2**: Results of tSNR in a water phantom setup, which mimics the in vivo setup. (a) Without SMS acceleration for combined and single-volume acquisitions. (b) With SMS with an acceleration factor of 3 for the "brain" volume only for combined and single volume acquisitions. (c) "spinal cord" volume during the combined measurement for both without and with SMS in the "brain" volume.

5.3.1 tSNR

Figure **5-2**c shows that for the phantom experiment in the "spinal cord" volume, there is no impact of SMS acceleration of the brain volume observed. This means the SMS acquisition and newly implemented reconstruction for the brain slices do not interfere with the non-accelerated spinal cord slices. In comparison to the single-volume acquisition, the combined acquisition has a tSNR difference over the whole volume of +4% for acquisition without SMS and a tSNR difference of +5% for acquisition with SMS 3 in the "brain" volume.

Figure **5-3** shows the tSNR from gray matter only of an in vivo results, which deliver similar results to the phantom results. In the spinal cord volume, there is no impact of the SMS acceleration of the brain volume observed. This means the SMS acquisition and implemented reconstruction for the brain slices do not interfere with the non-accelerated spinal cord slices. In comparison to the single-volume acquisition, the combined acquisition

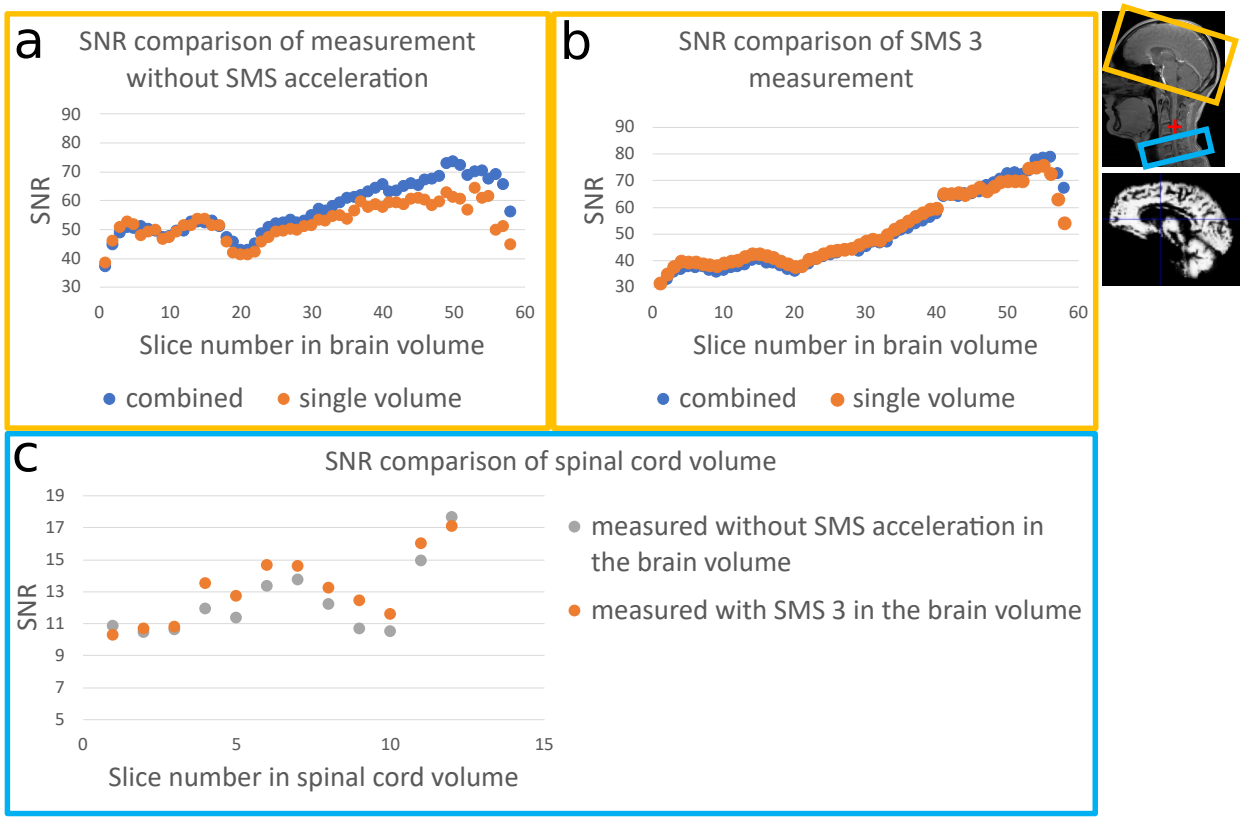

Figure **5-3**: Results of tSNR in gray matter for all slices for an in vivo volunteer. (a) Without SMS acceleration for combined and single-volume acquisitions. (b) SMS with an acceleration factor of 3 for the brain volume only for combined and single-volume acquisitions. (c) The spinal cord volume during the combined measurement for both without and with SMS in the brain volume.

has a tSNR difference of 7% (gain) for acquisition without SMS and a tSNR difference of 2% (loss) for acquisition with SMS 3 in the brain volume.

tSNR curves show that the acquisitions with SMS have two interruptions (between slice 20 and 21, and between slice 40 and 41) in the tSNR curve over the slices. And both combined and single-volume results behave the same; therefore, it does not come from the implemented reconstruction. It is a general SMS reconstruction issue. This effect could be related to filtering performed in SMS reconstruction.

There are only minor differences in terms of tSNR from the phantom measurement and in vivo images between the SMS image without (single volume) and with (combined) the self-modified reconstruction pipeline.

As a result, we can say that partial SMS acceleration with factor 3 is feasible for brain coverage and does not make a quality difference with regards to tSNR in comparison to single volume coverage with SMS. However, for now, we can only see that the mean tSNR within one slice is good. Therefore, we would also like to look into the local differences,

i.e. increase in one, and a decrease in another region is bad but would yield a similar mean value. The tSNR value maps for gray matter for single volume acquisition without SMS acceleration, single volume acquisition with SMS 3, and combined volume acquisitions with SMS 3 were shown in figure **5-4**. It shows that there is no local tSNR disadvantage for the different acquisitions locally.

5.4 Summary and Conclusion

Partial SMS acquisition and reconstruction were implemented and tested. There is less tSNR loss compared to non-accelerated acquisitions. However, it results in a volume coverage and/or temporal resolution gain.
The minimum TR for full brain coverage and C6 and C7 spinal cord coverage can be reduced from more than 4s to below 2s, when using SMS acceleration in the brain. If we want to achieve the same minimum TR of below 2s without the use of SMS, we would have to reduce the brain coverage by two third.
To conclude, the partial SMS method works for the combined fMRI measurement, which improves the volume coverage and/or temporal resolution. This is essential for the optimization of brain and spinal cord combined T2* weighted fMRI.

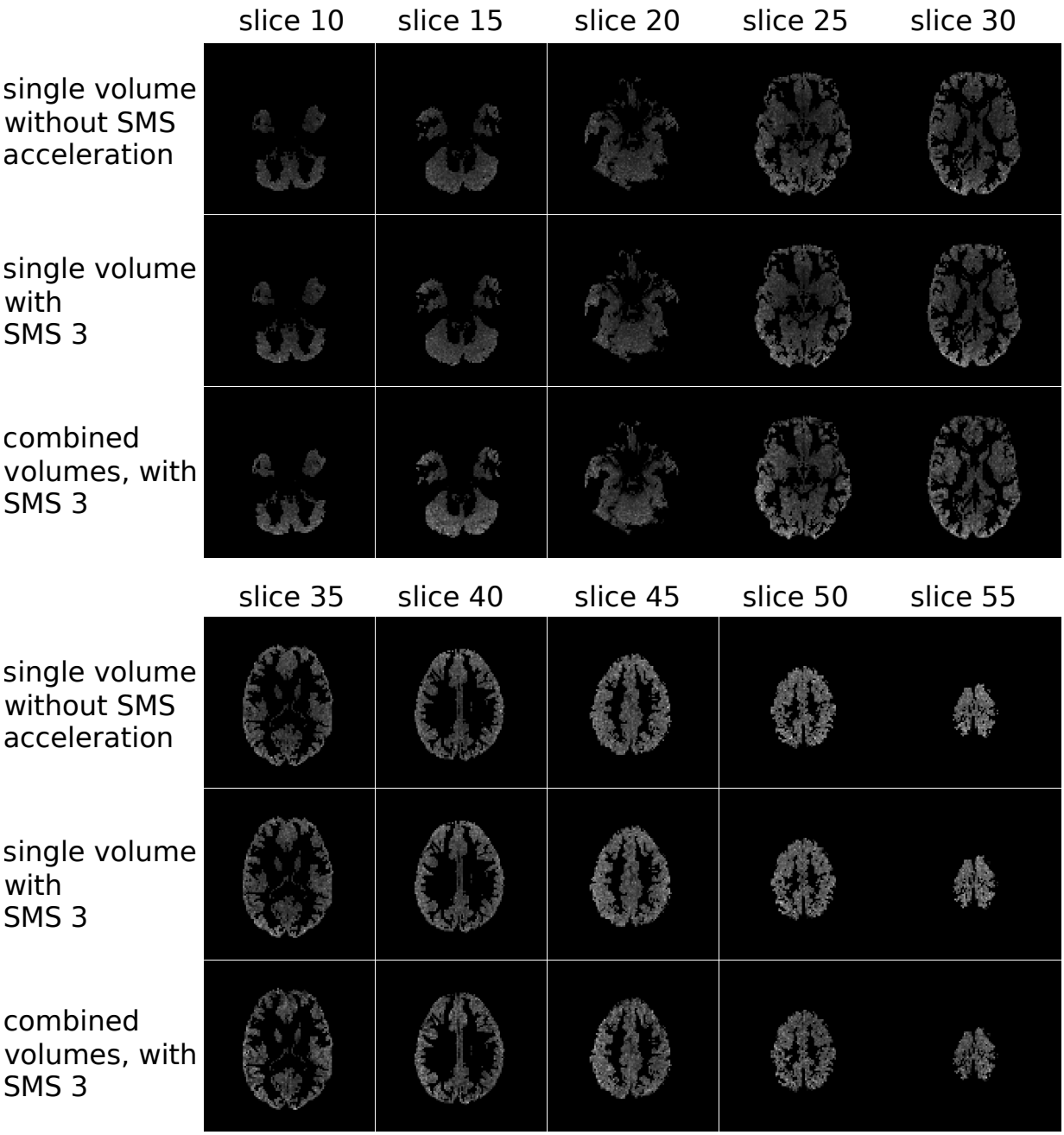

Figure **5-4**: tSNR maps for the gray matter of ten brain slices obtained in a healthy volunteer with single brain volume without SMS acceleration, a single brain volume with SMS 3, and brain and spinal cord volume ("combined") with SMS 3. All images were scaled with the same gray values.

6 On-the-Fly Reconstruction

The desired geometry and timing parameters differ between brain and spinal cord fMRI due to different resolutions and FOV. Nevertheless, combined fMRI acquisitions could be realized with "ideal" parameters for both volumes. However, the standard image reconstruction is not able to handle two sets of such parameters in a single acquisition. As a consequence, image file data like voxel size, TE, and bandwidth contain only the values from one of the volumes. More importantly, some calculations and corrections performed will be wrong for the other volume, e.g. the calculation of ramp sampling or correction of concomitant field-induced distortions or coil sensitivity-related image intensity differences. As a workaround, a retrospective reconstruction was used in the past [40]. After finishing the measurement, reconstruction parameters that are used to configure functions of the reconstruction chain are changed to the parameters of the other volume, and the reconstruction is started again. This method is error-prone and difficult and needs to be done multiple times, which means additional time is needed, which blocks the MR system.
In this chapter, extended image reconstruction has been implemented that considers the correct parameters for each volume for all calculations and ensures that parameters stored in the image files have the correct values, which avoids retrospective reconstruction.

6.1 Setup and Parameters

For the Measurement, a brain and spinal cord combined EPI sequence is used as shown in figure **2-21**. The phase and frequency encoding gradients show the different geometry and timing parameters of these two volumes.
For EPI, the parameters from sections 2.5 are used. Both volumes had a TE of 30ms, which yields a minimum TR of 2696ms for these 40 slices (brain and spinal cord).

6.2 Regridding

For typical fMRI measurements, the typical bandwidth for brain and spinal cord volumes differs. The higher the in-plane resolution, the smaller bandwidth per pixel is required. This difference in bandwidth per pixel affected the echo spacing for the two subvolumes. The smaller the desired bandwidth per pixel, the longer the echo spacing to acquire the same amount of pixels.

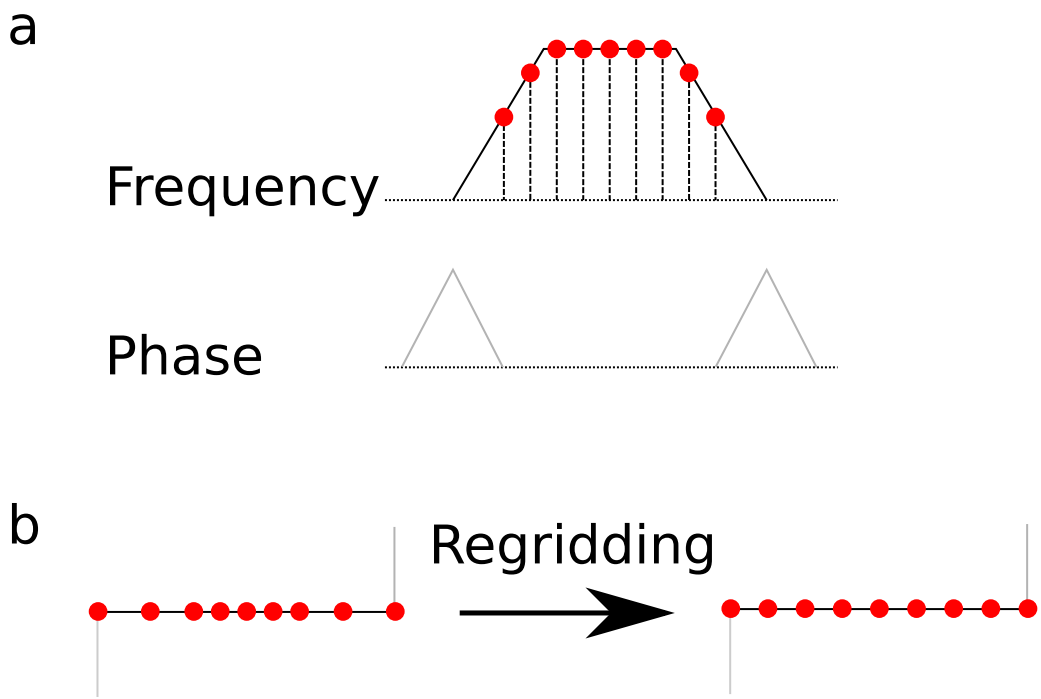

Figure **6-1**: Illustration of (a) sampled data and (b) regridding in k space. (a) The red points on the gradient trapezoid visualize the equidistant sampling points and (b) how they are distributed on the k space line.

Ramp sampling [5] was applied during the readout gradient pulses for both brain and spinal cord subvolumes to minimize the echo spacing. However, because of the equal distant sampling, the data sampled on the ramp shows a bigger distance for the acquisition lines on k-space, as shown in the figure **6-1**. Without a correction on it, there are ringing-like artifacts on the images, as shown in **6-3**. To correct the sampling as an equal distant sampling on the k space, regridding [27] needs to be used, in which the data points are interpolated to the desired position.
To do so, the correct duration of the ramp time, echo spacing and plateau time of the frequency encoding gradient, and blip time of the phase encoding gradient should always be considered. However, the standard reconstruction can only consider one set of these parameters. For this project, the corresponding parameters for different subvolumes were considered and sent in the extended on-the-fly reconstruction pipeline.

6.2.1 Method

To address the different timing parameters and gradient amplitudes of the different volumes, the reconstruction pipeline is extended, as shown in figure **6-2**. A branch functor prior to the regridding needs to be inserted in the pipeline. This branch functor has two exits. An additional regridding functor is created with the parameters of the second volume. Then,

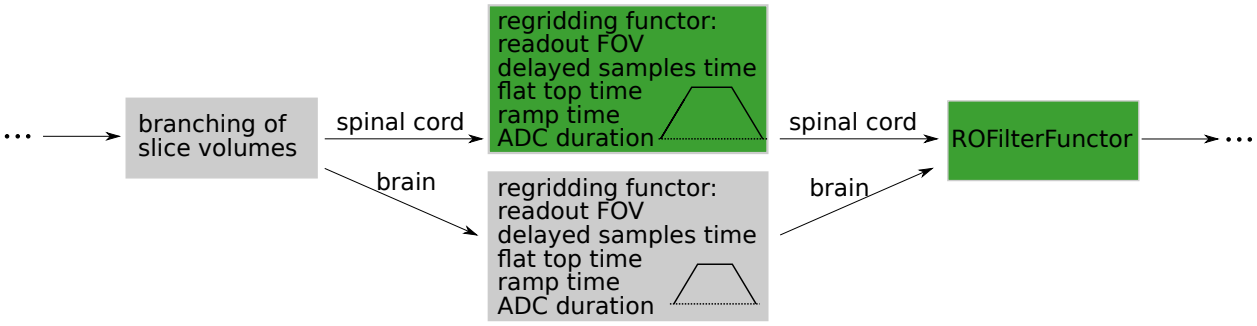

Figure **6-2**: The extended reconstruction pipeline. The green blocks represent standard functors. The gray blocks represent functors that be extended. The three points represent the omission of the functions of the reconstruction pipeline.

this additional regridding functor is inserted after the second exit. This branch functor splits the data via the slice volume. The spinal cord continues along the standard chain and the brain volume continues along the second exit.

6.2.2 Results and Discussion

Both retrospective reconstruction and the extended pipeline use the spinal cord as standard volume, which can already be reconstructed perfectly on-the-fly before. Therefore, only brain images are shown in this chapter. The retrospective reconstruction of the brain volume is also not shown. As it handles a pipeline extension, there are no differences between the parameters of retrospective reconstruction and the on-the-fly reconstruction.
Figure **6-3** shows the results of the phantom acquisition. Figure **6-4** shows the effect of different timing parameters on the regridding of the ramp-sampled data for the brain volume in one in vivo acquisition. In both figures, ringing-like artifacts appear at the edge of the phantom/brain when the regridding is performed with the spinal cord parameters; using the brain parameters, there is no ringing-like artifact to observe. Especially in the homogenous water phantom, the ringing-like artifact at the edge of the image is obvious.

6.3 Concomitant Field

Concomitant magnetic-field-induce artifacts in EPI, which needs to be corrected [41]. The artifacts arise from the higher-order magnetic fields produced when a linear magnetic field gradient is desired. This desired linear magnetic field gradient does not fulfill the Maxwell equations because they produce higher-order fields than only the desired basic linear gradients. In other words, the linear gradient is designed to produce a specific magnetic field at each point in space, but in reality, higher-order fields are also produced due to Maxwell's

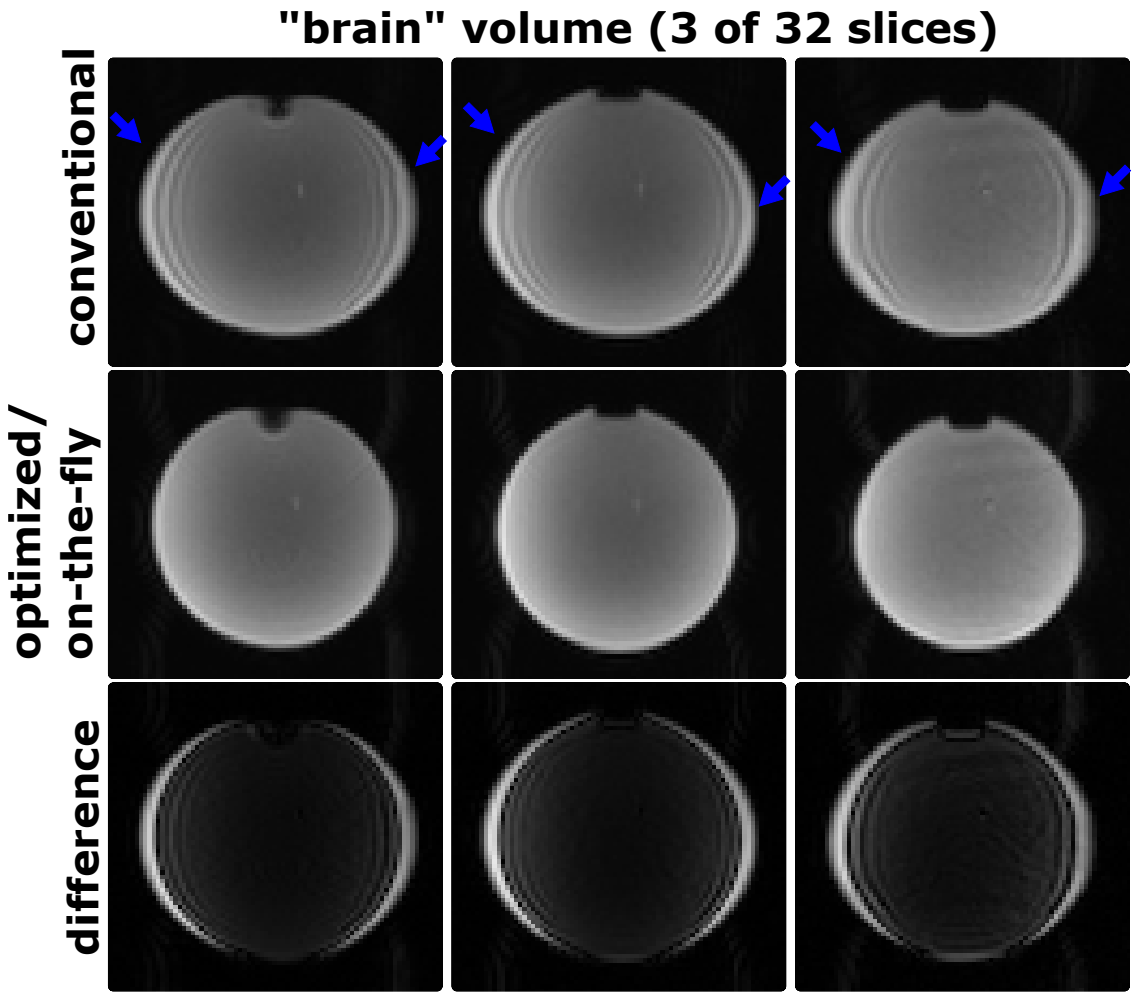

Figure **6-3**: Ringing-like artifacts on a water phantom. The first row is a conventional original reconstruction using the standard reconstruction pipeline. The second row is the acquisition with optimized retrospective reconstruction or the newly implemented on-the-fly reconstruction. The third row is the difference map of the images of the first two rows. The blue arrows in the first row show the ringing artifact.

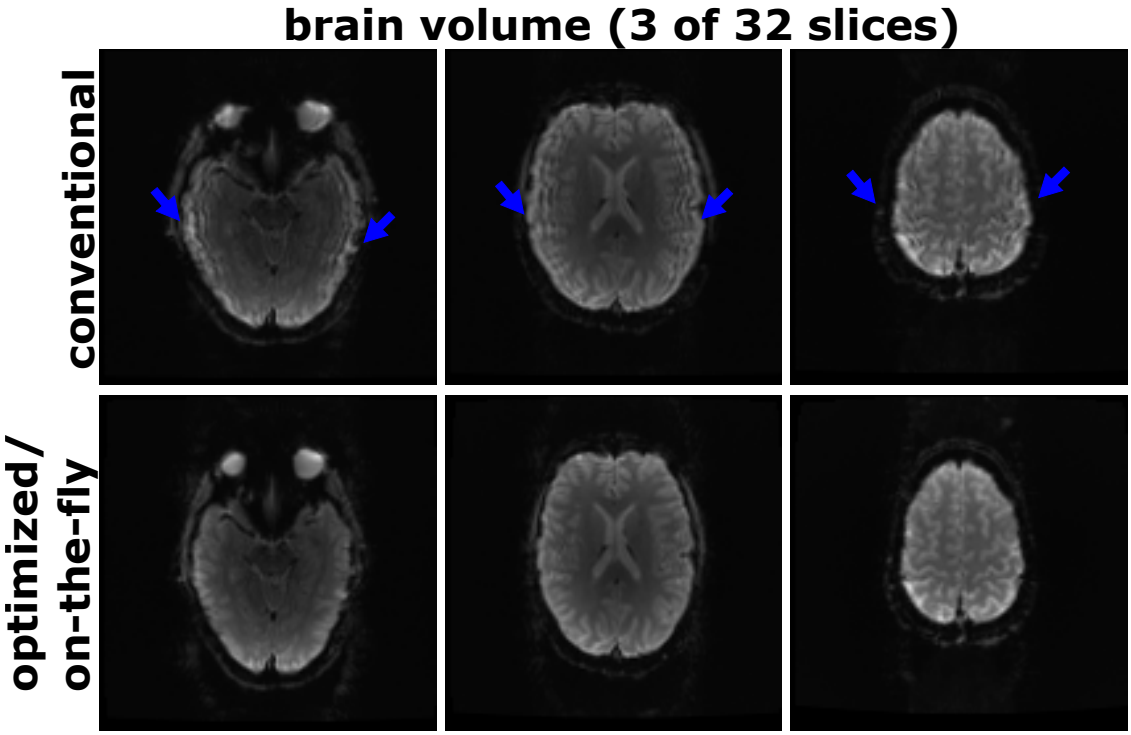

Figure **6-4**: Ringing-like artifacts on an in vivo experiment. The first row used a conventional reconstruction. The second row is the acquisition with optimized retrospective reconstruction or the newly implemented on-the-fly reconstruction. The blue arrows in the first row show the ringing artifact.

laws. These concomitant magnetic higher-order fields give a field of

$$B_{\text{concom}} = \frac{z^2 G^2}{2B_0} \tag{6-1}$$

which yields a phase shift of

$$\Phi_{\text{concom}} = \frac{\gamma z^2 G^2 t_G}{2B_0} \tag{6-2}$$

where t_G is the duration of the gradient field, γ is the gyromagnetic ratio, z is the position of the current slice, G is the desired gradient field, and B_0 is the main magnetic field. From the equation above, we know that a spatially varying phase shift is on the direction of the main magnet z-direction. This phase shift, dependent on the z-position, produces a shift for the whole EPI image, and together with the phase offset created from the frequency gradient, they result in a shearing artifact on the volume.
To correct the shearing effect caused by the concomitant field, we use the known integral of the square of the gradient field and echo spacing (t_G), which is called Maxwell integral, to compensate for the shift effect induced by the higher-order magnetic fields. Therefore, the concomitant magnetic field depends on the slices' position and echo spacing.

6.3.1 Method

For the correction of the concomitant field, specific "Maxwell Integral" and echo spacing need to be used for the reconstruction pipeline. To achieve it, the slice group of brain volume need to be modified with a specific "Maxwell Integral" and echo spacing. A similar branch and copy of the maxwell function is used as shown in figure **6-2** with the correct "Maxwell Integral" parameter and echo spacing parameter.

6.3.2 Results and Discussion

Figure **6-5** shows that both in phantom and in vivo acquisition, a significant shearing of the brain volume can be observed with the conventional on-the-fly reconstruction. This shearing effect is corrected with the modified reconstruction pipeline on-the-fly, which realizes the image quality of the retrospective reconstruction.

6.4 Correction of the Receive-Coil Sensitivity Inhomogeneities

Because arrays of small receive coils are placed outside of objects, their sensitivities at different positions of the scanned object are different. Therefore, a correction of receive-coil inhomogeneities can usually be done, called prescan normalization, which determines

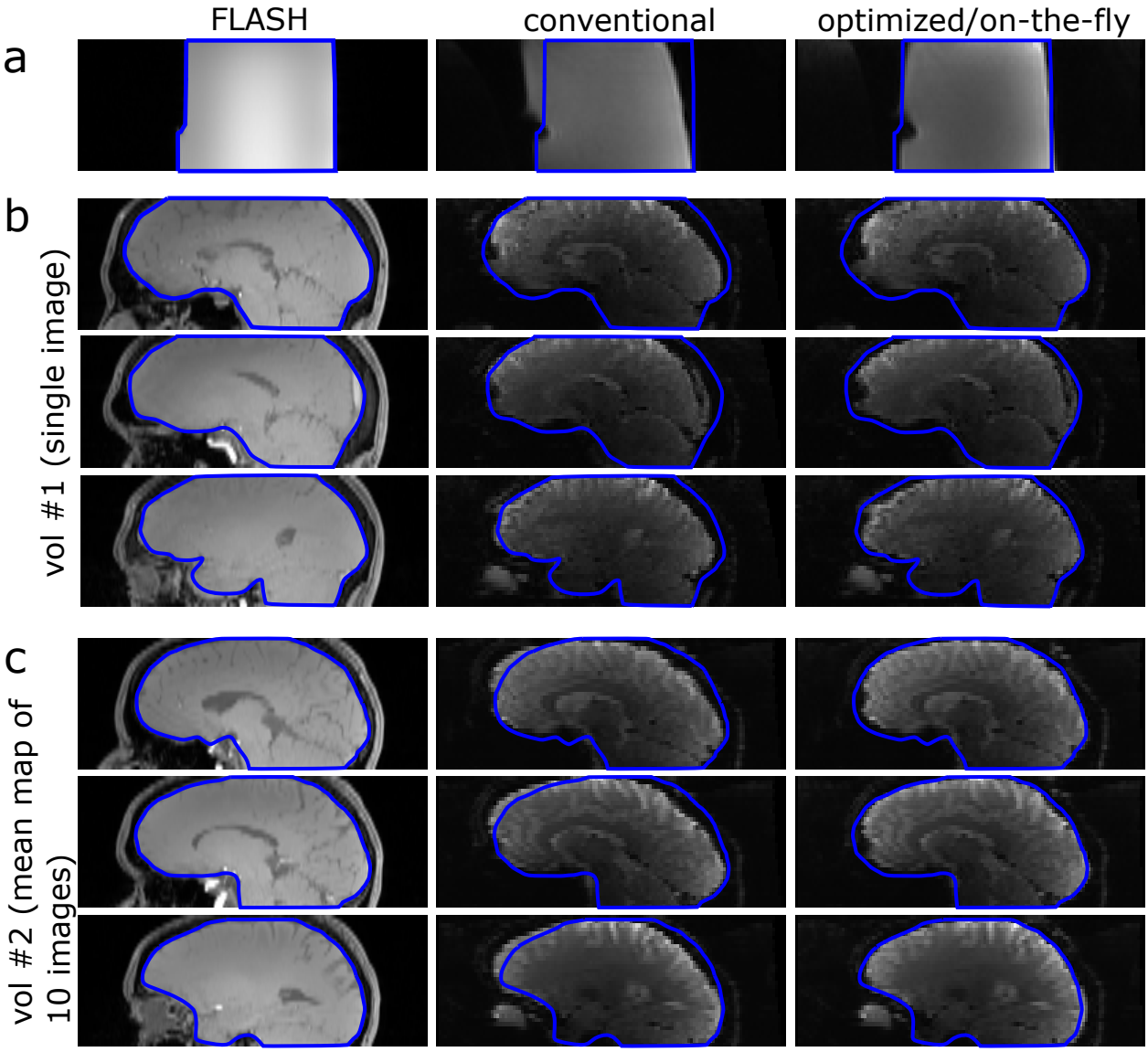

Figure **6-5**: Effect of volume-specific parameters on the correction of EPI distortions caused by concomitant field gradients in (a) phantom and (b,c) healthy volunteers, the distortion is compared with the anatomic reference (FLASH acquisition, which does not suffer from concomitant field effects). The blue contours represent the outline of the brain from the anatomical reference images.

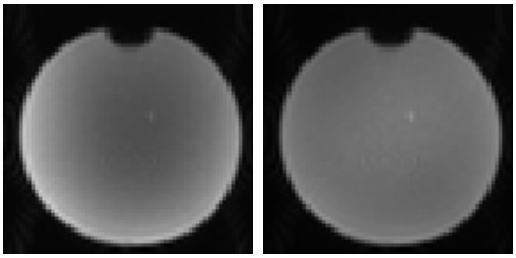

Figure **6-6**: Transversal images of a water phantom filled with homogenous water for both without prescan normalization (left) and with prescan normalization (right).

the spatial distribution of coil sensitivities and corrects pixel intensities accordingly. This correction is based on an independent measurement over a big volume.
The image shown in figure **6-6** (left) shows that the water phantom image, which should contain a homogenous signal across the cross-section, contains non-homogenous signals.

6.4.1 Method

A self-written reconstruction functor containing data of the slice geometry parameters (field-of-view, pixel spacing, slice thickness) of the brain volume with the reconstructed image is inserted in the reconstruction chain.

6.4.2 Results and Discussion

The influence of the geometric parameters on the correction of the receive coil sensitivity is presented in figure **6-7** in a phantom. The conventional reconstruction does not consider the modified field-of-view size of the brain slices and, thus, does not perform a proper correction. In contrast, the modified program is able to provide a good correction with homogenous signal amplitude across the phantom.
Figure **6-8** shows brain images obtained with the retrospective and the modified on-the-fly reconstruction. The modified pipeline performs as well as the retrospective reconstruction with respect to regridding and correction of the concomitant field. However, the optimized on-the-fly reconstruction pipeline applies a proper correction of the coil sensitivities, which yields a more homogeneous signal intensity distribution across the brain.

6.5 Summary and Conclusion

In conclusion, the extended on-the-fly reconstruction pipeline performs an optimized reconstruction regarding regridding and correction of concomitant field effects for the brain volume for the combined fMRI acquisition without a time-consuming retrospective reconstruction

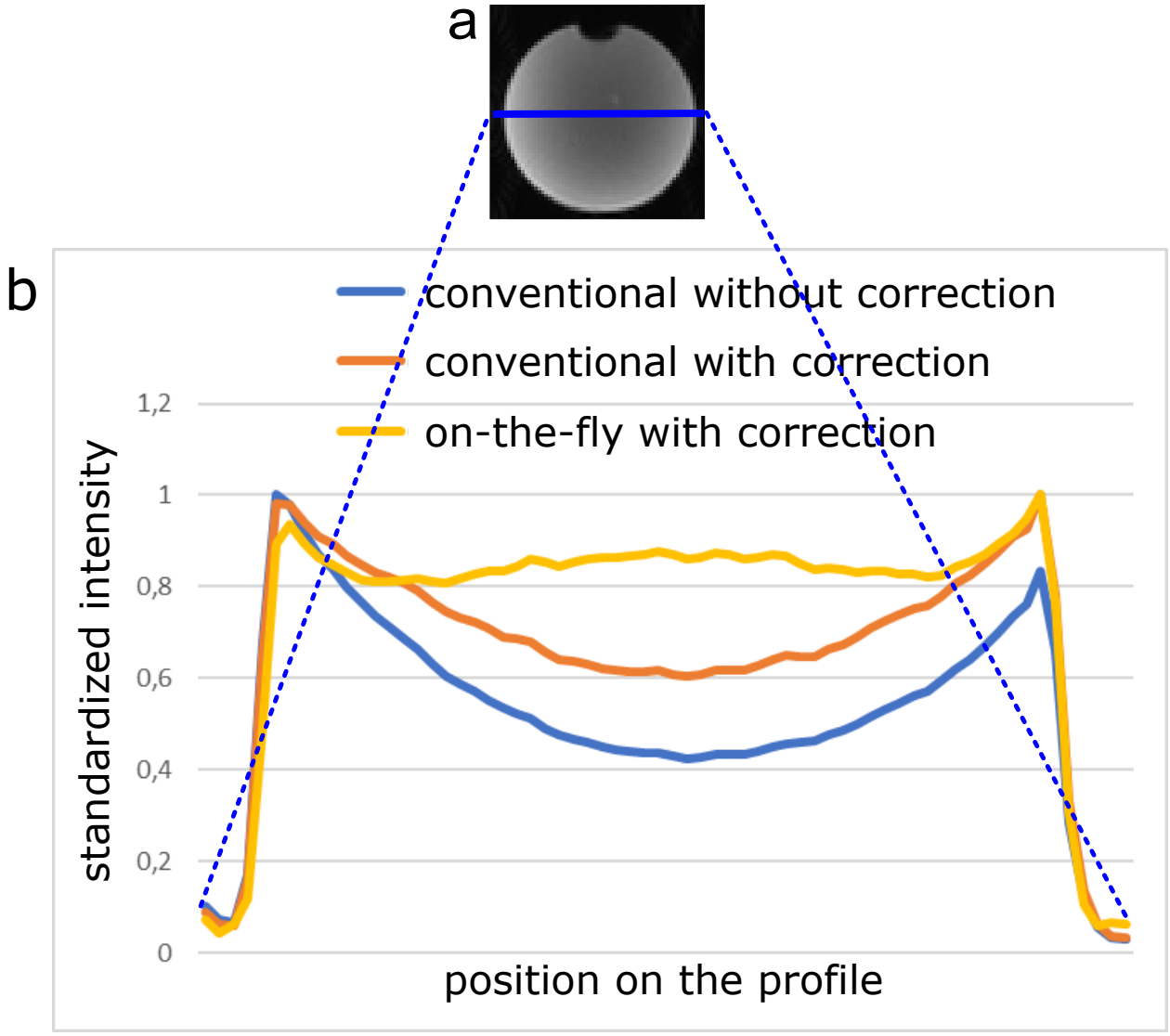

Figure **6-7**: (a) Transversal image of a water phantom without correction. The blue line represents the profile considered in (b). (b) Plots of the signal profile along a horizontal line (the blue line in (a)). The optimized on-the-fly reconstruction (yellow) provides a more homogeneous signal intensity than the conventional approach (orange) or reconstructions without correction (blue).

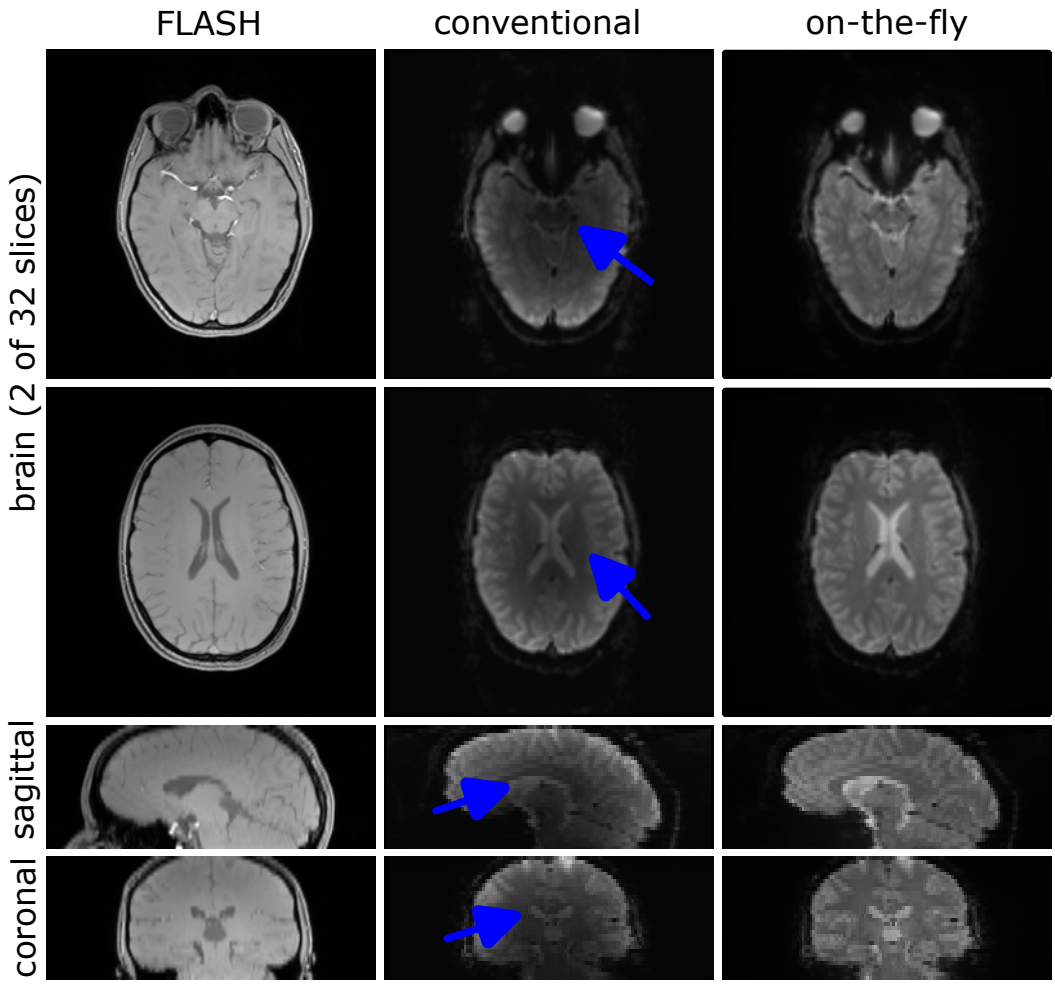

Figure **6-8**: Comparison of the anatomic reference image with FLASH (left column), conventional reconstruction without coil sensitivity correction, and fully optimized on-the-fly reconstruction with modified reconstruction pipeline. For each, two selected transversal images, one sagittal and one coronal plane image, are shown. The arrows show the signal inhomogeneity in the middle of the brain.

on the scanner system. Furthermore, it can correct the inhomogeneity of the coil sensitivity. Thus, this on-the-fly reconstruction pipeline can help the applicability of the brain and spinal cord combined fMRI.

7 A Navigator Echo for Motion Correction of Spinal Cord fMRI

A spinal cord fMRI study can take longer than 1 hour and usually lasts more than 30 minutes. It is difficult for both healthy volunteers and weak patients to not swallow and have strong respiratory activity for that long. However, both activities can move the spinal cord, which is hard to detect and correct due to its shape, size, and inner structure not changing very much along the cord's axis (as shown in figure **7-1**). In the previous spinal cord fMRI studies [14] [40], the motion detection and correction in the cord's axis direction is based on the intervertebral discs from the transversal acquisitions. However, the slice thickness of spinal cord acquisition is usually not less than 3.5mm, and the periodicity of the spine structure may cause wrong assignments yielding stepwise movement by several centimeters. Thus, a manual check is always required. Furthermore, on-the-fly correction is ideal for repositioning slices upon motion, particularly with respect to z-shim.

Also, if we consider the inner FOV imaging technique[17], which is a method to improve the spinal cord imaging quality (with respect to geometric distortion) by focusing the excitation on a smaller area, there is no disc for the motion correction software to consider, as shown in figure **7-2**.

Here, a columnar navigator scan involves acquiring a projection of the spine with a better spatial resolution. This image can be acquired repeatedly throughout the MRI scan, e.g., once per image or volume. Here, it is shown that a navigator measurement of a columnar volume (c.f. Fig. **7-3**a) based on 2DRF excitation (refer to section 7.1) along the spine axis can be used to estimate spine movements in this direction with high spatial resolution. As shown in figure **7-3**a, along the spine, the intensity profile along the disc can provide a clear pattern due to the intensity difference between the intervertebral disc and vertebral body that can be used for motion correction. This approach can provide a much better spatial resolution, i.e., the precision of the obtained displacement, and is compatible with inner FOV imaging [17]. Thus, it could help to improve motion correction in spinal cord fMRI acquisitions. This is essential for future on-the-fly correction work. By comparing the navigator images with each other, we can detect motion that has occurred along the spine direction and use this information to adjust the imaging parameters (i.e., slice position) even in real-time, which makes sure the z-shim (refer to section 4) determined is still up-to-date.

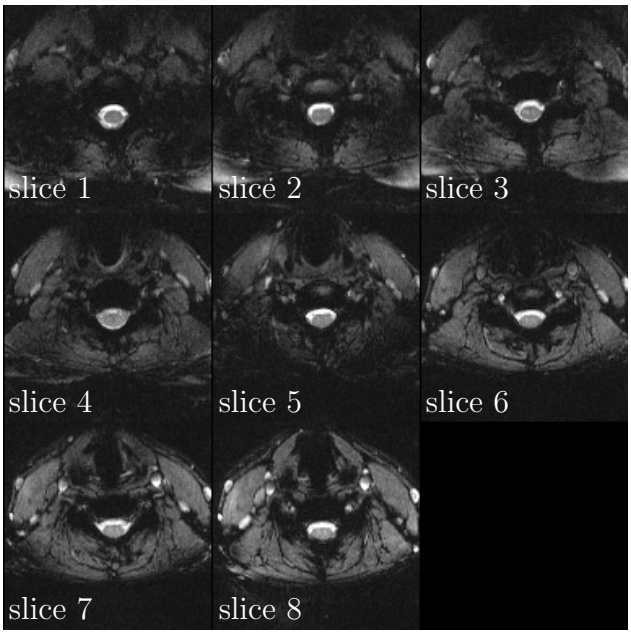

Figure **7-1**: Eight successive slices of the cervical spinal cord

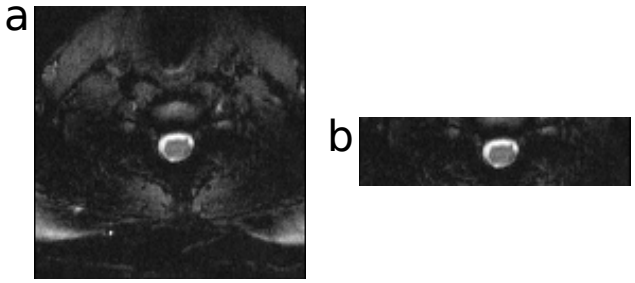

Figure **7-2**: Example single-slice EPI data of spinal cord acquired with (a) a conventional full FOV and (b) inner FOV based on a 2DRF excitation.

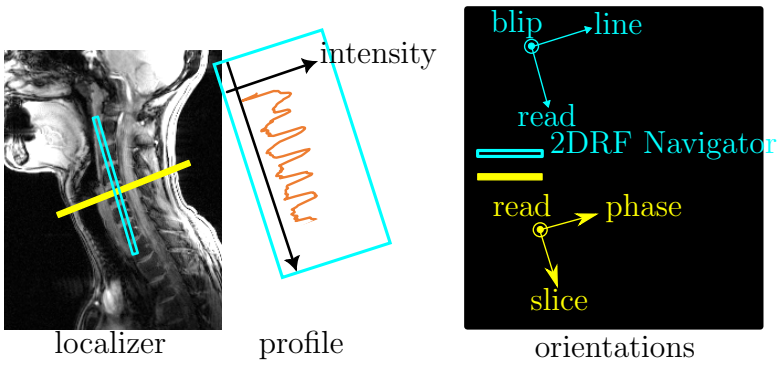

Figure **7-3**: Localizer illustration of a navigator echo. (a) Localizer with basic geometric setup of the navigator (blue) and a single EPI (yellow) slice. (b) One orientation possibility for the navigator and slices. The line direction correlates with lines in the k space trajectory in the k space for excitation.

7.1 Theory of 2DRF Excitation

This navigator measurement is based on the two-dimensional spatially-selective radio frequency (2DRF) [34] excitation. This method can be used to measure smaller FOVs than the object without aliasing. In this case, the 2DRF excitation only creates a columnar excitation through the spine.

Pauly has developed the k-space description for 2DRF excitations [34], which establishes a connection between the envelope of an RF pulse and its corresponding excitation volume. It ignores the relaxation during the excitation. Similar to the k-space trajectory for data acquisition in equation 2-38, the K-space trajectory for a selective RF excitation is given by

$$\vec{K}(t) = \gamma \int_t^T \vec{G}(t')dt' \tag{7-1}$$

This formula shows the integration from the time t to the time of the end of the excitation pulse T. We assume that at the start time, the magnetization aligns in the z-direction in the thermal equilibrium, which means that the initial magnetization has the state (0, 0, M_0). We have

$$M_{xy}(\vec{r}) = -i\gamma M_0 \int_k W(\vec{K}) \cdot S(\vec{K}) e^{-i\vec{r}\vec{K}} d\vec{K} \tag{7-2}$$

where $W(\vec{K})$ can be determined by

$$W(\vec{K}(t)) = \frac{B_1(t)}{|\gamma G(t)|} \tag{7-3}$$

where $S(\vec{K})$ is the spatial sampling function. $S(\vec{K})$ defines a discrete and finite trajectory in the k-space. Therefore, the excitation profile is periodic and imperfect after the inverse

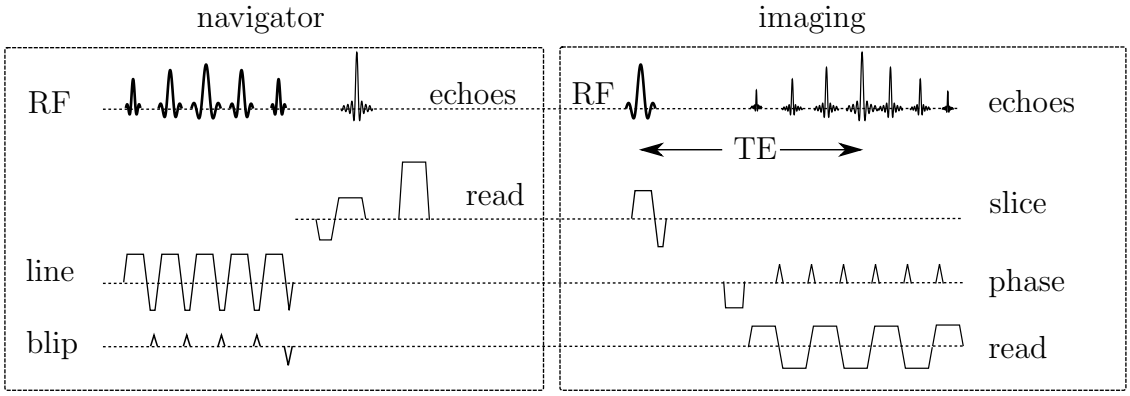

Figure **7-4**: Example pulse sequence used in the navigator experiments composed of a navigator part (left) based on a blipped planar 2DRF excitation with fly-back trajectory and a standard EPI shot (right). The orientations of the navigator and image acquisition can be rotated independently. In this case, the navigator slice is perpendicular to the slice of the image, as shown in figure **7-3**

Fourier transforms. Besides the main excitation, we will also have infinite periodic side excitations. The distance between the main excitation and the nearest side excitation is the field of excitation (FOE). A signal contribution of the side excitation can be avoided by positioning the side excitation outside of the object.

7.2 Method

The basic geometric setup is shown in figure **7-3**a, and the orientations of the slice and the navigator column are shown in figure **7-3**b. The figures show that the navigator measurement is perpendicular to the slice stack, and the navigator is positioned along the spine.

7.2.1 Sequence and Parameters

A columnar excitation is needed to achieve a columnar measurement in MR acquisition. We use a 2DRF excitation [34] [17] for the excitation part of the navigator measurement and only a single echo of the data acquisition is needed for every navigator measurement as we only need one projection profile of this columnar excitation. The sequence diagram is shown in figure **7-4**.

The fly-back blipped planar spatial sampling function is used (c.f., figure **7-4**), which has line gradients in one direction and blipped gradients in its orthogonal direction for the excitation; therefore, the side excitations are in the blip direction, which is the left-right direction, which can be shifted outside of the human body easily. Usually, a low-resolution of 2DRF excitation profile is chosen to reduce the excitation duration. Also, the FOE increase with an increased

sampling density; however, an increased sampling density increases the excitation duration and, hence, the echo time (TE).
The experiments involved instructing the volunteers to first rest and then move their head and neck area back and forth along the head-feet direction. The 2DRF excitation (flip angle 10°) had a spatial resolution of $5\times10\text{mm}^2$ (line $\times$ blip) with the blip direction oriented along the left-right direction with a FOE of 150mm to position the side excitations outside of the human body. To reduce Gibbs ringing, a Gaussian filter was applied to the RF envelope, reducing the calculated amplitude values by 85% at the edges of excitation in the k-space. The navigator data were acquired with a single echo in frequency encoding direction with a bandwidth per pixel of 495Hz and a spatial resolution of 1mm, covering a field-of-view of 128mm. The signal is then Fourier transferred to columnar data. The overall duration of the navigator part (c.f., figure **7-4**) was 13.8ms for each shot. A single-slice mock EPI shot (data not stored) was also performed in between. Every measurement (with and without movement) contains 128 navigator echoes, and, therefore, 128 single-shot EPIs. Each combination of one navigator echo and one single shot EPI with waiting time costs 200ms, yielding a temporal resolution of 200ms for motion detection experiment shown in this chapter. Therefore, the acquisition time for each experiment (with and without movement) is 25.6s.

7.2.2 Data Analysis

Figure **7-5** shows the analysis workflow of the experiment. First, after the image acquisition, the navigator signals are presented as columns, as shown in picture (b). Then the movement of one intervertebral disc is analyzed. As a result, if we do the convolution process with the reference vector and all subsequent lines shown in (c) and (d), we can obtain a plot to show the shift of the single intervertebral disc over a time axis as shown in (e) in figure **7-5**.

7.3 Results

Figure **7-6** shows the results. For the rest condition, the navigator signal from the target disc, which is emphasized within the red block, shown is very stable in time, with the plot of the position of the target disc representing a straight line during the time series in figure **7-6** (c). In other words, the data analysis did not show any displacement. For the movement measurement (Fig. **7-6** (d)), the navigator signal shows a periodic signal variation. The shifts (Fig. **7-6** (e)) obtained from the data analysis also clearly reflect this periodic movement.

7.4 Discussion and Conclusion

The analysis and results of this chapter show that a navigator along the spine can detect motion along the spine's axis with a high spatial (e.g. 1mm) resolution. The overall duration

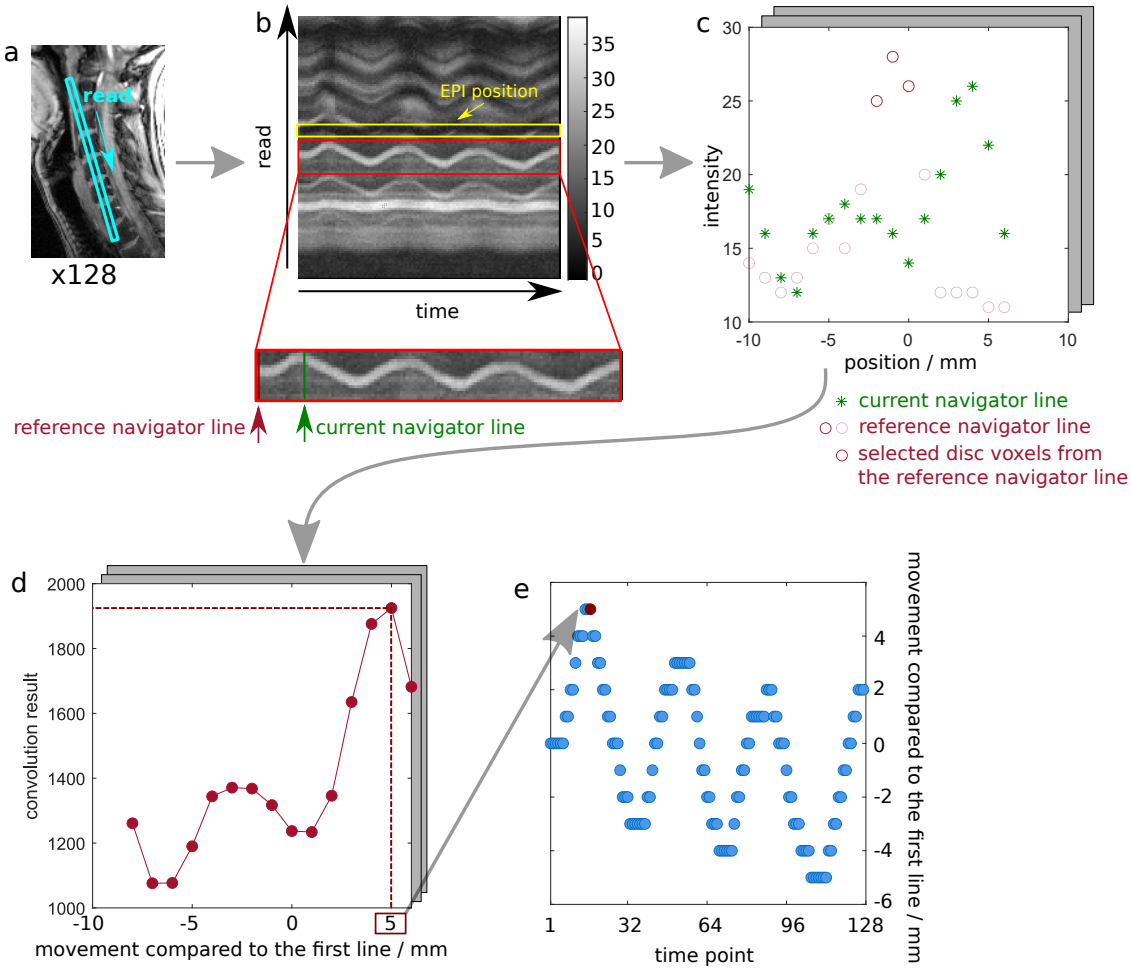

Figure **7-5**: Analysis workflow for the volunteer experiment. (a) shows a localizer with the navigator's position (blue). (b) shows 128 navigators acquired with a temporal/spatial resolution of 200ms/1mm as 128 columns. The zoomed areas contain the signal from the selected disc. We recognize the EPI slice with a fixed spatial position that saturates the magnetization and shows up as a dark band in the navigator signals, as shown with the yellow block. We use the first echo as the reference. One example of the position of the green arrow is shown in the following steps. (c) shows signal plots of both navigator lines considered. The position of the intervertebral disc is calculated. The voxels with an intensity greater than 0.7 times the maximum intensity value are defined as the intervertebral disc. A convolution of the two peak signals reveals a maximum if both peaks match. The required shift is considered as the movement of the spine at the time of the considered line. Afterward, the convolutions between this reference vector and the subsequent lines (green stars) were calculated. Finally, (d) shows the result of the convolutions, the positions of the largest convolution value show the shift directly because they are the position where the reference vector and the current line matched.

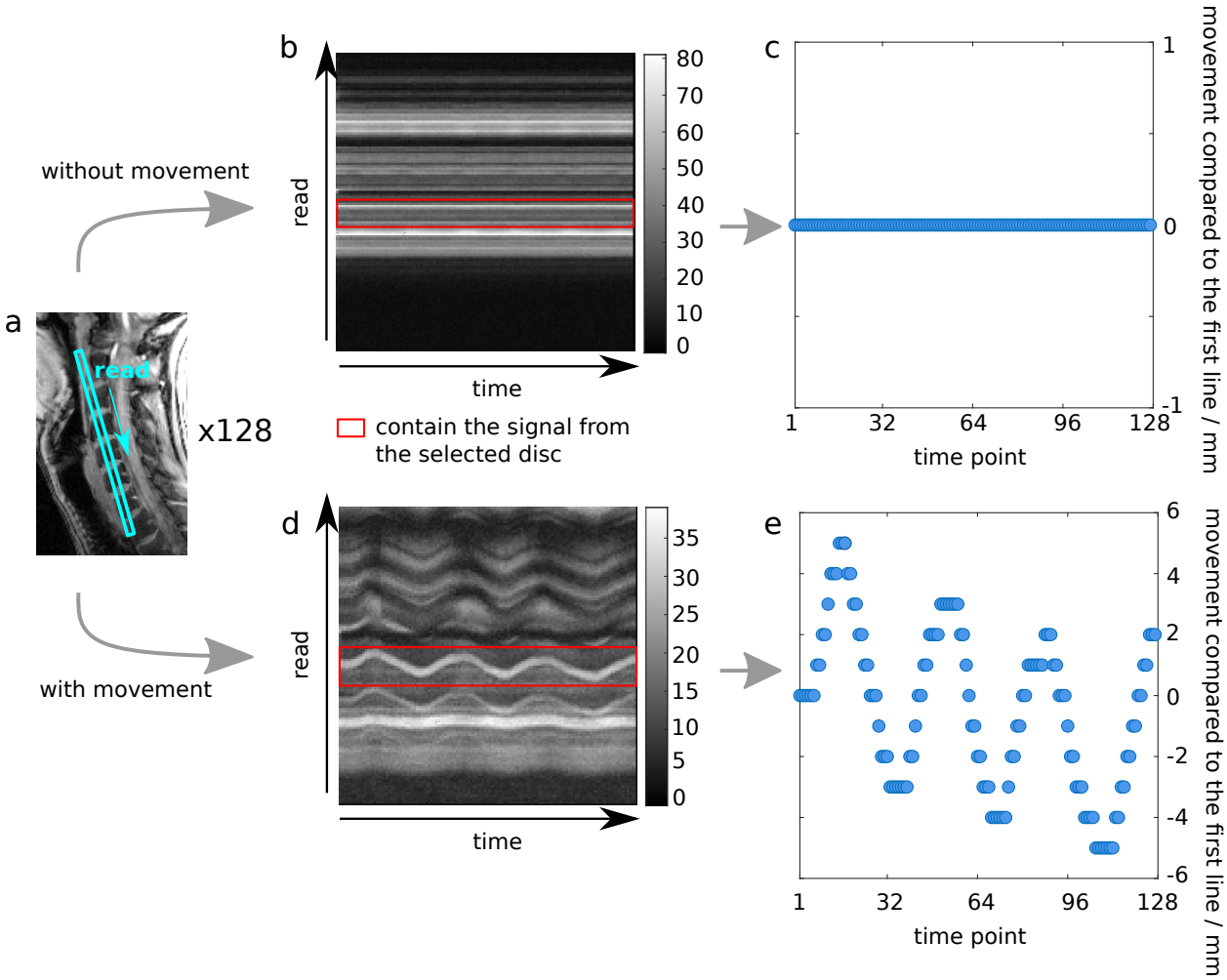

Figure **7-6**: Results of navigator echo. (a) Localizer image. (b) and (d) Navigator consisting of all navigator acquisitions for (b) rest condition and (d) movement measurement. The abscissa axis from (c) and (e) is the time point of the navigator echoes, and the vertical axis is the relevant displacement for the subsequent lines compared to the reference line.

of the navigator part was 13.8ms, which only adds a small fraction of scan time for every volume of a typical fMRI (between 2 and 3s). This study uses a similar motion detection idea like previous studies [40], which rely on fMRI data that have used spine displacements to represent spinal cord movements along the spine's axis direction. The navigator echo method also provides a higher spatial resolution and is compatible with inner-FOV imaging [7], which may reduce geometric distortions and improve tSNR for EPI in spinal cord volume. Therefore, the navigator echo approach can help to improve motion detection in spinal cord fMRI.

To date, this subproject focused on whether the spine information from a single columnar acquisition is sufficient for a displacement of the slice and the implementation of the navigator echo. For future work, an on-the-fly detection and correction of the slice displacement is desired. One main reason is that the reference scans-based z-shim approach (refer to chapter 4) is sensible with regards to a displacement of the slice position.

To achieve the on-the-fly detection and correction of the slice displacement, the reconstruction pipeline needs to be extended to make it able to transfer the new slice information into the sequence and change the slice information from the upcoming acquisition of the volume. One major challenge will be the periodicity of the spine structure which may cause wrong assignments yielding stepwise movement by several millimeters. Therefore, experimental investigation with control is needed.

8 Summary

The goal of this project was to optimize the combined brain and spinal cord T2* weighted imaging. This project was divided into 5 subprojects, which were: dedicated shim algorithm, automated z-shim for the spinal cord region, partial SMS EPI for the brain region only, on-the-fly reconstruction, and a navigator along the spine axis.
The results from chapter 3 confirmed that the dedicated shim algorithm provides a better field homogeneity which results in a better performance of the EPI acquisition regarding geometric distortions and signal losses in the brain and spinal cord regions.
The experiments from chapter 4 confirmed that the automated z-shim method can improve the slice-wise signal loss problem in the spinal cord and provide as good as a result as the user-based z-shim method, but it is less time-consuming and not user-dependent.
The results of the investigation from chapter 5 shows that the partial SMS method delivers the same image quality as the methods without SMS or single volume SMS. However, it can significantly reduce the minimum TR and/or increase the volume coverage.
The modified on-the-fly reconstruction pipeline introduced in chapter 6 performs an optimized reconstruction regarding regridding and Maxwell Integral without a time-consuming retrospective reconstruction. Furthermore, it can correct the inhomogeneity of the coil sensitivity.
The most obvious finding to emerge from the study in chapter 7 is that a navigator echo at the spine can detect the motion of the spinal cord along the spine axis indirectly. Future studies could include an automated on-the-fly corrector of the scanned volume.
These projects can help to improve the image quality of the combined brain and spinal cord fMRI and enhance its practicability considerably.
There are multiple possible future works on the combined brain and spinal cord T2* weighted imaging. One possible investigation is to implement FLASH-based PAT for the combined EPI, as a former study [36] shows that with the use of the ACS data from the GRE-based acquisition for PAT, the tSNR of the cervical spinal cord is improved at a 7T system. They explained that the ACS data from the FLASH-based acquisition are more robust to respiration-induced phase errors in comparison to the conventional ACS data from EPI.
Another possibility to further improve the tSNR and reduce the geometric distortion in the spinal cord volume is to use the inner FOV technique for the spinal cord volume. A previous study of us [7] shows that the inner FOV technique provides better tSNR and reduces geometric distortion for the spinal cord in comparison with PAT, especially for lower spinal cord sections and obese volunteers or patients. It was not considered here because

the structure of the intervertebral disc and vertebrae in the EPI image is still essential information for the correction of movement of the spine. With an application of the navigator echo along the spine, as present before, it has the potential to detect and correct the spine motion on-the-fly. It is, therefore, a precondition for the inner FOV technique for the spinal cord volume, which could further improve the image quality of the spinal cord volume.

Bibliography

[1] J. Ashburner and K. J. Friston. Unified segmentation. *NeuroImage*, 26(3):839–51, 2005.

[2] M. Barth, F. Breuer, P. J. Koopmans, D. G. Norris, and B. A. Poser. Simultaneous multislice (sms) imaging techniques. *Magnetic Resonance in Medicine*, 75:63–81, 2016.

[3] Y. Boillat and W. van der Zwaag. Whole brain measurements of the positive BOLD response variability during a finger tapping task at 7t show regional differences in its profiles. *Magnetic Resonance in Medicine*, 81(4):2720–2727, oct 2018.

[4] H. Braaß, J. Feldheim, Y. Chu, A. Tinnermann, J. Finsterbusch, C. Büchel, R. Schulz, and C. Gerloff. Ventral premotor cortex influences spinal cord activation during force generation. *bioRxiv*, 2023.

[5] D.-Q. Chen, R. B. Marr, and P. C. Lauterbur. Reconstruction from nmr data acquired with imaging gradients having arbitrary time dependence. *IEEE Transactions on Medical Imaging*, 5(3):162–164, 1986.

[6] Y. Chu. Improved t2*-weighted imaging of the spinal cord. Master's thesis, University of Hamburg, 2019.

[7] Y. Chu and J. Finsterbusch. Geometric distortions and signal-to-noise ratio of conventional and inner fields-of-view for t2*-weighted echo-planar imaging of the spinal cord. In *Proceedings of the 27th Scientific Meeting, International Society for Magnetic Resonance in Medicine, abstract number: 1172*, 2019.

[8] Y. Chu and J. Finsterbusch. Optimized on-the-fly reconstruction for combined t2*-weighted imaging of the human brain and cervical spinal cord. In *Proceedings of the 28th Scientific Meeting, International Society for Magnetic Resonance in Medicine, abstract number: 3813*, 2020.

[9] Y. Chu and J. Finsterbusch. Partial simultaneous multi-slice acquisition of combined t2*-weighted imaging of the human brain and cervical spinal cord. In *Proceedings of the 29th Scientific Meeting, International Society for Magnetic Resonance in Medicine, abstract number: 3468*, 2021.

[10] Y. Chu and J. Finsterbusch. Automated calculation of optimum z-shim gradient pulses from a reference acquisition for spinal cord fmri. In *Proceedings of the 30th Scientific*

Meeting, International Society for Magnetic Resonance in Medicine, abstract number: 3297, London, UK, 2022.

[11] Y. Chu and J. Finsterbusch. Detecting spine movements with a navigator echo for motion correction of spinal cord fmri. In *Proceedings of the 31st Scientific Meeting, International Society for Magnetic Resonance in Medicine, abstract number: 5523*, Toronto, Canada, 2023.

[12] Y. Chu, B. Fricke, and J. Finsterbusch. Improving t2*-weighted human corticospinal acquisitions with a dedicated algorithm for region-wise shimming. *NeuroImage*, 268:119868, 2023.

[13] F. Cooke, A. Blamire, D. Manners, P. Styles, and B. Rajagopalan. Quantitative proton magnetic resonance spectroscopy of the cervical spinal cord. *Magnetic Resonance in Medicine*, 51(6):1122–1128, 2004.

[14] F. Eippert, J. Finsterbusch, U. Bingel, and C. Büchel. Direct evidence for spinal cord involvement in placebo analgesia. *Science*, 326:404, 2009.

[15] T. Ethofer, I. Mader, U. Seeger, G. Helms, M. Erb, W. Grodd, A. Ludolph, and U. Klose. Comparison of longitudinal metabolite relaxation times in different regions of the human brain at 1.5 and 3 tesla. *Magnetic Resonance in Medicine*, 50:1296–1301, 2003.

[16] S. H. Faro, F. B. Mohamed, M. Law, and J. T. Ulmer. *Functional Neuroradiology Principles and Clinical Applications*. Springer, 2012.

[17] J. Finsterbusch. Improving the performance of diffusion-weighted inner field-of-view echo-planar imaging based on 2d-selective radiofrequency excitations by tilting the excitation plane. *Journal of Magnetic Resonance Imaging*, 35(4):984–992, dec 2011.

[18] J. Finsterbusch, F. Eippert, and C. Büchel. Single, slice-specific z-shim gradient pulses improve t2*-weighted imaging of the spinal cord. *NeuroImage*, 59(3):2307–2315, feb 2012.

[19] J. Finsterbusch, C. Sprenger, and C. Büchel. Combined t2*-weighted measurements of the human brain and cervical spinal cord with a dynamic shim update. *NeuroImage*, 79:153–161, 2013.

[20] K. J. Friston, J. Ashburner, C. D. Frith, J.-B. Poline, J. D. Heather, and R. S. J. Frackowiak. Spatial registration and normalization of images. *Human Brain Mapping*, 3(3):165–189, 1995.

[21] U. C. L. Functional Imaging Laboratory. SPM software for neuroimaging analysis, Accessed 2023.

[22] G. Girard, M. Taso, V. Callot, D. Duclap, C. Gros, J. Maranzano, N. Richard, N. Stikov, and J. Cohen-Adad. Spinal Cord Toolbox. `https://spinalcordtoolbox.com/`, Accessed 2023.

[23] C. Gros, B. De Leener, A. Badji, J. Maranzano, D. Eden, S. M. Dupont, J. Talbott, R. Zhuoquiong, Y. Liu, T. Granberg, R. Ouellette, Y. Tachibana, M. Hori, K. Kamiya, L. Chougar, L. Stawiarz, J. Hillert, E. Bannier, A. Kerbrat, G. Edan, P. Labauge, V. Callot, J. Pelletier, B. Audoin, H. Rasoanandrianina, J.-C. Brisset, P. Valsasina, M. A. Rocca, M. Filippi, R. Bakshi, S. Tauhid, F. Prados, M. Yiannakas, H. Kearney, O. Ciccarelli, S. Smith, C. A. Treaba, C. Mainero, J. Lefeuvre, D. S. Reich, G. Nair, V. Auclair, D. G. McLaren, A. R. Martin, M. G. Fehlings, S. Vahdat, A. Khatibi, J. Doyon, T. Shepherd, E. Charlson, S. Narayanan, and J. Cohen-Adad. Automatic segmentation of the spinal cord and intramedullary multiple sclerosis lesions with convolutional neural networks. *NeuroImage*, 184:901–915, 2019.

[24] H. P. Hetherington, C. H. Moon, M. Schwerter, N. J. Shah, and J. W. Pan. Dynamic b0 shimming for multiband imaging using high order spherical harmonic shims. *Magnetic Resonance in Medicine*, 85(1):531–543, 2021.

[25] C. Hutton, A. Bork, O. Josephs, R. Deichmann, J. Ashburner, and R. Turner. Image distortion correction in fmri: A quantitative evaluation. *NeuroImage*, 16(1):217–240, 2002.

[26] H. Islam, C. S. W. Law, K. A. Weber, S. C. Mackey, and G. H. Glover. Dynamic per slice shimming for simultaneous brain and spinal cord fmri. *Magnetic Resonance in Medicine*, 81(2):825–838, 2019.

[27] J. Jackson, C. Meyer, D. Nishimura, and A. Macovski. Selection of a convolution function for fourier inversion using gridding (computerised tomography application). *IEEE Transactions on Medical Imaging*, 10(3):473–478, 1991.

[28] M. Kaptan, S. J. Vannesjo, T. Mildner, U. Horn, R. Hartley-Davies, V. Oliva, J. C. W. Brooks, N. Weiskopf, J. Finsterbusch, and F. Eippert. Automated slice-specific z-shimming for functional magnetic resonance imaging of the human spinal cord. *Human Brain Mapping*, 43(18):5389–5407, 2022.

[29] B. D. Leener, S. Lévy, S. M. Dupont, V. S. Fonov, N. Stikov, D. L. Collins, V. Callot, and J. Cohen-Adad. Sct: Spinal cord toolbox, an open-source software for processing spinal cord {MRI} data. *NeuroImage*, 145, Part A:24 – 43, 2017.

[30] Z. Liang and P. C. Lauterbur. *Principles of Magnetic Resonance Imaging*. SPIE Optical Engineering press, 2000.

[31] P. Mansfield. Multi-planar image formation using NMR spin echoes. *Journal of Physics C: Solid State Physics*, 10(3):L55–L58, feb 1977.

[32] J. Martindale, A. J. Kennerley, D. Johnston, Y. Zheng, and J. E. Mayhew. Theory and generalization of monte carlo models of the bold signal source. *Magnetic Resonance in Medicine*, 59:607–618, 2008.

[33] S. Ogawa, T. M. Lee, A. R. Kay, and D. W. Tank. Brain magnetic resonance imaging with contrast dependent on blood oxygenation. *PNAS*, 87:9868–9872, 1990.

[34] J. Pauly, D. Nishimura, and A. Macovski. A k-space analysis and of small-tip-angle and excitation. *Journal of Magnetic Resonance*, 1989.

[35] F. Schmitt, M. Stehling, and R. Turner. *Echo-Planar Imaging*. Springer, 1998.

[36] A. C. Seifert and J. Xu. Impact of autocalibration method on accelerated epi of the cervical spinal cord at 7 t. *Magnetic Resonance in Medicine*, 88(6):2583–2591, 2022.

[37] K. Setsompop, J. Cohen-Adad, B. A. Gagoski, T. Raij, A. Yendiki, B. Keil, V. Wedeen, and L. Wald. Improving diffusion mri using simultaneous multi-slice echo planar imaging. *Journal of Physics C: Solid State Physics*, 63(1):569–580, jun 2012.

[38] S. C. Simon-Zoula, L. Hofmann, A. Giger, B. Vogt, P. Vock, F. J. Frey, and C. Boesch. Non-invasive monitoring of renal oxygenation using bold-mri: a reproducibility study. *NMR in Biomedicine*, 19(1):84–89, 2006.

[39] C. Sprenger, J. Finsterbusch, and C. Büchel. Spinal cord–midbrain functional connectivity is related to perceived pain intensity: A combined spino-cortical fmri study. *Journal of Neuroscience*, 35(10):4248–4257, 2015.

[40] A. Tinnermann, S. Geuter, C. Sprenger, J. Finsterbusch, and C. Büchel. Interactions between brain and spinal cord mediate value effects in nocebo hyperalgesia. *Science*, 358(6359):105–108, 2017.

[41] X. Zhou, Y. Du, M. Bernstein, H. Reynolds, and J. Maier. Concomitant field induced artifacts in axial echo planar imaging. *Magn. Reson. Med*, 39:596–605, 1998.